University of Toronto

Masters Thesis

Evaluation of Low-Cost MEMS Accelerometers and Investigation of Inertial Algorithms for Dead Reckoning in Railway Environment

Author:
René Rail-Ip

Supervisor:
Dr. David Johns

A thesis submitted in conformity with the requirements for the degree of Master of Applied Science, Graduate Department of Department of Electrical and Computer Engineering, in the University of Toronto

"Nothing in the world can take the place of persistence. Talent will not. The world is full of unsuccessful men with talent. Genius will not. Unrewarded genius is almost a proverb. Education will not. The world is full of educated derelicts. Persistence and determination alone are omnipotent. The slogan 'Press On' has solved and always will solve the problems of the human race."

Calvin Coolidge

UNIVERSITY OF TORONTO

Abstract

Faculty of Applied Science and Engineering
Department of Electrical and Computer Engineering

Master of Applied Science

Evaluation of Low-Cost MEMS Accelerometers and Investigation of Inertial Algorithms for Dead Reckoning in Railway Environment

by René Rail-Ip

Low-cost micro-electro-mechanical systems (MEMS) accelerometers are gaining momentum in the defence, aerospace, transportation, and automotive industries. While high-cost accelerometers are being used on subway trains for their signalling systems, this work investigates the possibility of replacing them with low-cost MEMS devices. To achieve this goal, a 3D printer was modified for use as a three-dimensional motion platform. A series of motions was developed to test parameters of the sensors such as noise, cross-axis sensitivity, bias stability, and accurate displacement estimation from double integration. A high-speed, high-resolution camera was used as a benchmark of the actual position of sensors throughout testing. In addition, the sensors were tested on subway trains. The results show that the Kionix KXRB5 accelerometer performs the best, even out-performing the high-end sensor tested. In addition, inertial algorithms were developed that were able to estimate displacements to below 10% error on the evaluation platform and subway line.

Acknowledgements

I would like to thank my girlfriend Rose, for her constant support, especially during the writing of this thesis. You helped me stay focused and I will forever appreciate that. I love you, always.

I would like to thank my parents and brothers for their continous and neverending support throughout my two years in graduate school and my years in undergraduate school. I love and miss you guys.

I would like to thank my supervisor, Dr. David Johns, for his guidance and advice throughout the thesis and for setting up the project with our industry partners. I would like to thank him especially for his fantastic management style, which allowed me to follow my own path while achieving goals we set out together. Thank you also for always providing new and interesting technology to discuss every week, keeping me inspired.

Thank you greatly to Peter Timmermans for his managing role as the coordinator with Thales and for joining me during all the testing on the TTC, including testing entirely through the night, as well as helping with the thermal chamber.

I would finally like to thank Carl Schwellnus and Ehsan Kimiagar from Thales for your time and expertise every week in suggesting methods to improve the results and for offering guidance and advice throughout the project. I learned so much from all of your insights, questions, and our discussions.

Contents

List of Figures

List of Tables

Abbreviations

AD	**A**nalog **D**evices
ADC	**A**nalog to **D**igital **C**onverter
FIR	**F**inite **I**mpulse **R**esponse
GNSS	**G**lobal**N**avigation **S**atellite **S**ystem
I2C	**I**nter-**I**ntegrated **C**ircuit
IIR	**I**nfinite **I**mpulse **R**esponse
IMU	**I**nertial **M**easurement **U**nit
GCDC	**G**ulf **C**oast **D**ata **C**oncepts
PC	**P**ersonal **C**omputer
PCB	**P**rinted **C**ircuit **B**oard
PSOC	**P**rogrammable **S**ystem **O**n a **C**hip
RMS	**R**oot **M**ean **S**quare
SPI	**S**erial **P**eripheral **I**nterface
TTC	**T**oronto **T**ransit **C**ommission
UTIAS	**U**niversity of **T**oronto **I**nstitute for **A**erospace **S**tudies

Physical Constants

Gravity of Earth $g = 9.8066 \text{ m/s}^2$

Symbols

a	acceleration	m/s^2
a_a	acceleration applied to sensors due to motion	m/s^2
a_x	acceleration on sensor's x-axis output	m/s^2
a_y	acceleration on sensor's y-axis output	m/s^2
a_z	acceleration on sensor's z-axis output	m/s^2
C	capacitance	F
L	conductor length	m
A	cross-sectional area of current flow	m^2
i	current	A
B_d	damping coefficient	Ns/m
x	displacement	m
A_e	electrode area	m^2
F_E	external force acting on proof mass	N
GF	gauge factor	
d_0	initial electrode gap	m
m	mass of accelerometer proof mass	kg
x_c	movement of capacitor plate from initial position	m
π	piezoresistivity coefficient	
ϵ	permittivity	F/m
ν	Poisson's ratio	
Q	quality factor	
R	resistance	Ω
ρ	resistivity	Ωm
ω_0	resonant frequency	rads

ϕ	sensor tilt angle	rads
B	sensor zero-g bias	g
BW	signal bandwidth	Hz
σ	signal standard deviation	g
N_0	spectral noise density	$\mu g/\sqrt{Hz}$
k	spring constant	N/m
S	strain	
T	stress	N/m^2
t	time	s
v	velocity	m/s
V	voltage	V
E	Young's modulus	N/m^2

This thesis is dedicated to Rose and to my parents, Christine and Alec, for their continous love, support, and faith in me.

Chapter 1

Introduction

MEMS technologies are most widely used in the production of accelerometers, which are capable of sensing forces along three axes of motions and outputting this data as an analog or digital signal. The largest driver of this technology in recent years has been the automotive industry, where high-G sensors are used in air bag deployment and low-G sensors are used for active suspension and vehicle stabilization [2]. More recently, research is going into the use of accelerometer sensors to estimate position for navigation and localisation purposes. Accelerometers are mounted together with gyroscopes, which measure angular velocities about the three axes of motion, to form an Inertial Measurement Unit (IMU). These IMUs perform mathematical integration on data from the accelerometers and gyroscopes to obtain positional data about the system on which the IMU is mounted. Theoretically, this concept can provide the user with accurate displacements and intelligent robotic navigation and localisation.

However, MEMS accelerometers like all sensors suffer from various sources of error. Sensor noise, nonlinearities, bias and sensitivity uncertainty, and other sources of error can lead to large errors in data output and when these errors are integrated to obtain velocity and displacement, they accumulate. This effect is called random walk and even at rest can produce errors of many metres. It is crucial to gain an understanding of these errors in order to effectively utilize these advancing sensors.

The applications of this sensing technology are endless and with increasing acceptance for robotics in the household and decrease in the cost of the sensors, the demand to use accelerometers in low-cost consumer robotics will grow. In addition, with the increasing performance of low-cost sensors, transportation and automotive industries will begin to shift towards replacing high-end, expensive sensors with lower-cost MEMS sensors that have the same performance.

1.1 Operation Principles

MEMS accelerometers work similarly to a mass-spring-damper system. In accelerometers, the mass is called a proof mass and is connected to the frame by a flexible spring. Gas or liquids are used in the package to introduce the damping effect and prevent excessive vibrations and ringing. Figure 1.1 shows the system and the following equations outline how acceleration is detected.

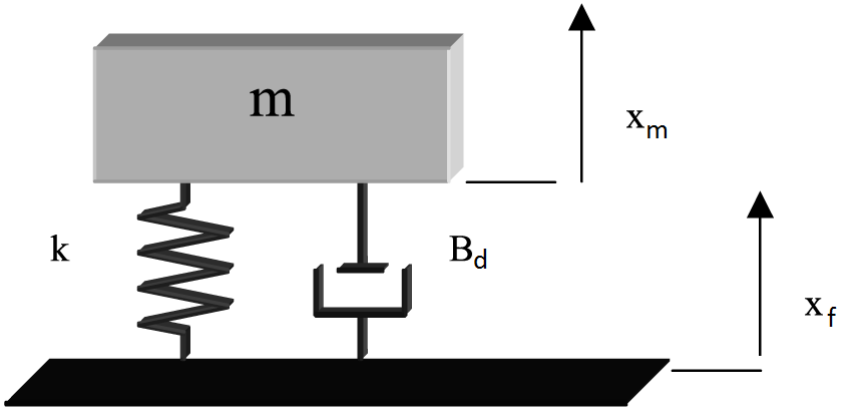

FIGURE 1.1: Structure of an accelerometer where m is the proof mass, k is the spring constant, B_d is the damping coefficient, x_m is the position of the proof mass away from the spring's natural position, and x_f is the frame's position

An accelerometer measures the force being applied to the proof mass inside the chip, shown in Figure 1.1. The setup in Figure 1.1 is for a one-axis measurement, in this case measuring in the upward direction. At rest or at constant acceleration, the net forces acting on the sensor are the following, given by Hooke's law and Newton's second law.

$$m\ddot{x}_f = kx_m \tag{1.1}$$

In the above equation, m is the proof mass, k is the spring constant, x_f is the position of the frame, and x_m is the position of the mass relative to the frame, away from the spring's natural position. The acceleration can therefore be calculated if the displacement x_m is known.

$$\ddot{x}_f = \frac{kx_m}{m} \tag{1.2}$$

This turns the problem into one of sensing a displacement, rather than an acceleration. At a constant acceleration, the proof mass will be displaced by a certain amount x_m. This explains why, at rest, an accelerometer aligned vertically with the axis of gravity will

measure an acceleration of $9.8\,\mathrm{m/s^2}$ upward. The accelerometer is actually measuring the normal force being applied to the sensor in response to the force due to gravity.

There are two basic sensing principles that are used for DC-response MEMS accelerometers [2]. They are piezoresistive sensing and capacitive sensing. Piezoresistive sensing uses piezoresistors on the spring in order to detect changes in resistance due to acceleration-induced stress. These sensors are robust and simple, however have poor noise and power performance. Capacitive sensing detects small changes in capacitance due to the movement between the proof mass and the frame to determine acceleration. These are the most widely used acceleration sensors as they are low-cost with low noise and power consumption. These will be discussed in more detail below.

The following equations show how acceleration is obtained from this structure based on the dynamics of the system when there are changes in acceleration as well as velocity and position. Equation 1.3 follows by analyzing the net forces acting on the proof mass m in Figure 1.1.

$$m\ddot{x}_m + B(\dot{x}_m - \dot{x}_f) + k(x_m - x_f) = F_E \tag{1.3}$$

In the above equation, m is the mass of the proof mass, k is the spring constant, B is the damping coefficient of the gas or liquid, x_m and x_f are the positions of the mass and the frame, respectively, and F_E is the external force acting on the mass. We can subtract $m\ddot{x}_f$ from both sides to obtain the following equation.

$$m(\ddot{x}_m - \ddot{x}_f) + B(\dot{x}_m - \dot{x}_f) + k(x_m - x_f) = F_E - m\ddot{x}_f \tag{1.4}$$

We take $x = x_m - x_f$ and $F = F_E - m\ddot{x}_f$ to get the following equation.

$$m\ddot{x} + B\dot{x} + kx = F \tag{1.5}$$

From this equation, we take the Laplace transformation and use quality factor $Q = \frac{\omega_0 m}{B}$ and resonant frequency $\omega_0 = \sqrt{\frac{k}{m}}$ to obtain the frequency response below.

$$x = \frac{\frac{F}{m}}{s^2 + \frac{s\omega_0}{Q} + \omega_0^2} = \frac{\ddot{x}_f}{s^2 + \frac{s\omega_0}{Q} + \omega_0^2} = H(s)\ddot{x} \tag{1.6}$$

The equation above shows the frequency response that relates the acceleration to the displacement of the proof mass in Figure 1.1. Therefore if there is a method to detect the displacement of the proof mass, then the acceleration response can be deduced.

Two ways to detect displacement are investigated below: piezeoresistive sensing and capacitive sensing.

1.1.1 Piezoresistive Sensing

The idea of piezoresistive sensing is based on the fact that when material is subjected to mechanical stress, its electrical resistance changes. It is based on the following law.

$$R = \rho \frac{L}{A} \tag{1.7}$$

In this equation, R is the resistance, ρ is the resistivity, A is the cross-sectional area of the conductor, and L is the length. We can derive this equation to obtain a form relating fractional changes in resistance.

$$\frac{\Delta R}{R} = \frac{\Delta \rho}{\rho} - \frac{\Delta A}{A} + \frac{\Delta L}{L} \tag{1.8}$$

From the above equation, changes in resistance are due to material and geometric changes. The material changes are related to resistivity changes while the geometric changes are due to changes in surface area and length. An often used measure of piezoresistivity is the piezoresistivity coefficient π defined below.

$$\pi = \frac{\Delta \rho / \rho}{T} = \frac{\Delta \rho / \rho}{ES} \tag{1.9}$$

In this equation, T is stress, E is Young's modulus, and S is strain. Materials with high piezoresistivity coefficients are most suited for application in accelerometers as they are able to better show changes in resistance, which can be detected by measuring voltage or current. A second coefficient used is the gauge factor, GF, defined below.

$$GF = \frac{\Delta R / R}{S} = \frac{\Delta R / R}{\Delta L / L} \tag{1.10}$$

Equations (1.8), (1.9), and (1.10) can be combined to obtain the following equation.

$$GF = 1 - \frac{\Delta A / A}{\Delta L / L} + \frac{\Delta \rho / \rho}{\Delta L / L} = 1 + 2\nu + E\pi \tag{1.11}$$

In the above, we've used the Poisson's ratio ν defined as $-\frac{\Delta A/A}{2\Delta L/L}$, which for almost all materials is between 0 and 0.5. Crystalline and polycrystalline silicon have large gauge factors in the hundreds, which makes them optimal choices for piezoresistive sensors.

The main disadvantage of using piezeoresistors is that they inherently introduce various types of noise. The main noise sources that add error to this type of sensing are thermal, shot, and flicker noise, which are discussed in other literature [2].

1.1.2 Capacitive Sensing

Capacitive sensors have taken the most of the market share for accelerometer technologies due to their low-cost, low-power, and low-noise performance. Mechanical movement induces changes in capacitance that can be measured, though sometimes in challenging ways for low capacitances. The operation of these sensors is based on the current through a capacitor, given below.

$$i = \frac{\partial CV}{\partial t} = C\frac{\partial V}{\partial t} + V\frac{\partial C}{\partial t} \tag{1.12}$$

Changes in current are due to both changes in voltage and changes in capacitance. The first term in the equation is often called the displacement measurement because changes of voltage are related to change in position while the second term is called velocity measurement because it depends on how quickly capacitance changes. Because the velocity measurement is proportional to the capacitance rate-of-change, it cannot be used to determine static displacements and is therefore not often used for accelerometers.

The position measurement term in equation (1.12) is the term most often used in circuit analysis showing that the current through a capacitor is equal to the capacitance times the change in voltage. It is shown below.

$$i = C\frac{\partial V}{\partial t} \tag{1.13}$$

Parallel plate capcitors are most often used in MEMS technologies. They are constructed by two parallel plates separated by a small gap. The capacitance is then given by the following.

$$C = \epsilon\frac{A_e}{d_0 - x_c} \tag{1.14}$$

In the above, ϵ is the permittivity, A_e is the electrode area, d_0 is the initial electrode gap, and x_c is the movement of the capacitor plate from the initial position. By using four capacitors in a Wheatstone bridge configuration as shown in Figure 1.2, changes in displacement x_c will correspond to changes in output voltage.

Designing the two left capacitors so that they are always equal to some capacitance C_0 and the two right capacitors as moving in opposite directions, we can see that $C_1 = \epsilon\frac{A_e}{d_0 - x_c}$ and $C_2 = \epsilon\frac{A_e}{d_0 + x_c}$. If we set $C_0 = \epsilon\frac{A_e}{d_0}$, we have $C_1 = \frac{C_0}{1 - \frac{x_c}{d_0}}$ and $C_2 = \frac{C_0}{1 + \frac{x_c}{d_0}}$. Thus,

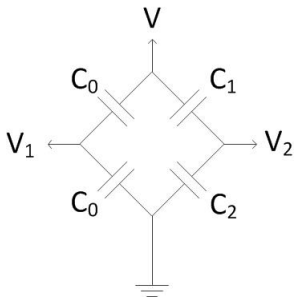

FIGURE 1.2: Capacitors in a Wheatstone Bridge Configuration for Differential Measurement

we can take the differential $V_{out} = V_2 - V_1$ and after some manipulation we obtain the result below.

$$V_{out} = V_2 - V_1 = \frac{x_c}{2d_0} V \tag{1.15}$$

This shows that the differential voltage output makes the change in displacement linearly related to change in output voltage, even though the change in displacement is related nonlinearly to the change in capacitance. From this change in displacement x_c, we can use the dynamics of the spring-mass-damper system to obtain the acceleration that produced the displacement.

The main disadvantage of using capacitive sensing is that parasitic capacitances exist that can distort the measured signal voltage. This is the biggest issue that must be addressed and there are various ways to reduce the parasitic capacitances, such as single-chip integration, shielding and grounding, and physical separation between capacitor electrodes [2].

1.2 Capabilities and Applications

Accelerometer sensor technology has many applications in the industrial, aerospace, and robotics fields. Some of these applications are listed below.

- Vehicle Dynamics
- Failure Analysis
- Vehicle Durability Testing
- Crash Testing
- Active Vibration Damping
- Motion Control for Robots or Tools
- Inertial Motion Measurement
- Robotic Manipulator Perception

Due to the linear nature of accelerometers, with the capability of sensing along the direction of one axis, there are some applications that are directly related to the railway environment. Within this field, there are many applications of accelerometer technology, which increase the reliability of the transportation, the comfort of the passengers, or the safety of the system. Some applications specific to the railway environment are listed below.

- Bogie monitoring, diagnostics system for security or comfort
- High-speed train tilt control system for improved passenger comfort
- Position monitoring of magnetic levitation train
- Health and usage monitoring system
- Shock monitoring
- Precise train positioning
- Railway track monitoring system

1.3 Accelerometers and Inertial Motion Units

One of the most interesting and potentially impactful applications of accelerometers is in the potential use for measuring distances travelled in navigation and localisation applications [1] [3]. In order to use accelerometers in inertial navigation applications, an inertial measurement unit (IMU) must be built, which combines the accelerometers with gyroscopes onto one module, which when attached to an object, can measure the necessary changes in orientation and displacement, as shown in Figure 1.3. The mathematical integration of the gyroscope data outputs the orientation of the object while the double integration of the accelerometer data provides the changes in three dimensions of movement. However, the technology is not immune to error, therefore a strong understanding of associated sensor error is necessary while techniques to reduce or avoid this error are essential to the successful use of this technology for inertial applications.

Although there are sources of error that arise from the use of MEMS gyroscope and accelerometer technology, they can be reduced by implementing real-time bias and sensitivity updates and estimates. Therefore, it is desirable to design an inertial measurement unit that can adequately compute the orientation and position of some object. It is known that the sensors provide angular speeds and translational accelerations, therefore the algorithm consists of integrating the angular speed to obtain orientation with respect to the frame of reference. With this update, double integrations of translational accelerations will enable a mobile robot to know which direction it is moving. This is summarized in block diagram form in Figure 1.4.

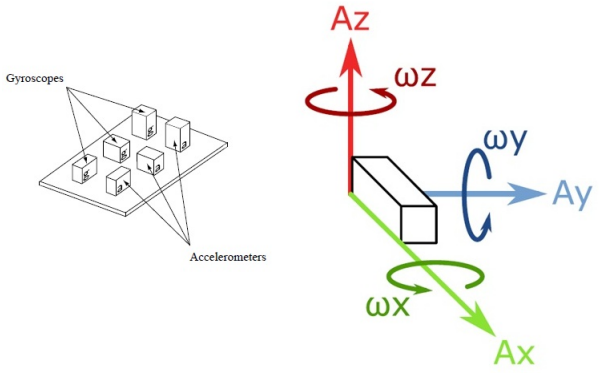

FIGURE 1.3: Inertial Motion Unit Measuring Accelerations and Angular Velocities [1]

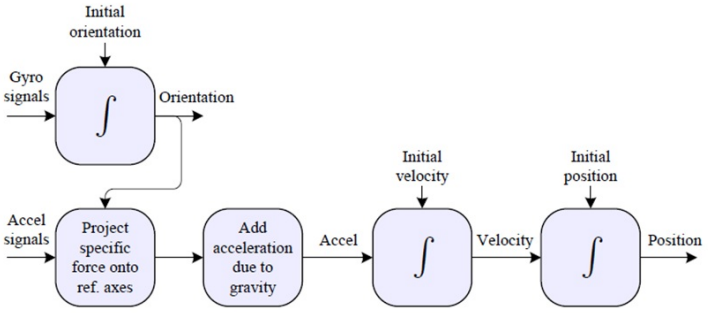

FIGURE 1.4: Inertial Measurement Unit Block Diagram Algorithm [1]

Another concept is the idea of pedestrian localisation, which utilizes an IMU mounted onto a human to sense their navigation through an environment. Using the steps of the human as they touch the floor as zero-speed updates for the state estimation algorithms enables higher precision and better results [1]. This concept of zero-speed updates is further investigated in Chapter 4.

Research was done in the use of an IMU for train localisation, which includes using gyroscopes and accelerometers to determine the position of the train [4]. This work utilizes feature detection to determine when the train is in a certain type of track or in a certain type of motion, such as as curves, changing slopes, or standing still. Feature detection is common in image processing algorithms in robotics. Other literature has also been able to robustly estimate position using various sensors on-board a train [5]. However, this work requires the use of Global Navigation Satellite System (GNSS) data, which is not always available for subway trains. Further work in [6] acknowledged the limitation of using GNSS data and attempts to utilize various on-board sensors including an IMU, odometer, and feature classification to fuse data using a Bayesian filter, which gave encouraging results in simulations.

1.4 Problem Statement and Thesis Organisation

There is a lot of research and literature that has been used to attempt to combine accelerometers, gyroscopes, and magnetometers into an effective and accurate IMU for dead reckoning in three-dimensions using various sensor fusion algorithms [4] [5] [6]. The purpose of this thesis is to determine the capabilities for these sensors to work in the railway environment, specifically on subway trains. This railway application simplifies the dead-reckoning problem, as the rails constrain the motion of the vehicle in such a way that the majority of its motion is in one dimension. This is an approximation but it is desired to see how much error exists using this approximation. Using this simplified problem, the challenge is to determine if simplified sensor hardware could accurately determine the subway train's position through time. The simplified hardware for this thesis is to use a single accelerometer, rather than three different types of sensors.

In order to effectively test this concept, an evaluation platform was built that would test various inertial algorithms on accelerometers travelling in a line, similarly to the motion that would be applied in the railway environment. This evaluation platform is described in Chapter 2, as well as the image processing algorithms used to determine the ground truth of sensors during testing and a description of the setup used to capture data from analog and digital sensors.

After testing on the evaluation platform, the sensors were brought into the field on the TTC Shepphard line in Toronto. Various tests were designed to determine if the algorithms developed could accurately estimate displacement from the data obtained. Landmarks in the subway line were used as an estimate to determine the ground truth of the train throughout testing (for example, it is known that the blue emergency lights in the tunnel are spaced 150 m apart).

The major part of this thesis is to find a low-cost MEMS accelerometer that could replace the high-cost sensor currently in-use on subway trains in the railway environment. This accelerometer has to be replaced whenever a train is repaired and these replacements costs can end up being very high. Therefore it is of interest to reduce the cost of building and the cost of repair by finding low-cost accelerometers that perform as well as or better than the current sensor. Chapter 3 details the accelerometer evaluation stages of this thesis, in which a large number of sensors are sourced and considered. Using a weighted decision-making process, eight sensors are chosen to be evaluated in the thesis to possibly replace the Jewell Instruments LCA-165-5051 currently being used. These eight sensors undergo testing on the evaluation platform and in the railway environment in order to compare them and benchmark them.

Finally, in Chapter 4, the thesis focuses on improving the inertial algorithms used to estimate displacements. The major challenge that must be addressed is the zero-g bias estimation problem. Due to changing track gradients and the suspension and braking mechanisms of the train, the sensors are constantly at a slight unknown tilt with respect to the gravity vector. This introduces a small component of gravity on the output of the sensing axis, which translates to an unwanted added acceleration when there may or may not be motion. Various methods are investigated, such as zero-velocity updates, bias interpolation, optimal bias determination, and delta-mounted sensors.

To summarize, the main objectives of this thesis are below.

- **Find and/or build a motion platform for evaluation of accelerometers and design a setup that can be used to capture analog and digital data coming from accelerometers that are chosen for evaluation.**
- **Research the most prominent MEMS sensor companies and list their accelerometers. Narrow the list in order to evaluate and benchmark approximately eight accelerometer sensors to determine which has the most promise in an inertial application for estimating displacement.**
- **Investigate inertial algorithms that only use the accelerometer sensor to accurately estimate displacements in a railway environment.**

Chapter 2

Experimental Setup

2.1 Accelerometer Evaluation Platform

This section describes the evaluation platform that was designed to benchmark the performance of various accelerometers. The primary objective of this platform is to measure some basic properties of the accelerometers and compare these measurements to the specifications from the datasheets. The secondary objective of this platform is to determine the sensors' ability to have their output double-integrated to obtain estimates of the displacement. The following sections describe the motion platform in detail, the accelerometer evaluation setup, and the camera and image processing used to determine ground-truth of the sensors during experimentation.

2.1.1 Motion Platform

The motion platform used is a modified Rostock MAX 3D printer, shown in Figure 2.1. This platform was chosen largely because of its low-cost. However, despite the low cost, it is a requirement for the printer to be precise to the millimetre in order to successfully print 3D objects.

This printer utilizes three arms in a delta configuration connected to stepper motors to move the print head linearly in three dimensions. The platform has a movement resolution of 1 mm and can move at speeds up to 800 mm/s . The hot-end of the printer was removed and the end-effector was modified so that a sensor suite could be fitted onto it. The printer is commanded using G-code from Repetier-Host software, which allows the user to command the end effector to a coordinate in the working space as well as command a speed.

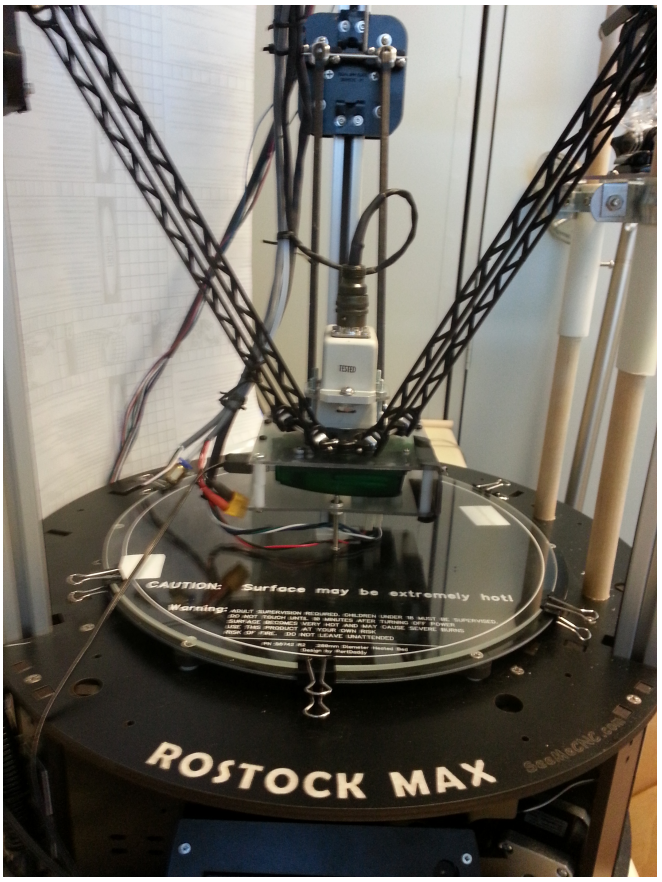

FIGURE 2.1: Rostock MAX 3D printer used as a motion platform

2.1.2 Accelerometer Evaluation Setup

In order to evaluate the accelerometers, there had to be a method to log the data from each sensor. Although various accelerometers have off-the-shelf dataloggers and evaluation platforms, it was inevitable that a custom printed-circuit-board would have to be developed to log the data from some accelerometers that were not sold with an evaluation platform. Due to past experiences with the Programmable-System-on-a-Chip from Cypress Semiconductors, it was chosen to fulfill the communication requirements to log data from analog or digital accelerometers. The PSOC5 development kit was purchased, shown in Figure 2.2, which allows the user to program it to perform many different tasks. For the purposes here, it was used as an analog-to-digital converter and digital communication hub. Further, it was used to communicate over a serial-to-USB communication with a PC, which saves the data to a text file. The programmable system can be seen in Figure 2.3.

An interrupt system was used to sample the ADC and read digital data at a frequency of 200 Hz. The PSOC5 samples 8 ADC channels, reads the SPI data, and sends this information to the PC with a timestamp every 5 ms. On the PC side, a Matlab program

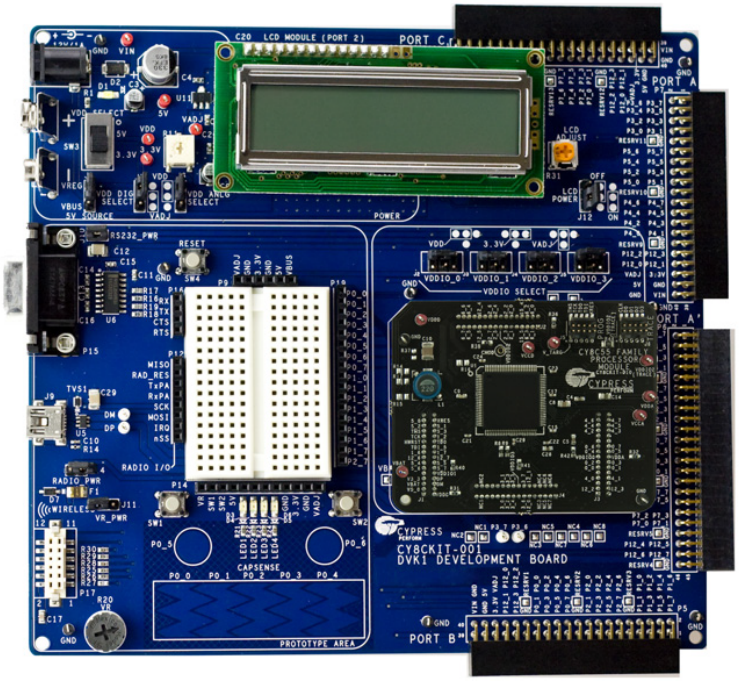

FIGURE 2.2: Programmable-system-on-a-chip used to read accelerometer data and transmit to a PC

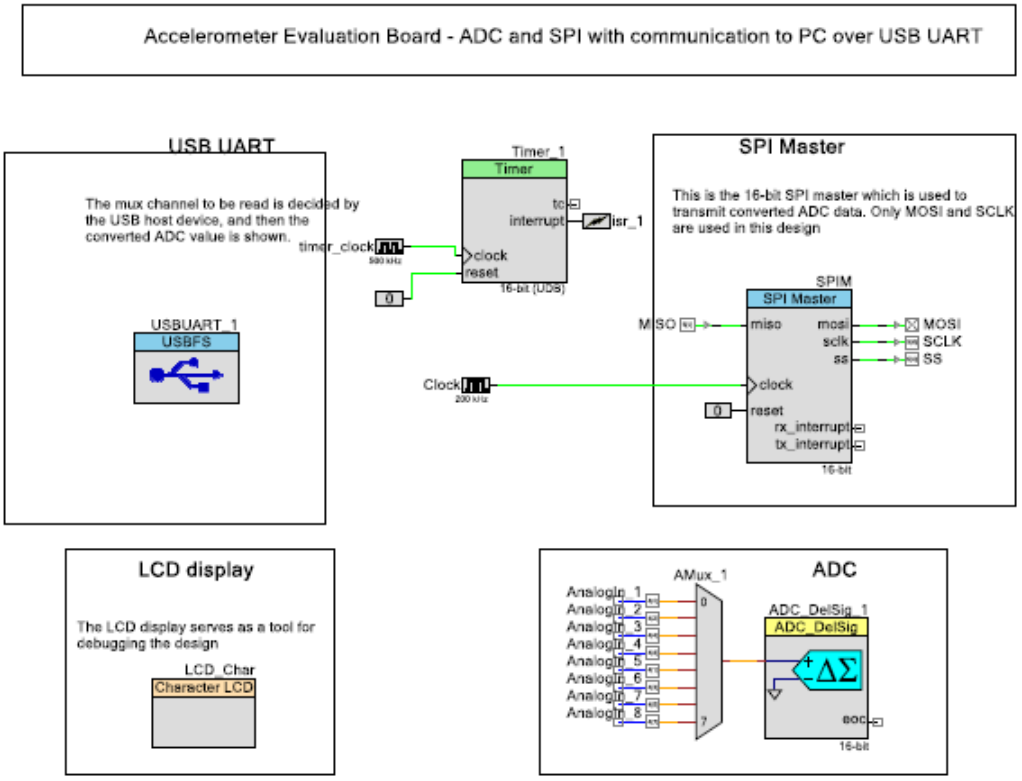

FIGURE 2.3: Components in the programmable system-on-a-chip needed to log data

was written to connect to the PSOC5 serial port and read in the data, then write it to a text file. To ensure that the timing was correct, the setup was tested by comparing the output timestamps to a stopwatch running at the same time. This ensured there were no delays in the communication and that the timestamps were accurate for each sample being logged.

2.1.3 High-Speed Camera and Image Processing

Commanding the motion of the end effector is done by specifying coordinates and the speed of motion. However, throughout motion the actual position at every point of time is not known precisely. In order to know the actual position, or ground truth, of the end-effector over time, a high-speed, high-resolution camera was chosen. The GoPro Hero3+ is capable of taking 960p video at 100 frames per second. At a low cost, this camera was desirable compared to other high-speed cameras ranging in the thousands of dollars. The GoPro camera has a built-in fish-eye lens, which adds distortion to the videos taken. GoPro Studio was used in post-processing to flatten the images and remove the distortion.

To determine the position of the end-effector, a simple target of two circles of known radius is mounted onto the side of the sensor platform (visible in Figure 2.4 and Figure 2.5). The GoPro camera was mounted to the side of the evaluation platform, as seen in Figure 2.4.

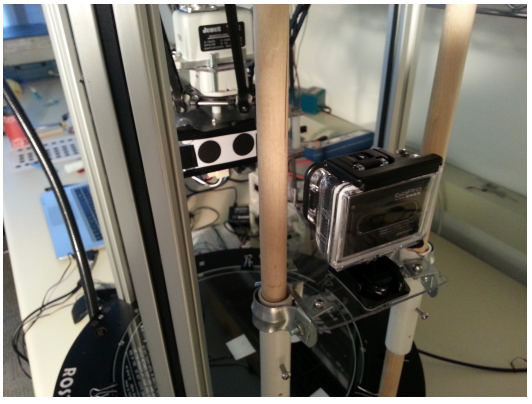

FIGURE 2.4: GoPro camera mounted to evaluation platform

The camera records the motion of the end-effector as it runs through the tests. During post-processing, a circle-detection algorithm based on the Hough Transform from Mathworks [7] is used, which can find circles in an image and determine the position and the radius of the circles in pixels. Knowing the actual radius of the circles in mm allows us to obtain a pixel to mm scale. Therefore, as the position of the circles changes in the image, the corresponding change in pixels can be scaled to a change in mm, giving us

our ground truth of the end effector. The picture in Figure 2.5 shows one frame read in from the GoPro camera of the target used with two circles. The circles are being outlined as they are detected by the Hough Transform algorithm and the coordinates of the centre's of the circles are being calculated and displayed.

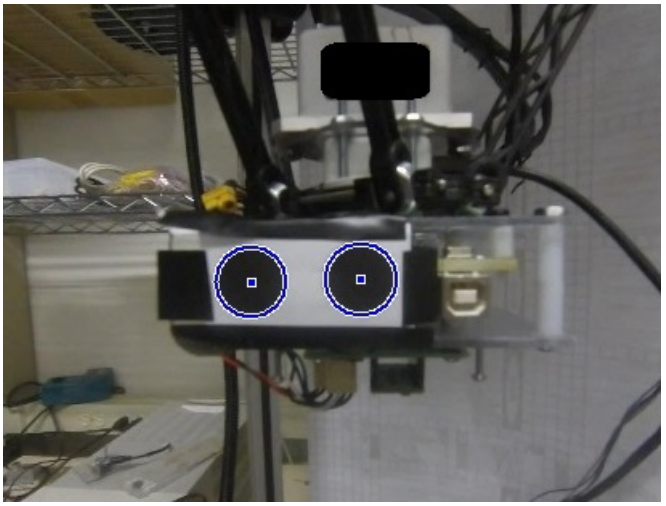

FIGURE 2.5: Hough detection algorithm detecting circles to obtain coordinates of the centre of the circles

After the entire video is processed, the trajectory of the end effector throughout the test is known, as seen in Figure 2.6. This figure illustrates the motion captured during a step motion test, which travels three iterations from $-10\,\text{cm}$ to $10\,\text{cm}$ in steps of $1\,\text{cm}$, with pauses of $400\,\text{ms}$ between each step. These displacements can be differentiated twice to obtain velocity and acceleration, which provides us with a ground-truth acceleration with which we can compare accelerometer data.

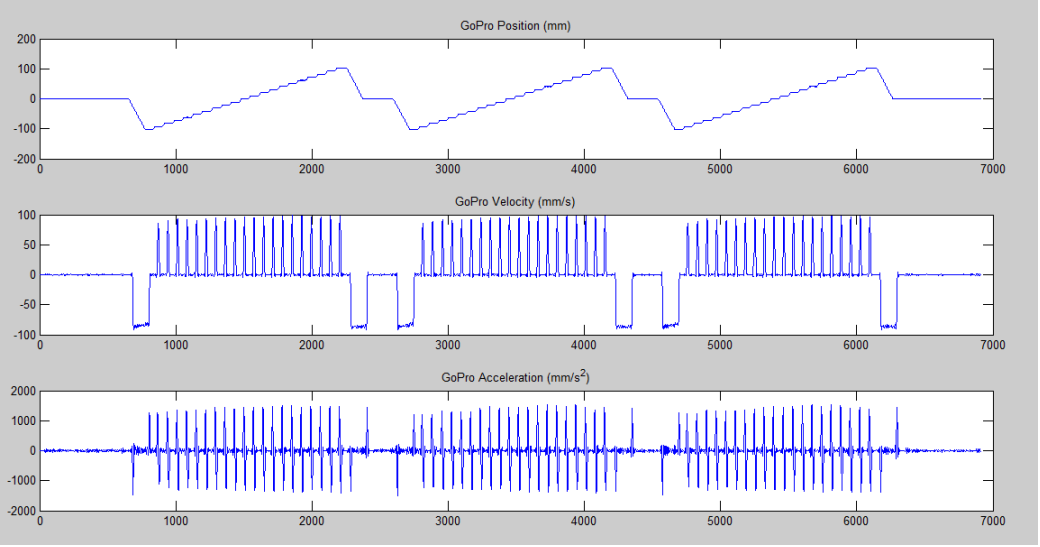

FIGURE 2.6: Output of ground-truth calculation using GoPro camera

2.1.4 Evaluation Setup for Railway Testing

Although the initial testing was done on the evaluation platform, the sensors had to be further tested in the environment in which they will be running. For testing in the railway environment, the sensors were removed from the evaluation platform and placed onto a wooden frame, shown in Figure 2.7, which could be screwed down to the floor of a subway train. During testing, the frame was screwed into the floor beneath seats on the subway train, shown in Figure 2.8. The evaluation tests were performed on the TTC Sheppard line, travelling between the Sheppard-Yonge station and Don Mills station. This subway line is shown in Figure 2.9

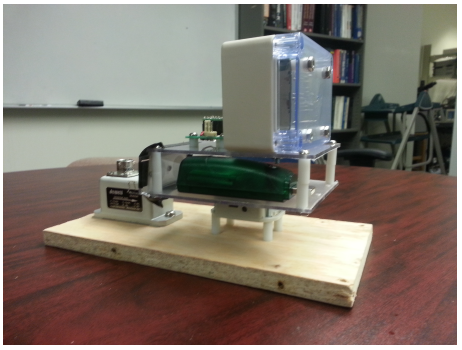

FIGURE 2.7: Sensors mounted onto wooden frame for testing in the railway environment

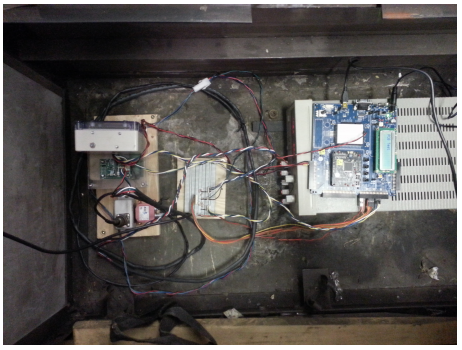

FIGURE 2.8: Sensor unit, power supply, and PSOC5 screwed to the floor beneath seats in the subway train

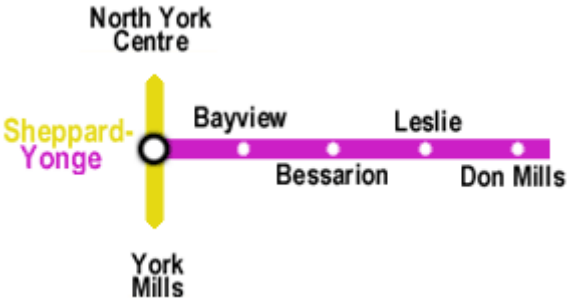

FIGURE 2.9: Shepphard subway line where the evaluation tests were performed

Chapter 3

Accelerometer Comparison

3.1 Accelerometer Selection

The primary objective of this chapter of the thesis was to identify a group of accelerometers that could be benchmarked and evaluated for potential in displacement estimation in a railway environment. The accelerometers are to be benchmarked against the Jewell Instruments LCA-165-5051, which is currently in use on-board subway trains. To this end, the companies that developed MEMS sensors at the time of research were identified and their most promising sensors were determined. In this section, the requirements and objectives put forth by the stakeholders are outlined. Furthermore, the manufacturers and sensors that have potential for evaluation are listed, followed by the decision-making process that led to a final group of eight sensors, including the Jewell, to be tested.

Some of the most important characteristics of accelerometers are listed below. The sensors' datasheets typically provide specifications for each of these characteristics. They are what make up the metrics for the device selection.

- **Measurement range:** The minimum and maximum accelerations the sensor can detect (ie. $\pm 2\,\mathrm{g}$) [8].
- **Sensitivity:** the ratio of change in acceleration to change in output signal. This can be expressed for analog sensors as a mV/g or for digital sensors as an LSB/g [8].
- **Noise density:** The square root of the power spectral density of the noise output [8].
- **Cross-axis sensitivity:** A measure of how much output is seen on one axis when acceleration is imposed on a different axis, specified as a percentage. The coupling between two axes results from a combination of alignment errors, etching inaccuracies, and circuit cross talk [8].

- **Nonlinearity:** A measurement of the deviation from a perfectly constant sensitivity, specified as a percentage with respect to full-scale range [8].
- **Package alignment error:** The angles between accelerometer-sensing axes and the referenced package feature [8].
- **Orthogonal alignment error:** deviation from the ideal angular displacement (90°) between two axes of the device [8].

3.1.1 Objectives and Requirements

A list of criteria was developed to rank the datasheet specifications of these sensors in order to narrow the number of accelerometers to within ten. The constraints and criteria that were identified are listed below in Table 3.1 and Table 3.2 and were developed jointly by the stakeholders in this project. Following the decision-making process, actual tests would be run and the best accelerometer would be chosen based on its performance against a different set of evaluation criteria.

Specification	**Minimum**	**Maximum**
Measurement Range	$-5\,\mathrm{g}$	$5\,\mathrm{g}$
Unit Price	\$0	\$350
Sampling Rate	$100\,\mathrm{Hz}$	$100\,\mathrm{Hz}$
Noise Density	$0\,\mu\mathrm{g}/\sqrt{\mathrm{Hz}}$	$200\,\mu\mathrm{g}/\sqrt{\mathrm{Hz}}$
Cross-Axis Sensitivity	$-2.0\,\%$	$2.0\,\%$
Nonlinearity	$-1.5\,\%$	$1.5\,\%$
Operating Temperature	$-40\,^{\circ}\mathrm{C}$	$85\,^{\circ}\mathrm{C}$
Storage Temperature	$-40\,^{\circ}\mathrm{C}$	$85\,^{\circ}\mathrm{C}$

Table 3.1: Constraints on accelerometer specifications

Specification	**Criterion**	**Weighting**
Sensitivity	Higher is preferred	5
Unit Price	Lower is preferred	5
Noise Density	Lower is preferred	10
Cross-Axis Sensitivity	Lower is preferred	8
Nonlinearity	Lower is preferred	10
Storage Temperature	A wider range is preferred	3
Number of axes	Higher is preferred	3
Integrated Gyroscope	Presence is preferred	3
Internal Temperature Sensor	Presence is preferred	5
Digital or Analog	Prefer digital	3
Ease of Evaluation	Existing platforms preferred	3

Table 3.2: Criteria on accelerometer specifications

3.1.2 Decision-Making Process

In order to begin the selection of accelerometers to be evaluated, a number of the most prominent sensor manufacturers was chosen and their most promising low-cost sensors were identified. The manufacturers identified from research in the industry are listed below.

- Analog Devices
- Bosch Sensortec (referred to throughout as Bosch)
- Colibrys
- Honeywell
- InvenSense
- Kionix
- Memsic
- STMicroelectronics

All Honeywell, InvenSense, and Memsic sensors had noise levels or prices that far exceeded the constraints shown in Table 3.1. From the remaining manufacturers, 56 sensors were identified to meet or closely meet the requirements. These sensors are shown in Appendix A. From these 56 sensors, measuring against the criteria provided in Table 3.2, 15 sensors were chosen with an effort to take at minimum one or two sensors from every manufacturer. These 15 devices and some key specifications are found in Table 3.3.

Manufacturer	**Accelerometer**	**Cost**	**Noise** ($\mu g/\sqrt{Hz}$)	**Output**
Analog Devices	ADIS16003	$23.00	110.00	Digital
Analog Devices	ADIS16300	$96.06	200.00	Digital
Analog Devices	ADIS16305	$133.35	225.00	Digital
Analog Devices	ADIS16445	$537.00	105.00	Digital
Analog Devices	ADXL203	$10.86	110.00	Analog
Analog Devices	ADXL313	$49.00	150.00	Digital
Bosch	BMA280	$1.46	120.00	Digital
Colibrys	MS7002.3	$330.00	14.00	Digital
Colibrys	MS9002.D	$290.00	18.00	Digital
InvenSense	MPU-6000	$15.00	400.00	Digital
Kionix	KXR94	$10.64	45.00	A or D
Kionix	KXRB5	$9.92	45.00	Analog
STMicroelectronics	LIS344ALH	$5.67	50.00	Analog
STMicroelectronics	LIS3LV02DL	$11.91	158.00	Digital
STMicroelectronics	LSM303DLHC	$5.02	220.00	Digital

TABLE 3.3: Fifteen accelerometers that met requirements

The fifteen accelerometers are further evaluated with the goal of evaluating between five and ten sensors. In order to rank these sensors, a Pugh chart was used, which scores each

sensor against the criteria listed in Table 3.2 and assigned each score the corresponding weight. The scores resulting from the Pugh chart is shown in Figure 3.1.

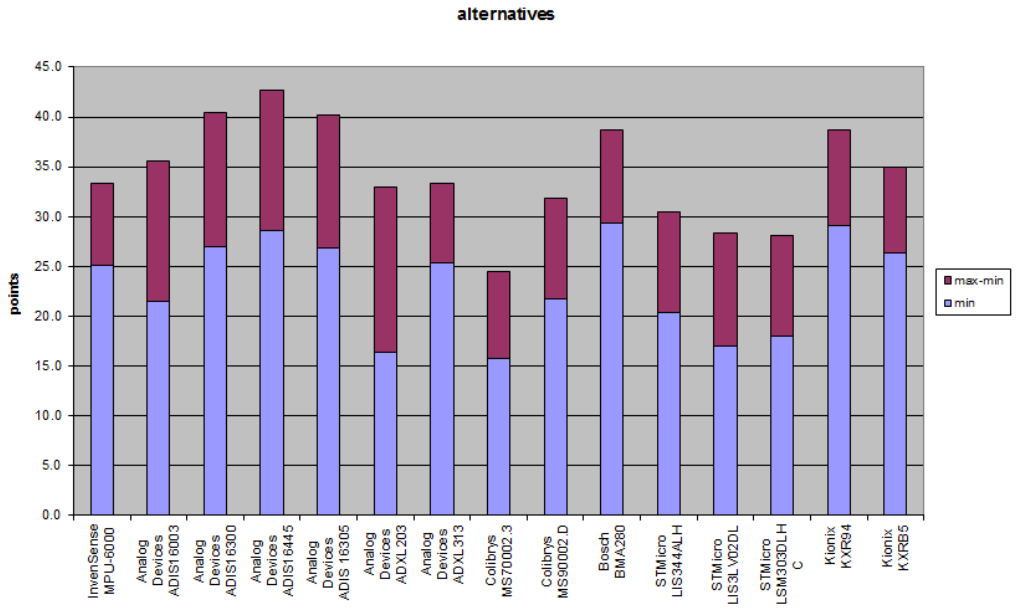

FIGURE 3.1: Scores obtained from Pugh chart for alternatives

3.1.3 Overview of Selected Accelerometers

The accelerometers outlined in Table 3.4 were chosen to be evaluated and benchmarked for this project. Table 3.4 also lists the reasoning for choosing each sensor. Further details on each are described in the section below.

Manufacturer	Accelerometer	Reasoning
Analog Devices	ADIS16305	Second best from AD, but much lower cost
Bosch	BMA280	Best from Bosch and very low-cost
Colibrys	MS9002.D	Best from Colibrys
Jewell Instruments	LCA-165-5051	Currently in use
Kionix	KXR94	Best from Kionix; evaluation board exists
Kionix	KXRB5	Similar to KXR94; data logger exists
STMicroelectronics	LIS344ALH	Best from STMicroelectronics
STMicroelectronics	LIS3LV02DL	In-House (AG-1 IMU)

TABLE 3.4: Accelerometers chosen for evaluation

3.1.3.1 Analog Devices ADIS16305

The ADIS16305 from Analog Devices is a three-axis digital acceleromter with a gyroscope. In order to test this device, the Analog Devices EVAL-ADIS Evaluation Board

was purchased. Using the supplied firmware, data from the ADIS16305 could be run in real-time and logged on a computer via a USB-to-Serial connection.

3.1.3.2 Bosch BMA280

The BMA280 is a 14-bit, three-axis, digital accelerometer that communicates via SPI or I2C interface. At this time of research, Bosch does not provide any evaluation boards to communicate with the chip and log data. A custom PCB was developed to breakout the chip pads to pins in order to communicate with the chip using the PSOC5.

3.1.3.3 Colibrys MS9002.D

The MS9002.D is a one-axis accelerometer chip with an analog output voltage between 0 and 5 volts. At the time of research, the manufacturer did not supply any evaluation boards or interfaces for this chip, so a custom PCB was designed that provided the chip with power and put the chip's output signals onto connector pins, which could be read in by an ADC, configured on the PSOC5.

3.1.3.4 Jewell LCA-165-5051

The Jewell Instruments accelerometer is a rugged one-axis analog accelerometer that operates on a $\pm 15\,\mathrm{V}$ power supply. This accelerometer is considered the highest quality as it is the most expensive accelerometer even though it is only one axis. A portion of this cost can be attributed to the packaging that the sensor comes encased in. An ADC is required to read and log the data from this sensor, so it was therefore connected to the PSOC5.

3.1.3.5 Kionix KXR94

The Kionix KXR94 sensor is a three-axis accelerometer that comes in either a digital or an analog package that had low noise and nonlinearity specifications. Furthermore, Kionix offered an evaluation kit and firmware for this sensor. However, there were issues with the zero-g bias of both chips that were purchased from Kionix and technical help from the company did not prove useful. Since accurate and correct data could not be obtained from this sensor, it was not put into any further tests.

3.1.3.6 Kionix KXRB5

The Kionix KXRB5 is a three-axis digital accelerometer that has very similar specifications as the KXR94. It was identified primarily because it was used in a data logger, the X2-2, from the company Gulf Coast Data Concepts (GCDC). This product logs the data output from the sensor and saves it to a microSD card, which can be processed later. Since there were implementation issues with the KXR94, the KXRB5 was considered an alternative candidate from the same manufacturer. This sensor may be called GCDC or GCDCXYZ in various figures throughout.

3.1.3.7 STMicroelectronics LIS344ALH

The LIS344ALH accelerometer is a three-axis analog output voltage accelerometer with a $\pm 2\,\mathrm{g}$ range. There is no evaluation board to log data from this accelerometer, but the manufacturer provides a breakout board (STEVAL-MKI015V1), which can be easily interfaced to an ADC. The PSOC5 was used to capture the analog data from this sensor.

3.1.3.8 STMicroelectronics LIS3LV02DL

The LIS3LV02DL is a three-axis digital accelerometer that was initially not included in the list of accelerometers to test. However, an accelerometer and gyroscope data logger (AG-1 from Icewire Technologies) was provided at no cost, which utilizes this accelerometer and logs data onto an SD card. Because of the ease of implementation and zero cost, this accelerometer was included in evaluation.

3.2 Evaluation Tests and Requirements

With eight sensors to be tested, a series of tests was needed to properly evaluate each sensor and compare them. Using some of the criteria identified in Table 3.2, tests were developed that would be able to verify datasheet specifications and quantitatively rank the accelerometers. Therefore, a new set of evaluation requirements was established, based off the various tests that were designed.

3.2.1 Evaluation Tests

3.2.1.1 Noise Characterization

Noise was identified as the most important criterion from the initial set and therefore consists of the first evaluation. The sensors were mounted onto the workbench and the output data was logged in intervals of approximately twenty seconds. This was done ten times. The noise density was calculated according to the following equation.

$$N_0 = \frac{\sigma}{\sqrt{BW}} \tag{3.1}$$

In this equation, N_0 is the spectral noise density, σ is the signal standard deviation and BW is the signal bandwidth. The noise density from each run was then averaged to obtain a final actual measurement of each sensor's noise density.

3.2.1.2 Off-Axis Motion

The cross-axis sensitivity is "a measure of how much output is seen on one axis when acceleration is imposed on a different axis, specified as a percentage" [8]. This definition assumes that, given that motion could be perfectly applied perpendicularly to the sensing axis, the sensing axis would then measure a percentage of this acceleration. The *off-axis* motion tests are developed to test the cross-axis sensitivity of the accelerometers, however the use of the term *off-axis* is used to explicitly state that this does not specifically test the cross-axis sensitivity of the sensor. This is because by mounting the devices into the evaluation platform, errors arise from small mounting angles and tilts and other mechanical imperfections associated with the evaluation platform and the workbench. Therefore, the off-axis sensitivity encompasses the cross-axis sensitivity, packing alignment error, orthogonal alignment error, mounting error, and other mechanical imperfections that are impossible to characterize quantitatively. The *off-axis* term in this report corresponds to one of the axes perpendicular to that of the sensing axis, most often the other horizontal axis (ie. x-axis for y-sensing-axis). In that sense, an off-axis motion is a motion perpendicular to the sensing axis and an on-axis motion is a motion in the direction of the sensing axis, as illustrated in Figure 3.2

The tests that were developed to quantify the off-axis error are to move the end-effector of the evaluation platform in the perpendicular direction of motion to the sensing axis. For the set-up with the coordinate frame of the platform, motion was applied in the x-direction while acceleration was sensed in the y-direction. The standard deviation of

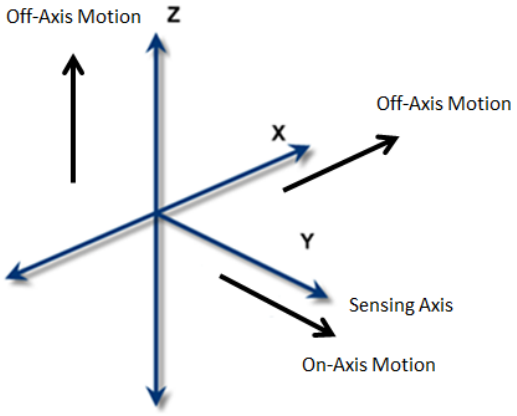

FIGURE 3.2: Off-axis motion and on-axis motion when the y-axis is the sensing axis

the output is used to quantify the amount of signal obtained from each sensor based on the same accelerations in the perpendicular direction.

3.2.1.3 Vibrations

The vibration tests are designed to test both the devices' ability to reject off-axis vibration motion as well as detect small vibrations in the direction of the sensing axis. This test moves the end-effector of the testing platform in all three directions at three different speeds. The standard deviation is measured during the off-axis vibrations to quantify the amount of error provided on the output of the sensing axis. Further, during the on-axis motion, the output is double-integrated to determine if accurate displacements of the vibration are obtained, with a final displacement of zero, since the end-effector returns to its original position at the end of each vibration.

3.2.1.4 Linear Step Motion

The linear step motion test is designed to determine the sensors' ability to estimate displacements by double integrating their output. The motion is applied on-axis by moving 5 cm to one direction. Then ten steps of 1 cm motion are applied in the other direction, with 400 ms pauses in between. The end-effector is then returned to its original position. Returning to the original position provides a simple method of determining the error, as final displacement should be zero.

3.2.1.5 Subway Train Tests

The sensors were brought onto subway trains at the Toronto Transit Committee (TTC) for testing in a railway environment. Six types of tests were designed for comparing the sensors to each other. They are described below.

- **Step Test:** The train was driven in one-direction, stopping every 150 m, for five intervals.
- **Shuttle Test:** The train travels to one point, then returns to the original point. This test was done in a subway station to have the most level track possible.
- **High Speed Test:** The train travelled at high speed from one station to another
- **Step and Return Test:** The train travelled from Bayview station to the end station (Sheppard-Yonge station). The train then returned, along the returning track, to the original station. In this test, when approaching the Sheppard-Yonge station the train had to stop three times to flip a switch in order to continue.
- **Full test:** The train travelled the entire Sheppard line, stopping at all station. During the actual test, the driver only slowed down at the first station, instead of coming to a complete stop.
- **Motionless test:** This test was designed to measure the noise output aboard the train to gauge how much more mechanical and electrical noise is present in the railway environment.

3.2.1.6 Thermal Tests

Operating in the railway environment in various climates, it is important that the sensors are able to function in a wide range of temperatures. The sensors were required to function between $-45\,^{\circ}\mathrm{C}$ and $85\,^{\circ}\mathrm{C}$. The sensors were put into a thermal chamber in order to test their functionality at these temperatures. The output bias and sensitivity of the sensor could be affected by the temperature. In order to differentiate between the two, the sensors were placed in the chamber mounted with the y-axis vertically (1 g on the y-axis, 0 g on the others). The zero-g axes would determine if the bias level is affected. The sensors were then placed at a 45° tilt (see Figure 3.3). With these two tests, it would be possible to determine if there is a correlation between bias and sensitivity changes and the temperature changes.

3.2.2 Evaluation Requirements

In order to remove sensors from evaluation and rank them, a set of requirements was developed, based on the evaluation tests that were described in the previous section.

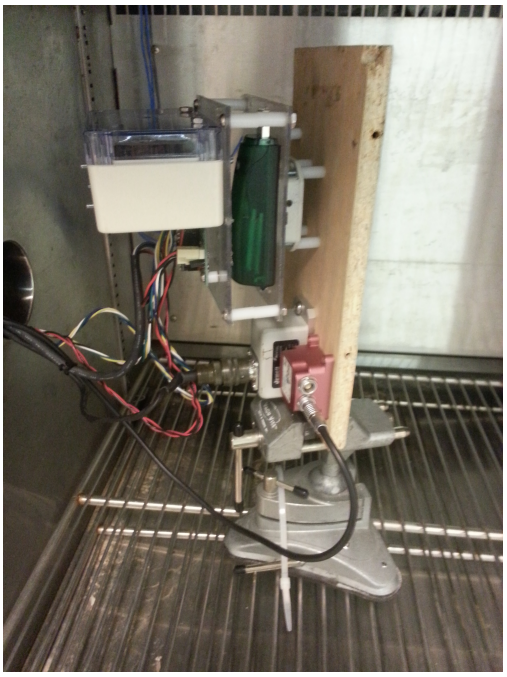

(A) Sensors mounted in thermal chamber with y-axis aligned with gravity

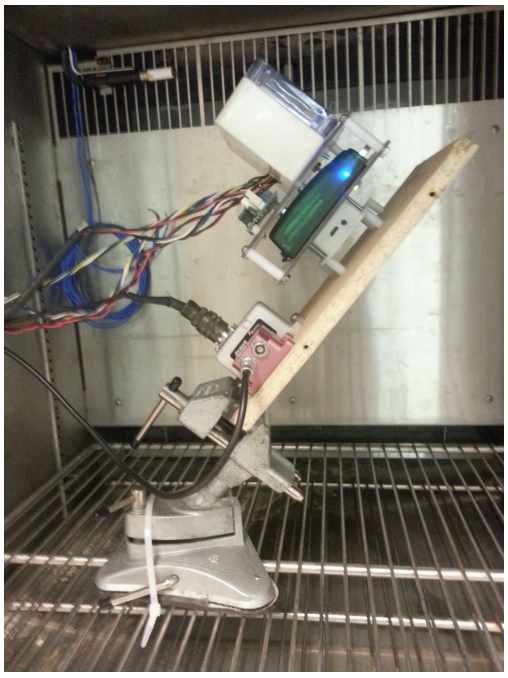

(B) Sensors mounted in thermal chamber with y-axis 45° to gravity

FIGURE 3.3: Thermal chamber mounting

The constraints are listed in Table 3.5. For each specification, the criteria is that the lower error is preferred. The weighting for each error quantity is also listed Table 3.5.

The double integration results are strongly dependent on the algorithms used. A very complex and sophisticated algorithm may be able to have great results for all sensors

Specification	**Constraint**	**Weighting**
Noise Density	$< 200\,\mu g/\sqrt{Hz}$	10
Cost	< \$300	8
Off-Axis Error	N/A	5
Vibration Error	N/A	5
Linear Step Motion Integration	N/A	5
Subway Step Test	N/A	3
Subway Shuttle Test	N/A	3
Subway High Speed Test	N/A	3
Subway Step and Return Test	N/A	3
Subway Full Test	N/A	3
Subway Motionless Test	$< 200\,\mu g/\sqrt{Hz}$	8
Thermal Test	$< 200\,\mu g/\sqrt{Hz}$	5
Digital or Analog	Prefer Digital	3

TABLE 3.5: Evaluation requirements for benchmarking

used, however would likely not be practical in real-time or in the subway control system. Therefore, in order to compare the results of displacement estimation, error was calculated with respect to the currently used accelerometer, the Jewell device. The following section will describe the algorithm used to perform double integration, which, for the purposes of comparison of the sensors themselves, is as simple as possible. This inertial algorithm, including integration and filtering, will be termed the *simple inertial algorithm*. In Chapter 4, more advanced algorithms will be explored to provide more precise estimation of displacement.

3.2.3 Simple Inertial Algorithm

3.2.3.1 Double Integration

The simple integration algorithm used includes a numerical double integration based on the trapezoidal rule as shown in Equation (3.2) and Equation (3.3).

$$\int_{t_1}^{t_2} v(t)dt \approx (t_2 - t_1)\frac{v(t_2) + v(t_1)}{2} \tag{3.2}$$

$$\int_{t_1}^{t_2} x(t)dt \approx (t_2 - t_1)\frac{x(t_2) + x(t_1)}{2} \tag{3.3}$$

3.2.3.2 Filtering

The primary filtering that was done was the implementation of an Finite Impulse Response (FIR) filter. The filter is a standard Hamming-window based, linear-phase filter

with cut-off frequency of 15 Hz and order 60. The filter eliminates the unwanted vibrations that are present on the subway trains and in any environment where unknown vibrations are present and reduces the noise level on the output of the sensors. The magnitude response of the filter is shown in Figure 3.4.

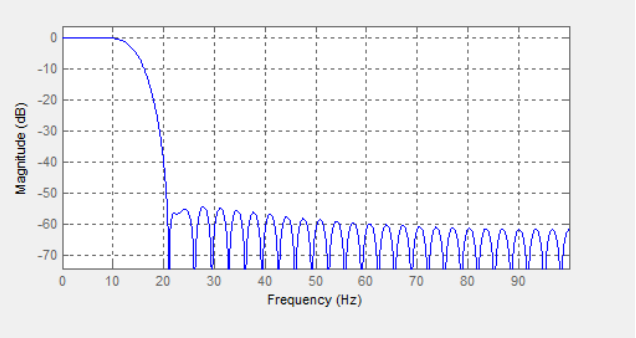

FIGURE 3.4: Magnitude response of the low-pass FIR filter with 15 Hz cut-off frequency and order 60

3.2.3.3 Bias Computation and Elimination

In order to accurately integrate acceleration, the zero-g bias must be removed from the output data. For the simple inertial algorithm, this occurs two times. The first bias correction takes the mean of the entire data set and subtracts the mean from the data. This correction gets the data near zero-g, which helps to align the data from the various sensors. This is necessary because the sensors are all started sequentially, a couple seconds apart.

Once the data is aligned, it is passed through the filter described above. Then the second bias correction stage is applied, in which the mean of the first second of data is removed from the data set. This ensures that all sensors have the first second of data corrected at zero-g to ensure an equal comparison during double integration.

3.2.3.4 Ground Truth from Video Data

In order to determine the ground truth during evaluation platform testing, the GoPro camera is used to take videos of the end-effector through motion. Using the calculated displacements from the circle-detection algorithm, the ground-truth is obtained. In order to compare these results with the acceleration results, we take the double derivative of the displacement to obtain velocity and acceleration. The ground-truth acceleration can then be considered as an *ideal* accelerometer and its output is then processed through the same inertial algorithm as the actual accelerometers. In addition, the computed *raw* displacements from the GoPro are plotted with the displacement estimations from the

accelerometers as well as the double-differentiated, then double-integrated, GoPro data to determine any errors in differentiation or integration algorithms.

3.2.3.5 Full Simple Inertial Algorithm

The full simple inertial algorithm is visually depicted in Figure 3.5.

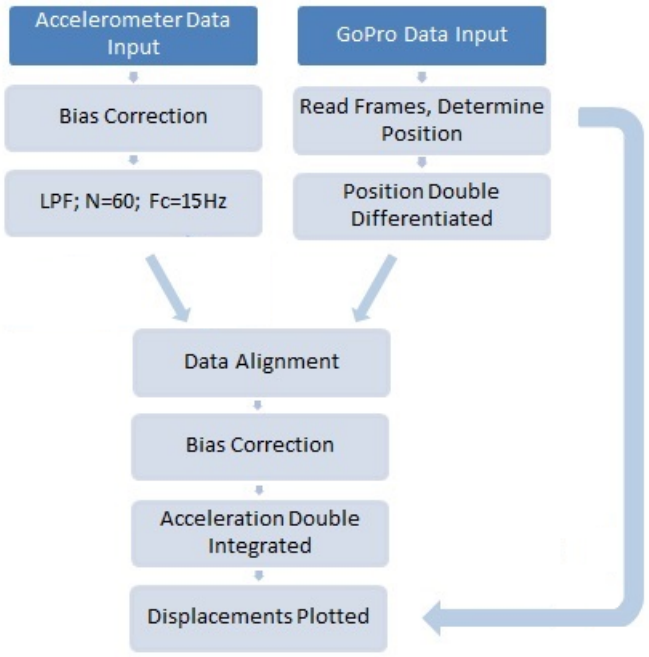

FIGURE 3.5: Block diagram of the simple inertial algorithm

3.3 Evaluation Results

3.3.1 Noise Results

The noise density of each sensor was measured to see how closely the sensor matches its datasheet. Noise measurements were performed in a stationary environment on the workbench. The results of the noise measurements are summarized in Table B.2 in order of lowest noise to highest noise with the datasheet specifications in the next column. Furthermore, the total noise is also shown, which is independent of the sampling frequency. The data obtained from these sensors for one of the ten noise runs can be seen in Figure 3.6, also presented in order of lowest to highest noise.

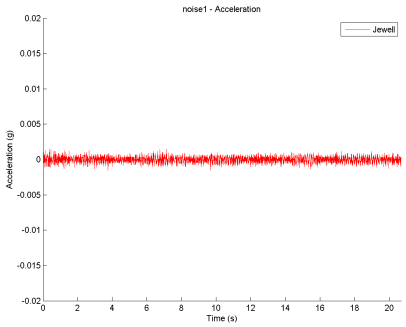

(A) Jewell motionless data

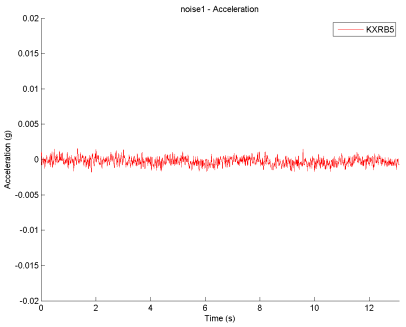

(B) KXRB5 motionless data

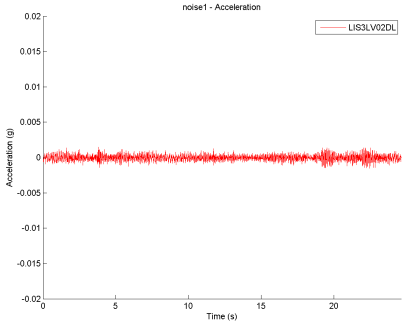

(C) LIS3LV02DL motionless data

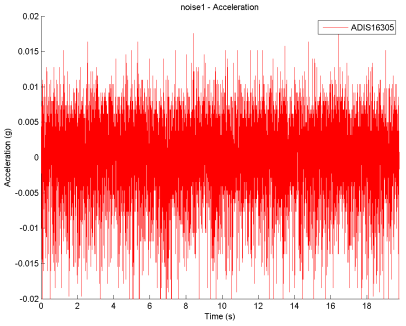

(D) ADIS16305 motionless data

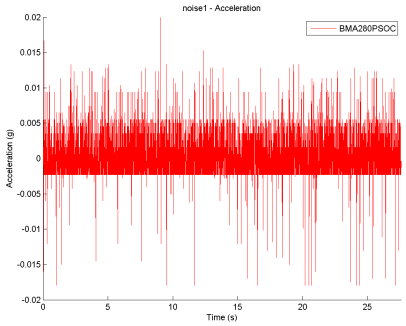

(E) BMA280 motionless data

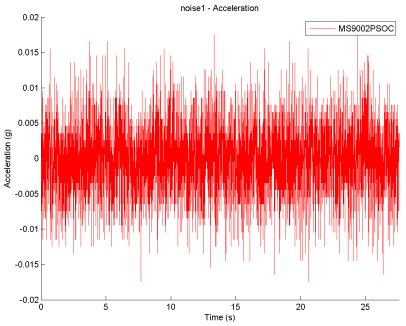

(F) MS9002.D motionless data

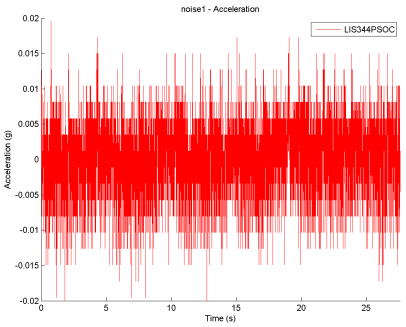

(G) LIS344ALH motionless data

FIGURE 3.6: Motionless data for sensors

The reason that the data in Figure 3.6d looks much noisier than others but has an

Accelerometer	**Measured Noise** ($\mu g/\sqrt{Hz}$)	**Datasheet Specification** ($\mu g/\sqrt{Hz}$)	**Total Noise** (μg)
Jewell	42.65	100.00	426
KXRB5	43.17	45.00	488
LIS3LV02DL	47.23	158.00	419
ADIS16305	289.77	225.00	5018
BMA280	333.86	120.00	3339
MS9002.D	563.93	18.00	5639
LIS344ALH	585.96	50.00	5860

TABLE 3.6: Noise measurements of the sensors compared to datasheet specifications

actual lower noise density is that the ADIS16305 is sampled at a much higher sampling rate, at approximately 600 Hz, while the the other sensors are sampled around 200 Hz. This higher sampling rate correspondingly lowers the noise density, as evident from Equation (3.1).

Only three of these eight sensors, the Jewell, the LIS3LV02DL and the KXRB5, meet the constraints listed in Table 3.5. The next steps for testing the sensors were to mount them onto the end-effector of the evaluation platform to test other characteristics such as cross-axis sensitivity and inertial displacement estimation potential. The sensors that did not meet the noise constraints are not included in the results for the next tests for simplicity and conciseness of the report, since the noise level significantly affects other tests. However, for completeness, the results are included in Appendix B. The scores for the sensors that meet the noise constraints are shown in Table 3.7.

Accelerometer	**Score (out of 100)**
Jewell	79
KXRB5	78.5
LIS3LV02DL	76.5

TABLE 3.7: Scores assigned to the devices from noise evaluation

3.3.2 Off-Axis Error Results

Noise density of the sensors was one of the highest weighted criteria that were outlined by the stakeholders. Another heavily weighted criterion was cross-axis sensitivity. This is defined as the amount of acceleration measured on an axis when an acceleration is applied to another axis, perpendicularly. In an ideal testing environment, motion would be applied perfectly perpendicularly to the axis being measured, however due to

mounting errors and slight tilts of the workbench or end-effector, this is impossible. The best effort was made to mount the sensors precisely for these tests.

The test in itself consists of moving the end-effector back and forth in the x- and z-axes. The y-axis is the output being tested. One test moved the end effector in the x-axis while measuring the y-axis output. The second test moved the end effector in the z-axis three times, at different speeds (slow, medium, and fast), and this was done twice. The metrics chosen to determine the amount of error on the output are the noise density during measurement, the maximum signal measured, and the signal power. The noise density is calculated in the same manner as in Equation (3.1). The maximum absolute signal is the maximum positive or negative acceleration sensed during the measurement. The signal power is an average of the signal energy over time, calculated according to Equation (3.4).

$$P = \frac{1}{t_2 - t_1} \int_{t_1}^{t_2} (|a(t)|)^2 dt \tag{3.4}$$

The results of these tests are summarized in Table 3.8.

Test	**Accelerometer**	**Measured Noise** ($\mu g/\sqrt{Hz}$)	**Maximum Signal** (mg)	**Signal Power** (g^2)
X-Axis	Jewell	37720	0.170	0.01400
X-Axis	LIS3LV02	19945	0.094	0.00390
X-Axis	KXRB5	15228	0.076	0.00230
Z-Axis Slow	Jewell	10411	0.036	0.00107
Z-Axis Slow	LIS3LV02	6464	0.018	0.00042
Z-Axis Slow	KXRB5	5076	0.015	0.00028
Z-Axis Medium	Jewell	43246	0.172	0.01820
Z-Axis Medium	LIS3LV02	11286	0.073	0.00120
Z-Axis Medium	KXRB5	9067	0.040	0.00080
Z-Axis Fast	Jewell	37411	0.229	0.01370
Z-Axis Fast	LIS3LV02	21737	0.117	0.00460
Z-Axis Fast	KXRB5	15956	0.095	0.00250
Average	Jewell	32197	0.152	0.01174
Average	LIS3LV02	14858	0.076	0.00253
Average	KXRB5	11331	0.056	0.00147

TABLE 3.8: Quantitative results from off-axis testing

As can be seen from the results, the KXRB5 is the sensor that rejects off-axis motion the best, followed by the LIS3LV02DL, then the Jewell. The scores assigned to each sensor for their performance in the off-axis error specification are shown in Table 3.9.

Accelerometer	Score (out of 100)
Jewell	60
KXRB5	95
LIS3LV02DL	90

TABLE 3.9: Scores assigned to the devices from vibration evaluation

3.3.3 Vibration Results

The vibration tests moved the devices in all three axes at three different speeds. In order to quantify the sensors' ability to reject off-axis vibrations and on-axis vibration, the same metrics as in the off-axis error tests were used. They are the noise level, the maximum absolute signal, and the signal power. The raw data from the tests is shown in Figure 3.7.

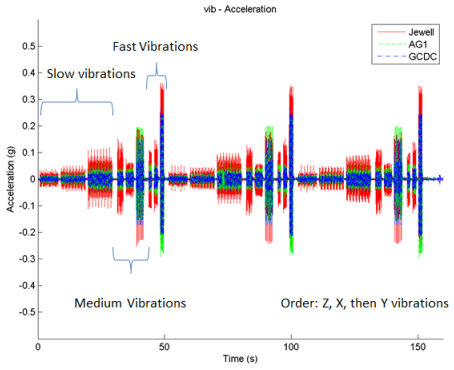

FIGURE 3.7: Raw data for three sensors during vibration testing

The quantitative results from the raw data in Figure 3.7 is summarized in Table 3.10. In all cases, a lower number is preferred.

Accelerometer	Measured Noise ($mg/\sqrt{Hz}$)	Maximum Signal (mg)	Signal Power (g^2)
Jewell	38.03	119.96	24.12
KXRB5	38.35	116.32	25.61
LIS3LV02DL	31.04	91.28	21.39

TABLE 3.10: Quantitative results from vibration testing

To summarize the results from Table 3.10, the LIS3LV02DL sensor has the best ability to reject vibration signal by having the lowest measured noise, lowest maximum signal, and lowest signal power. The scores resulting from vibration results are shown in Table 3.11.

Accelerometer	Score (out of 100)
Jewell	80
KXRB5	80
LIS3LV02DL	95

TABLE 3.11: Scores assigned to the devices from vibration evaluation

3.3.4 Step Motion Results

During the step motion tests, the end-effector was brought to the location $y = -10\,\text{cm}$, then moved across the stage to $y = 10\,\text{cm}$ in intervals of $1\,\text{cm}$, with pauses of $400\,\text{ms}$ in between each interval. The end-effector was then brought back to the initial position at $y = 0\,\text{cm}$.

Using the simple inertial algorithm, the output of the accelerometers was double integrated to obtain displacement. The test was performed three times in a row. The raw data obtained from the test is shown in Figure 3.8.

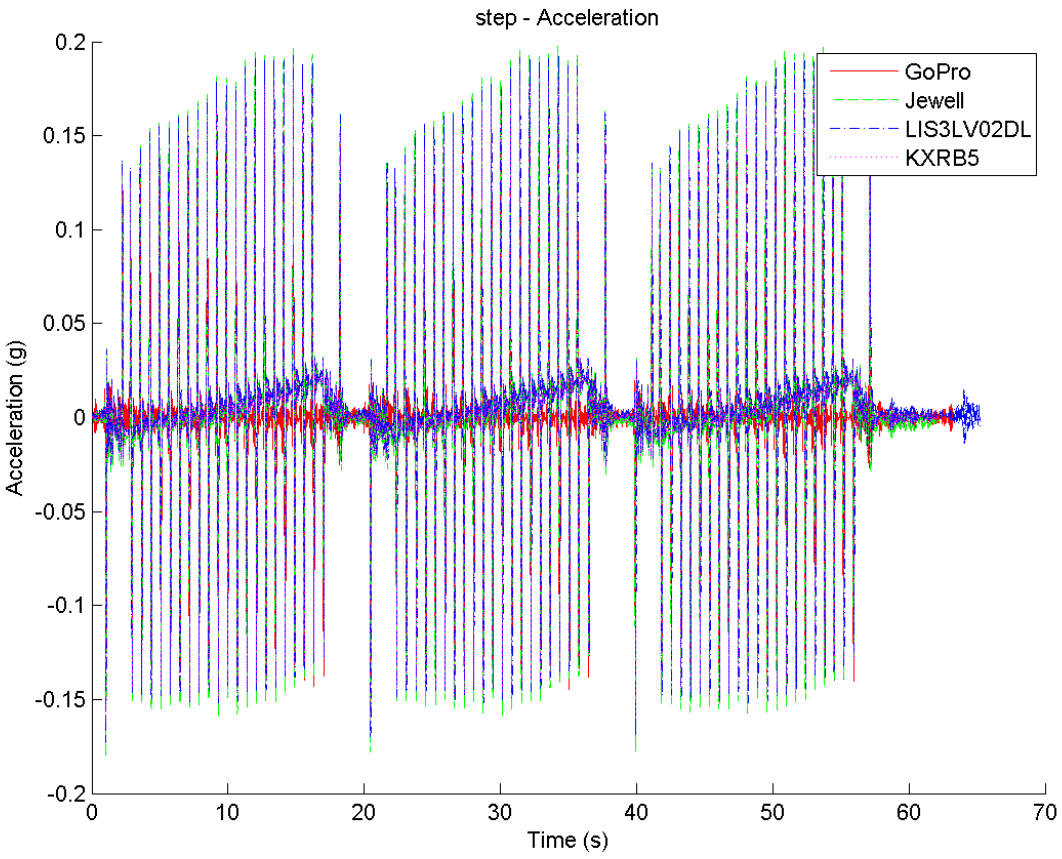

FIGURE 3.8: Raw data for three sensors during step motion testing

The GoPro camera was used to determine the ground-truth of the end-effector throughout the test. This shows the actual motion that the devices underwent. The devices are contrasted against this ground-truth in order to compare their performance, based on several metrics. The quantifiable metrics are: the displacement power and the velocity power. The power of a signal is calculated according to Equation (3.5).

$$P = \sum_{n=n_1}^{n_2} |a[n]|^2 \tag{3.5}$$

For the individual tests, the results are shown in Figure 3.9. The results are further quantified in Table 3.12

Accelerometer	**Final Velocity** (m/s)	**Velocity Power** (m^2/s^2)	**Final Displacement** (m)	**Displacement Power**(m^2)
Jewell	0.666	1.736	-0.384	43.125
KXRB5	0.669	1.633	-0.02	32.636
LIS3LV02DL	0.975	2.919	2.887	14.390

TABLE 3.12: Quantitative results from step testing, averaged for three individual runs

The results from Table 3.12 would suggest that the LIS3LV02DL performs the best amongst the three sensors, as it has lower velocity and displacement power. However, having a final velocity higher than the other two sensors is a very significant downfall. If the data is integrated through all three tests at once, as shown in Figure 3.10, it is clear why this is the case.

The final displacement and velocity of the LIS3LV02DL is much larger compared to the other three sensors when the three tests are put together. Although the individual tests would suggest LIS3LV02DL to be the best sensor in this case, the full integration shows that this is not the case. This is shown in Table 3.13, where the full measurement velocity and displacement powers are shown.

Accelerometer	**Final Velocity** (m/s)	**Velocity Power** (m^2/s^2)	**Final Displacement** (m)	**Displacement Power**(m^2)
Jewell	1.96	45.80	37.49	12707
KXRB5	1.99	46.79	38.29	13250
LIS3LV02DL	2.96	121.50	66.72	44657

TABLE 3.13: Quantitative results from step testing for three runs in a row

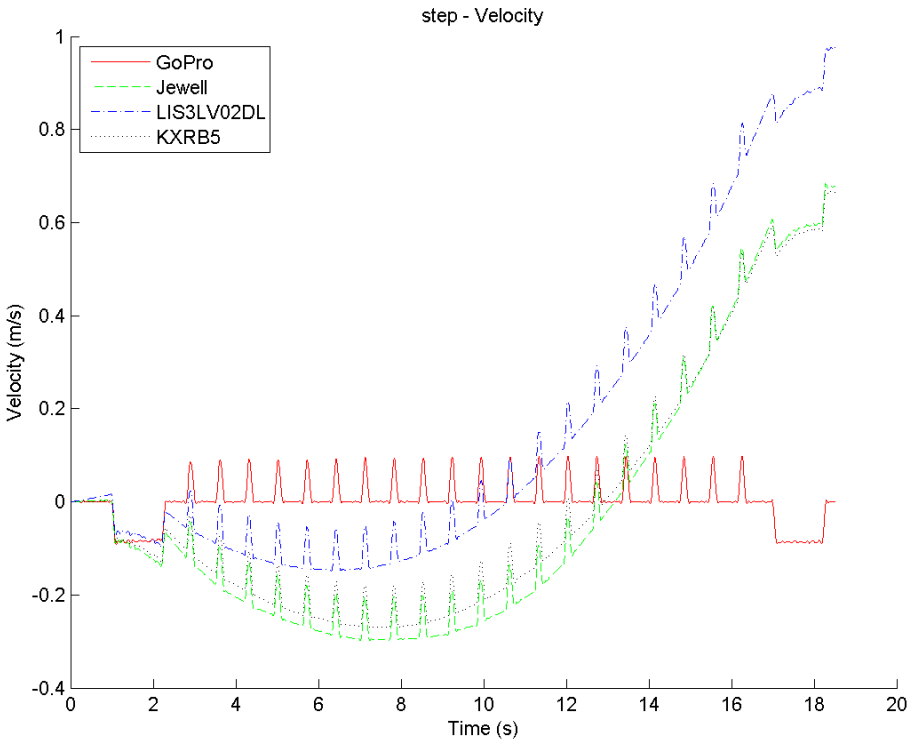

(A) Single integration of acceleration to obtain velocity

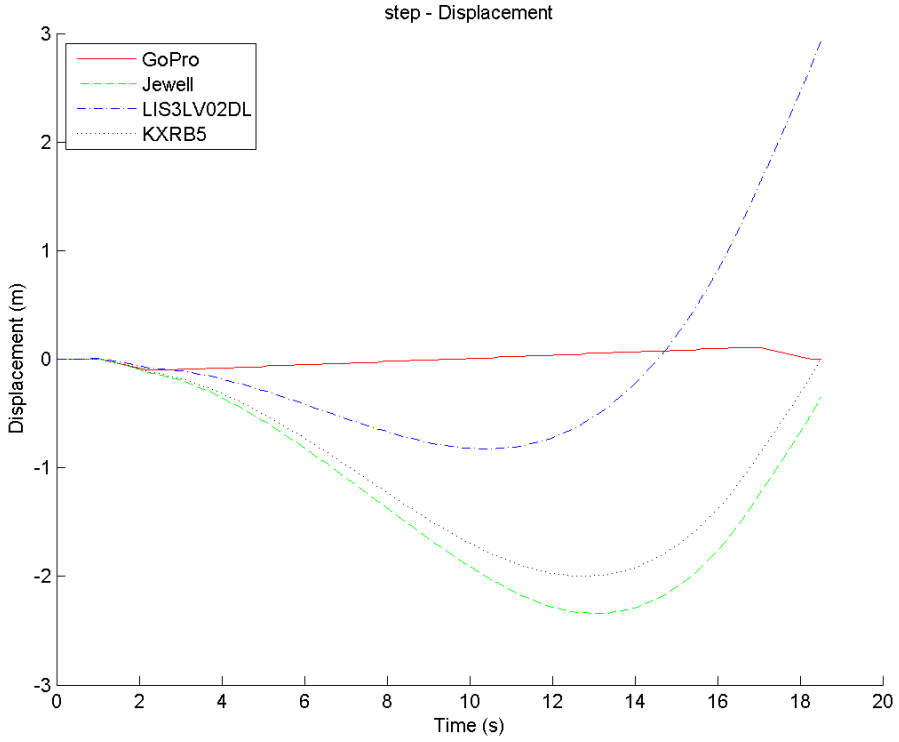

(B) Double integration to obtain displacement

FIGURE 3.9: Results of double integration for one step motion run

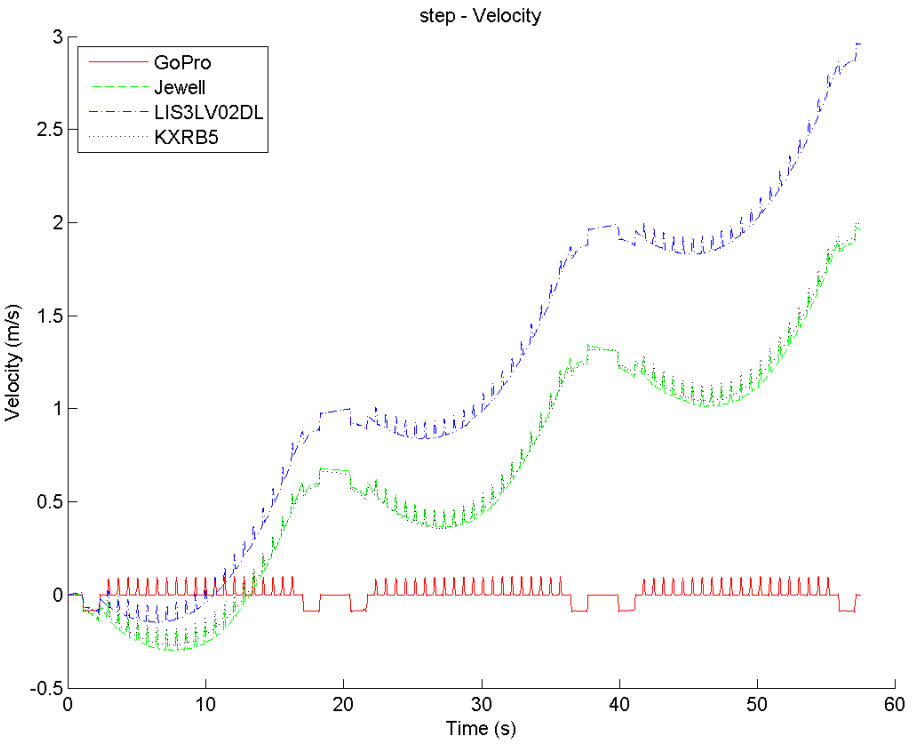

(A) Single integration to obtain velocity

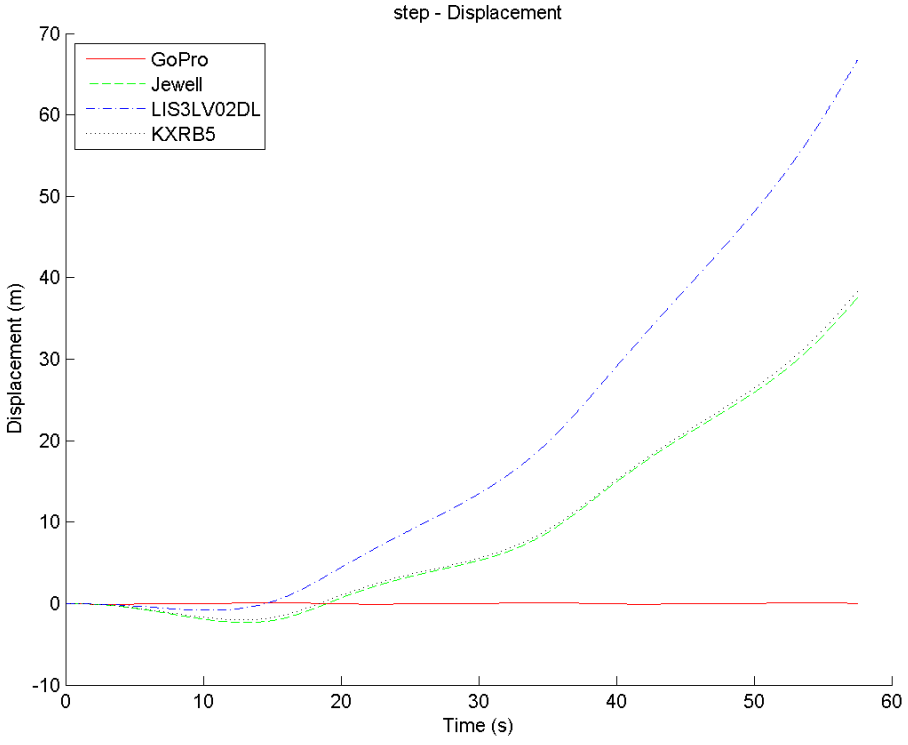

(B) Double integration to obtain displacement

FIGURE 3.10: Results of double integration for all three step runs in a row

From these results, it is clear that the KXRB5 sensor has the best performance, followed closely by the Jewell. The scores assigned to each sensor in this category are shown in Table 3.14.

Accelerometer	**Score (out of 100)**
Jewell	90
KXRB5	95
LIS3LV02DL	75

TABLE 3.14: Scores assigned to the devices from step motion evaluation

3.3.5 Subway Test Results

There were five subway tests used to evaluate the sensors: the step test, the shuttle test, the step-and-return test, the high speed test, and the motionless test. The step test was performed four times, the shuttle test was performed once, the step-and-return test was performed twice, and the high speed test was performed twice. The motionless test was ran for over 200 seconds to obtain a measurement of the noise density on-board the subway train.

Raw data from the noise measurements can be seen in Figure 3.11.

The LIS3LV02DL maintains the least noise followed by the KXRB5, as the results in Table 3.15 show. These sensors are both digital, while the Jewel is an analog sensor. There is possibility of electrical noise being induced onto the cables connecting to the Jewel, which could account for its weaker performance in this category.

Accelerometer	**Measured Noise** ($\mu g/\sqrt{Hz}$)	**Datasheet Specification** ($\mu g/\sqrt{Hz}$)	**Total Noise** (μg)
Jewell	112.91	100.00	1129
KXRB5	54.31	45.00	457
LIS3LV02DL	40.38	158.00	361

TABLE 3.15: Noise measurements of sensors on stationary subway train

The step test consisted of five movements of 150 m each. The actual displacement was approximately 760 m. The raw data obtained from the three sensors for one of these runs can be seen in Figure 3.12.

The shuttle test was a single movement approximately 140 m each through a station, followed by a movement back to the original position. The raw data obtained from the three sensors in this one run is shown in Figure 3.13.

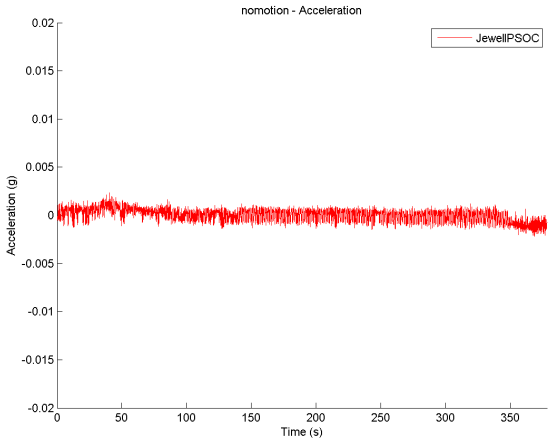

(A) Jewell stationary noise on the subway train

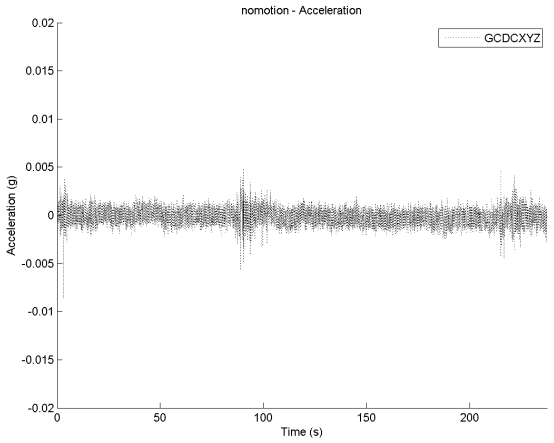

(B) GCDC stationary noise on the subway train

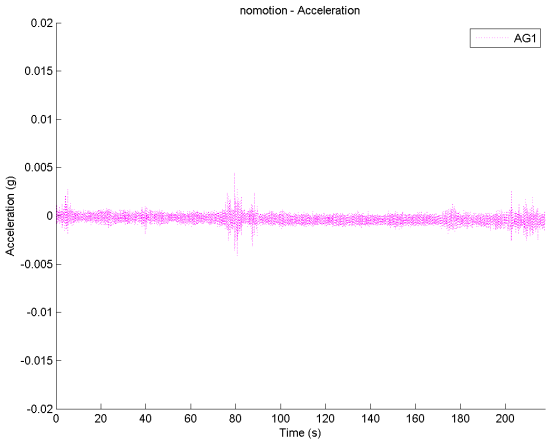

(C) AG1 stationary noise on the subway train

FIGURE 3.11: Raw data measurements of stationary subway noise

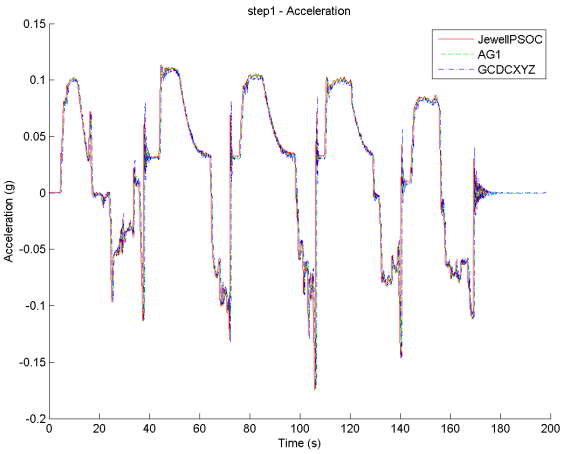

(A) Step test acceleration

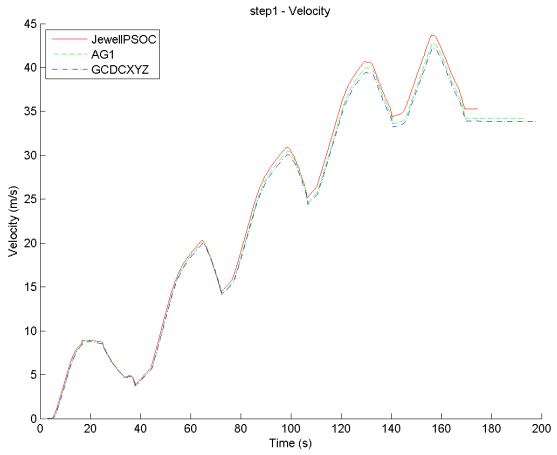

(B) Step test velocity

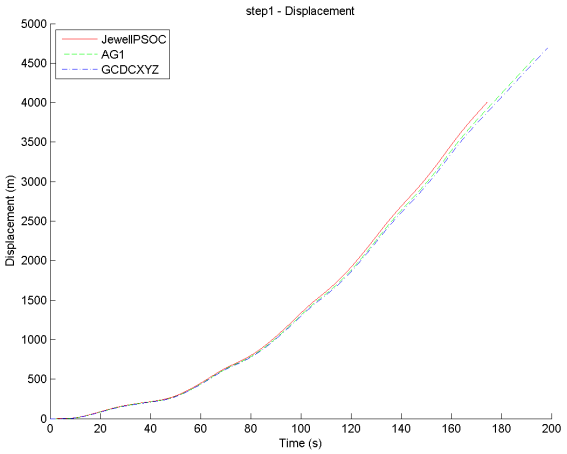

(C) Step test displacement

FIGURE 3.12: Raw data measurements of subway step test

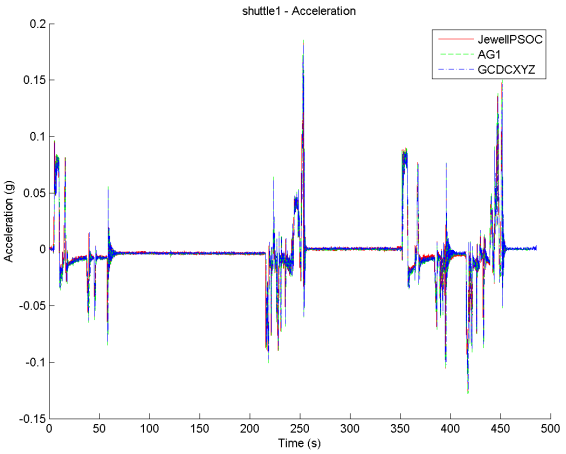

(A) Shuttle test acceleration

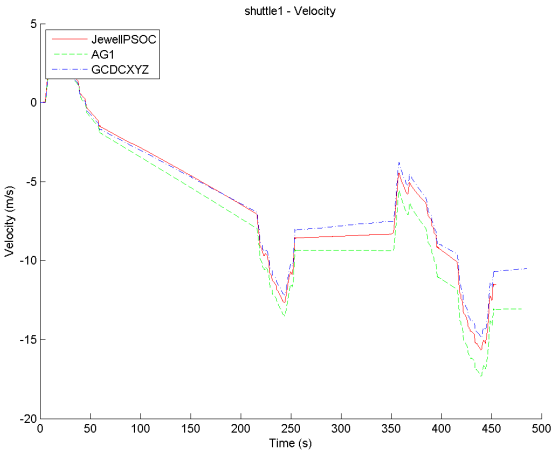

(B) Shuttle test velocity

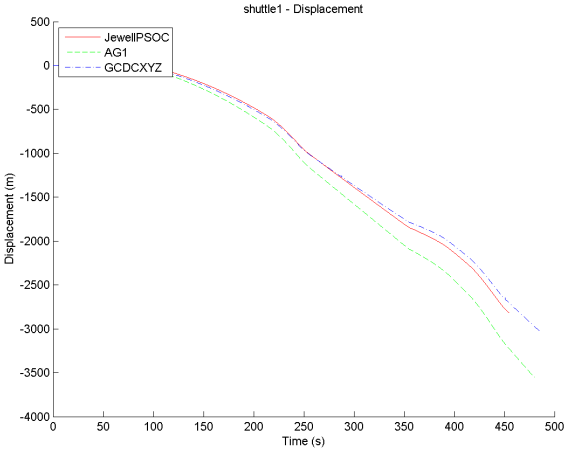

(C) Shuttle test displacement

FIGURE 3.13: Raw data measurements of subway shuttle test

The step-and-return test started at Bayview station, travelled towards Yonge station, and then returned to Bayview station. Both stations are 2000 m apart, totalling 4000 m of travelled distance. The raw data from one of the two runs is shown in Figure 3.14.

During the high speed test, the subway train was brought up to its maximum speed (approximately 55 km/h) and travelled from one station to the other. The raw data from one of the high speed runs is shown in Figure 3.15.

The output for each run was double-integrated using the simple inertial algorithm to estimate the displacement. In order to compare the sensors, final velocity and displacement values were calculated. However, these results utilize a very simple inertial algorithm that has poor performance. Therefore, to normalize the results, the error is calculated as a difference between the sensors' output and the Jewell's output, then divided by the Jewell output, providing a percentage error value. The results of the all of the tests are summarized in Table 3.16.

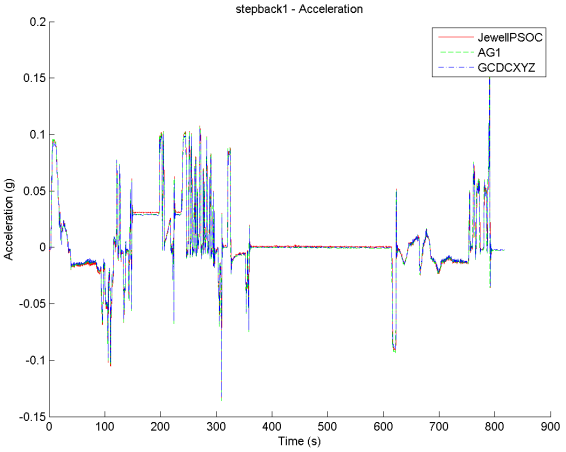

(A) Step-and-teturn test acceleration

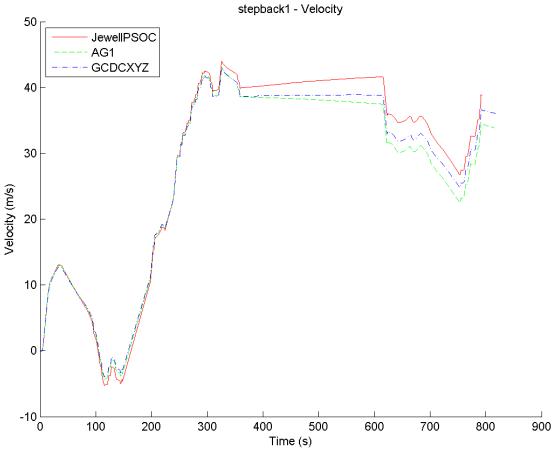

(B) Step-and-teturn test velocity

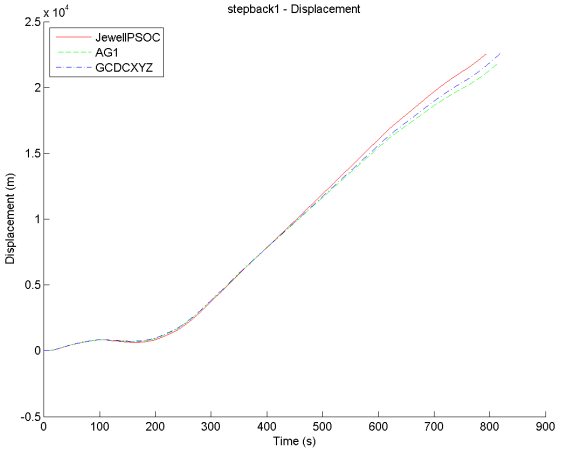

(C) Step-and-teturn test displacement

FIGURE 3.14: Raw data measurements of subway step-and-return test

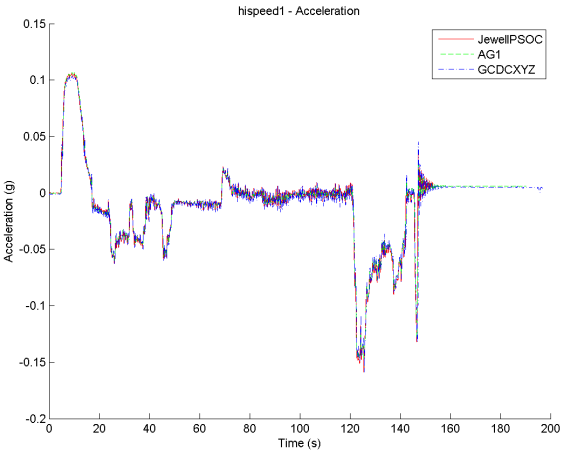

(A) High speed test acceleration

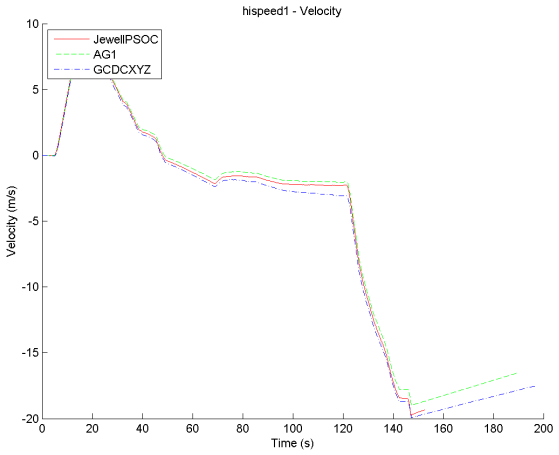

(B) High speed test velocity

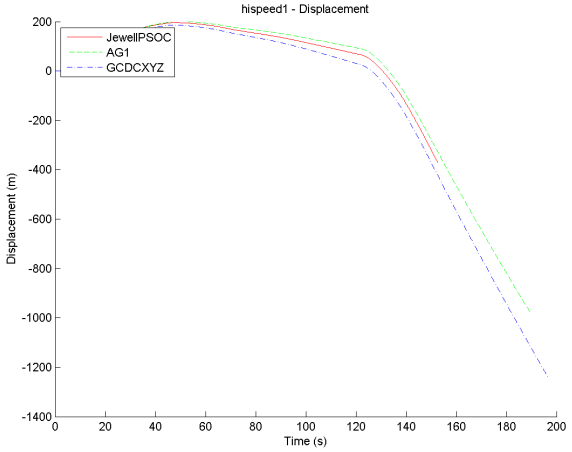

(C) High speed test displacement

FIGURE 3.15: Raw data measurements of subway shuttle test

Test	**Device**	**Velocity Error (m/s)**	**Velocity Percent Error (%)**	**Displacement Error (m)**	**Displacement Percent Error (%)**
Step 1	KXRB5	1.41	4	128.75	3
Step 1	LIS3LV02DL	1.06	3	84.08	2
Step 2	KXRB5	0.53	2	35.56	2
Step 2	LIS3LV02DL	0.45	2	30.71	2
Step 3	KXRB5	0.23	1	38.47	1
Step 3	LIS3LV02DL	0.26	1	7.06	0
Step 4	KXRB5	0.05	0	24.95	0
Step 4	LIS3LV02DL	0.00	0	9.31	0
Average	KXRB5	0.55	2	56.93	2
Average	LIS3LV02DL	0.44	0	32.79	1
Shuttle	KXRB5	0.85	7	115.39	4
Shuttle	LIS3LV02DL	1.57	14	404.08	14
Step and Return 1	KXRB5	2.27	6	914.53	4
Step and Return 1	LIS3LV02DL	4.36	11	1459.48	6
Step and Return 2	KXRB5	3.50	12	1037.30	6
Step and Return 2	LIS3LV02DL	1.57	5	528.13	3
Average	KXRB5	2.89	9	975.92	5
Average	LIS3LV02DL	2.96	8	993.80	5
High Speed 1	KXRB5	0.31	2	52.62	14
High Speed 1	LIS3LV02DL	0.66	3	41.66	11
High Speed 2	KXRB5	0.25	2	36.38	18
High Speed 2	LIS3LV02DL	0.46	3	65.62	33
Average	KXRB5	0.28	2	44.50	16
Average	LIS3LV02DL	0.56	3	53.64	22

TABLE 3.16: Quantitative results from various subway tests

Examining the results from Table 3.16, it is difficult to say whether one of the sensors performs better than the other. The LIS3LV02DL performs better on average in the step test, however the KXRB5 performs better on average in the other three tests.

In these results, the sensors are rated relative to the Jewell. However, the Jewell has significant error itself and possibly more than the other two sensors. Therefore it is useful to compare the final displacements of each sensor for the tests in which the approximate

actual displacements are known. The results are summarized in Table 3.17, where the total error for the displacement estimation is shown. Averages are taken for the tests that had multiple runs.

Test	**Accelerometer**	**Displacement** (m)	**Actual Displacement** (m)	**Displacement Error**(m)
Step	Jewell	3642	760	2882
Step	KXRB5	3585	760	2825
Step	LIS3LV02	3609	760	2849
Shuttle	Jewell	-3691	0	3691
Shuttle	KXRB5	-3057	0	3057
Shuttle	LIS3LV02	-3482	0	3482
Step-and-Return	Jewell	19310	0	19310
Step-and-Return	KXRB5	19371	0	19371
Step-and-Return	LIS3LV02	18844	0	18844

TABLE 3.17: Absolute error during subway tests

From the absolute error results shown in Table 3.17, all three sensors have a large amount of error from the simple inertial algorithm. Because the bias estimation is inaccurate using this algorithm, large integration drift error is present. However, the sensors are consistent amongst themselves, with final displacements being only a small percentage different from each other. This suggests that the sensors perform similarly, but a more intelligent algorithm may be needed to accurately estimate the displacement from the acceleration data.

In addition, it must be taken into account that there were possible mounting errors, which would make the sensing axis of each sensor misaligned with the direction of motion. This could have a significant effect in reducing or increasing the error in the results, though it is impossible to quantify this error. Care was taken in mounting the sensors parallel to the side of the train, though imperfections would remain.

The next section will introduce advanced algorithms that obtain better estimations of displacements. These results serve only to demonstrate that with the most simple algorithms, the results from the three sensors is very similar. In fact, the low-cost sensors have lower displacement error on average. The scores for the sensors for the TTC trials are summarized in Table 3.18. Because of the fact that it is very difficult to compare the sensors from these evaluations due to the simple inertial algorithm used, the subway testing criteria are weighted lower than the rest, except for the stationary noise measurement.

Test	**Accelerometer**	**Score (out of 100)**
Noise	Jewell	50
Noise	KXRB5	80
Noise	LIS3LV02	75
Step	Jewell	45
Step	KXRB5	55
Step	LIS3LV02	50
Shuttle	Jewell	40
Shuttle	KXRB5	60
Shuttle	LIS3LV02	50
Step-and-Return	Jewell	50
Step-and-Return	KXRB5	45
Step-and-Return	LIS3LV02	60
High Speed	Jewell	50
High Speed	KXRB5	55
High Speed	LIS3LV02	45

TABLE 3.18: Scores for the various subway evaluations

3.3.6 Thermal Testing Results

The sensors were tested at the Thales office in an industrial thermal chamber. The main factor that was immediately noted was that when the thermal chamber was turned on, a substantial amount of vibrations was present due to the heating and cooling systems. This mechanical noise was then seen on the output of all of the accelerometer sensors. Secondly, there is the possibility that some electrical noise was also induced on the output of the sensors. Thirdly, as can be seen from Figure 3.3, some of the sensors were mounted above others. When the main block of wood undergoes vibrations, they are propagated to the devices on the upper levels and the vibrations are amplified there. A last issue is that the devices logged data in many different manners, as we had two different off-the-shelf dataloggers, one custom PCB, and two rugged analog accelerometers mounted at the same time. The GCDC data logger was unable to completely log cold temperatures as it went into an error mode, which could not be reset until the battery died. This prevented full testing of the Kionix KXRB5 chip.

Due to the combination of these factors, the thermal testing was largely inconclusive. However, plots of the data from the sensors is available in Appendix B, which shows some variance in the sensor data during testing. It is not clear unfortunately if there is a direction relation between temperature changes and acceleration changes, which makes it impossible to compensate for these changes. Further thermal testing is recommended to ensure that the selected device can successfully perform in the required temperature range.

3.4 Evaluation Summary

In order to recommend a low-cost device for use in the railway environment, a score was assigned to each device that met constraints in each criterion from Table 3.5. The scores for the devices are shown in Table 3.19.

Characteristic	Weight	Jewell	KXRB5	LIS3LV02DL
Noise Density	10	79	78.5	76.5
Unit price	8	0	100	100
Off-Axis Error	5	60	95	90
Vibration Error	5	80	95	80
Step Integration	5	90	95	70
Subway Step	3	45	55	50
Subway Shuttle	3	40	50	60
Subway High Speed	3	50	55	45
Subway Step and Return	3	50	45	60
Subway Noise	8	50	80	85
Thermal	5	N/A	N/A	N/A
Digital or Analog	3	0	100	100

TABLE 3.19: Summary of all scores for the evaluation requirements

These scores are then multiplied by the assigned weights and a final score for each device is calculated. The final score for each device can be seen in Figure 3.16.

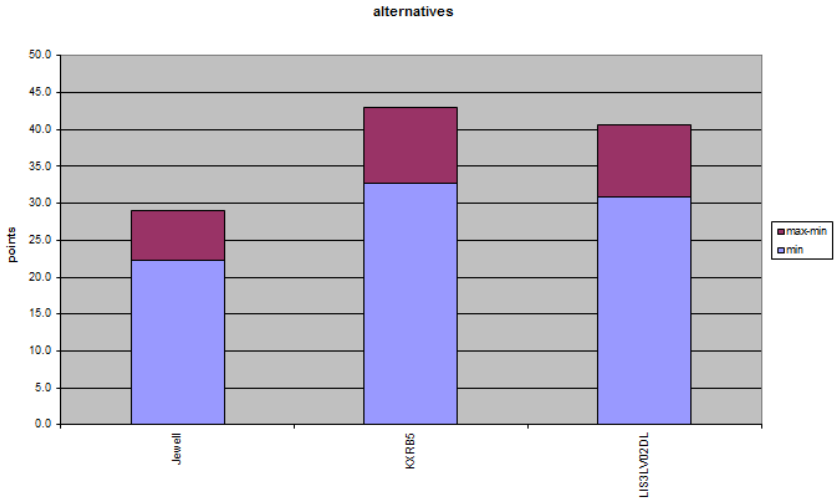

FIGURE 3.16: Decision-making results, based on the assigned score and weight for each requirement

As can be seen from Figure 3.16, the KXRB5 sensor has the highest score calculated from its performance in the various evaluation tests. The LIS3LV02DL performs very similarly to the KXRB5 and could certainly be considered as an alternative for the Jewell replacement. Although the final score shows the Jewell performing significantly worse

than the other two devices, this is primarily because the cost of the device is included in this selection process. In this category, the Jewell scores zero. However, it is important to note that the Jewell is an off-the-shelf device that is ready for implementation at its stated cost. In contrast, both the KXRB5 and the LIS3LV02DL require an amount of electrical and mechanical design in order to obtain the data from the digital sensors and ruggedize the components for an industrial and automotive environment. ***The final recommendation for further investigation and implementation in the railway environment is the Kionix KXRB5.***

Chapter 4

Inertial Algorithms

This section of the thesis describes the methods that were used to improve the results of double integration of the acceleration data to obtain displacement. The key problem to be solved is bias estimation. The biggest challenge to be addressed in determining displacements from acceleration signals is to remove the undesired gravity component from the output. Unfortunately, the largest expected accelerations in the railway environment reach approximately 0.15 g, which is kess than a fifth of the acceleration due to gravity. Any component of gravity that is present due to an unknown tilt of the sensors cannot be eliminated will provide unwanted integration drift error. Any slight tilts of the sensors put a component of gravity on the output. As a simple example, a relatively small tilt of 5 degrees will provide an unwanted signal of $\cos(5 * \text{pi}/180) = 0.0872\,\text{g}$, which is over 50% of our expected signal. Unfortunately, although the gradient of railway tracks is known, there are unknown tilts applied to the train and sensors during motion due to the suspension system and braking mechanics. Therefore, during motion, a combination of acceleration due to gravity from an unknown tilt and acceleration due to motion is seen on the sensor output.

It was observed throughout testing that during periods of no motion, the zero-g bias of the accelerometers varied from position to position. On the evaluation platform, this bias was approximately consistent for every coordinate in the workspace. However, in the railway environment, the movement of the subway train is less consistent and is more dynamic. Figure 4.1 shows a test in which the subway train moved forward and stopped at different points. Highlighted are the points of no motion, where the zero-g bias of the accelerometer is significantly different at each stop.

Many efforts [4] [5] [6] have gone into using gyroscope, magnetometers, and inclinometers with sensor fusion algorithms in order to precisely know the orientation of an IMU at all times and effectively remove the gravity component of acceleration. Although some

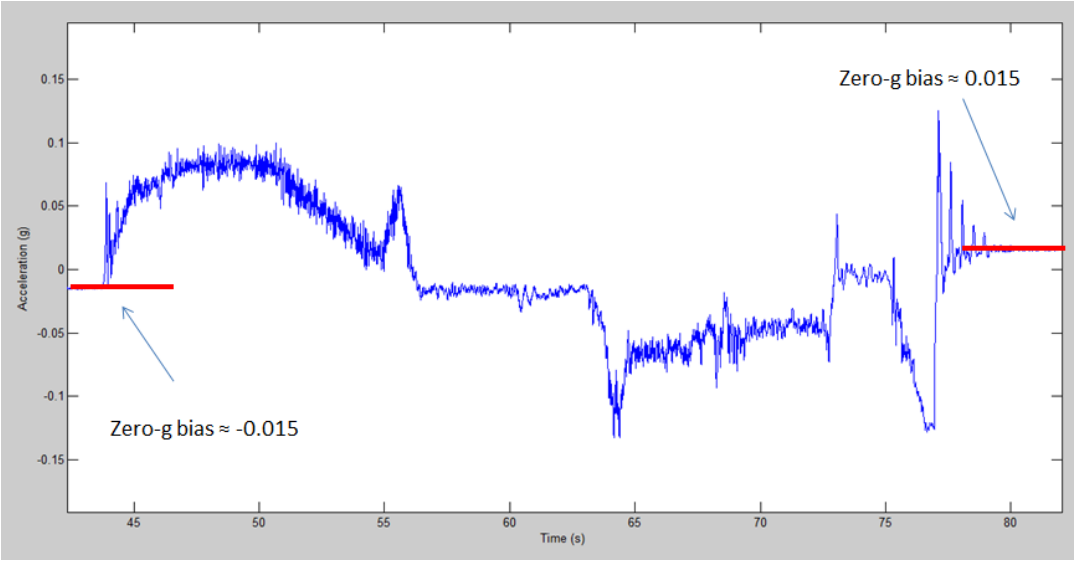

FIGURE 4.1: A step motion showing two different biases at the start and end of motion

high-end IMUs manage to deduce linear acceleration with good accuracy, the efforts in this section of the thesis were to determine how well low-cost accelerometers could do this as a single sensor, which simplifies the hardware and the computational algorithms while reducing the cost required for a navigation system.

A variety of methods were used to remove the gravity bias and they are listed below. They will be further described in the remainder of this section.

- Low Pass Filtering
- Zero Velocity Detection
- Bias Interpolation
- Optimal Bias Algorithm
- Delta Mounted Sensors

Some of the above methods are not possible to be implemented in real-time. These would not be beneficial in the railway environment, especially as safety is a critical requirement. However, they were explored to determine if, given that the bias was nearly perfectly known, these low-cost accelerometers could be successfully used alone in displacement estimation.

4.1 Low Pass Filtering

Filtering the high frequency noise is a strategy that was implemented in all of the methods. It was determined through trials that the signal due to motion resides at frequencies less than approximately 15 Hz, so an FIR low-pass filter of order 60 was

designed that could be used in real-time to eliminate unwanted mechanical and electrical noise. The magnitude response of this filter is shown in Figure 4.2.

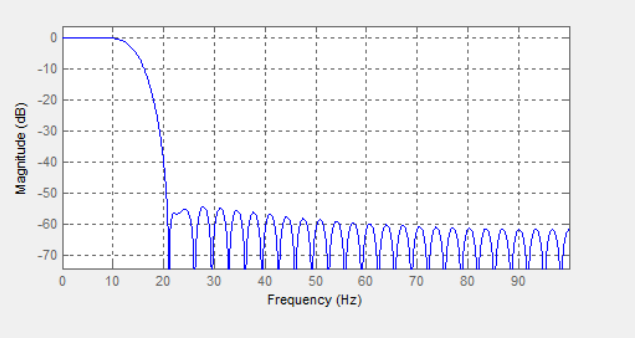

FIGURE 4.2: Magnitude response of the low-pass FIR filter with 15 Hz cut-off frequency and order 60

4.2 Zero Velocity Detection

The biggest problem, based off issues with the simple algorithms explored in the previous chapter, is that slight tilts of the devices cause an obvious offset to the zero-g bias of the sensors since a component of the gravity vector appears on our sensing axis. Therefore the challenge is to attempt to determine the zero-g bias. It is simple to determine the zero-g bias when the sensors are not moving. If it is possible to know that there is no actual motion, then the sensor output is the zero-g bias at that moment. However, the only way to know that the sensors are not moving is to subtract the zero-g bias from the output and the result is zero. This is an inherent problem: you need to know the zero-g bias in order to know you are not moving in order to know that the sensor output is the zero-g bias!

In the railway application being studied, there may be other ways of determining when the train is not moving. From the tests that were done, it was observed that during motion, the sensor outputs were significantly noisier due to vibrations than during periods of no motion. This is demonstrated in Figure 4.3.

As can be seen within the black boxes, the standard deviation of the output on all three axes is significantly lower. These black boxes are during periods of no motion. However, the algorithm must be well tuned or false-positives for no motion may be made. One such false positive is shown in the red box. Here the standard deviation is also low, however it is known that the train was moving here, at a slow but near constant speed.

This observation suggested that it may be possible to determine when the train was stopped by analysing the deviation in the signal from its mean. Utilizing this strategy,

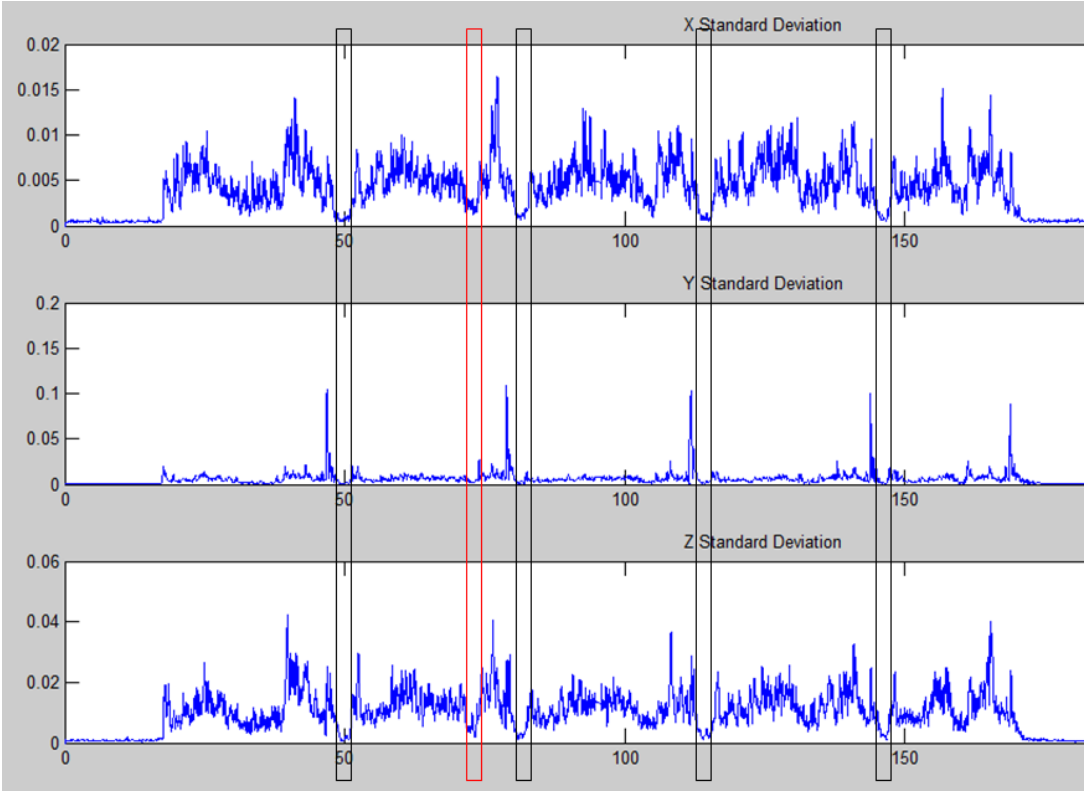

FIGURE 4.3: Standard deviation in a window of accelerometer outputs - the black boxes show the periods where the train was stopped while the red box shows a period of low acceleration where the train was moving slowly but at constant speed

sensors with three-axes have a significant advantage because all three axes can be analysed for motion vibrations to assist in determining if the train is really moving or not. The algorithm that was found to succeed in determining when the train was in motion checks the standard deviation of the signal in a small window near the current time. If the standard deviation on all three axes is below a certain threshold, it is assumed that the train is stopped and the bias is determined to be the sensor output. If the standard deviation on one axis is above the threshold, it is assumed the train is moving. In addition, if the train is assumed to be stopped, integration is not necessary, which eliminates integration drift due to random error for the period of no motion.

This approach of analysing the standard deviation was used successfully for a step run, demonstrated in Figure 4.4. The periods of no motion are after deceleration and the algorithm successfully detects them. However, there is one short false positive at approximately the 70 second mark.

An alternative approach to analysing the standard deviation of the three axes takes the total magnitude of the acceleration and analyses the standard deviation of this. The total magnitude of the acceleration is calculated using Equation (4.1).

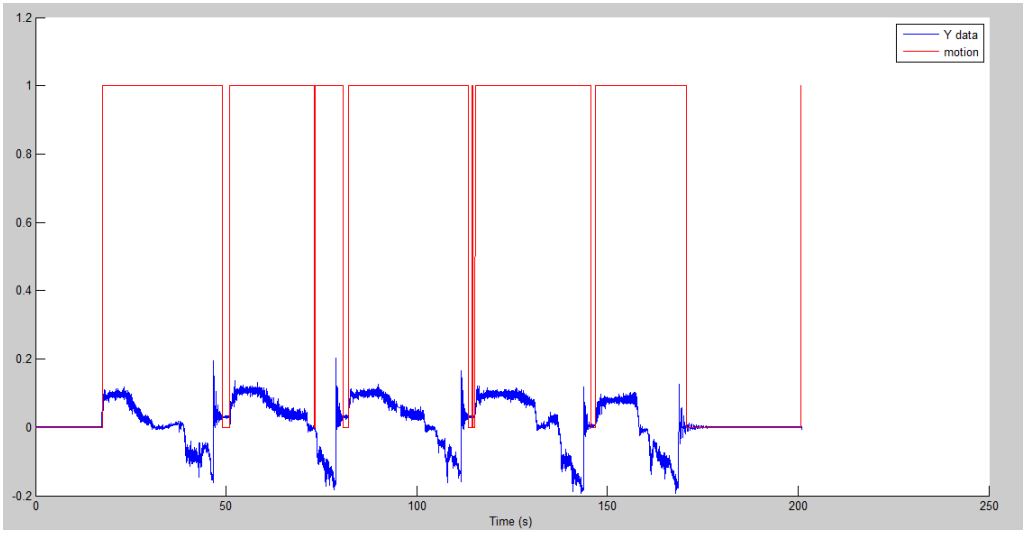

FIGURE 4.4: Standard deviation algorithm for no motion - the red line shows 1 if the algorithm determines there is motion and 0 if it determines there is no motion

$$a_{tot} = \sqrt{a_x^2 + a_y^2 + a_z^2} \tag{4.1}$$

The advantage of doing this is that it is known the signal will centre about 1 g. Subtracting 1 g from the magnitude centre the data about 0 g, which allows the algorithm to also use the absolute value of the acceleration to determine if there is no motion. The total acceleration standard deviation is shown in Figure 4.5.

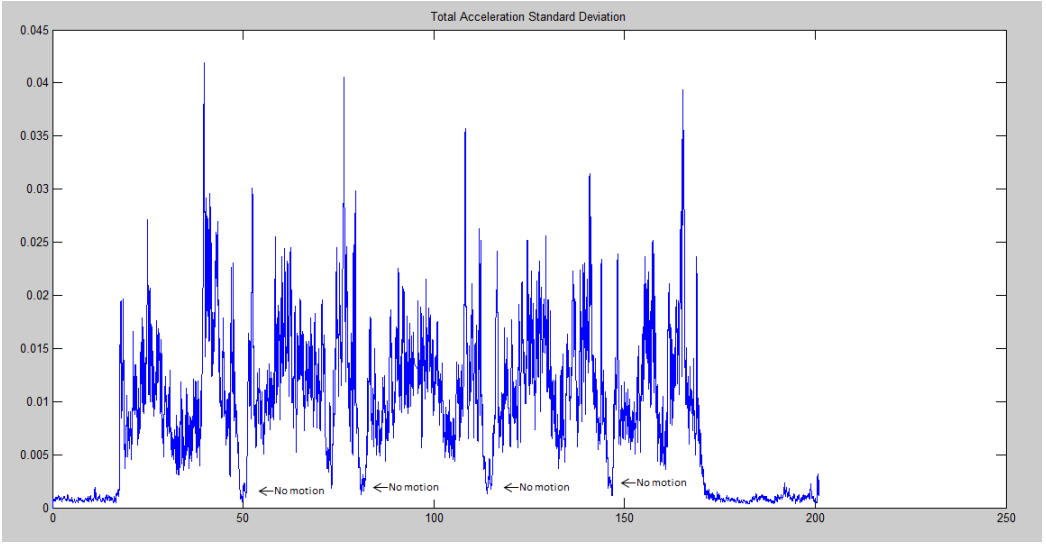

FIGURE 4.5: Standard deviation of the total acceleration

Adding the condition that the absolute value of the total acceleration must be below a threshold helps to remove the false positives that can occur by only looking at the standard deviation of the signal. The results of this algorithm's performance are shown in Figure 4.6.

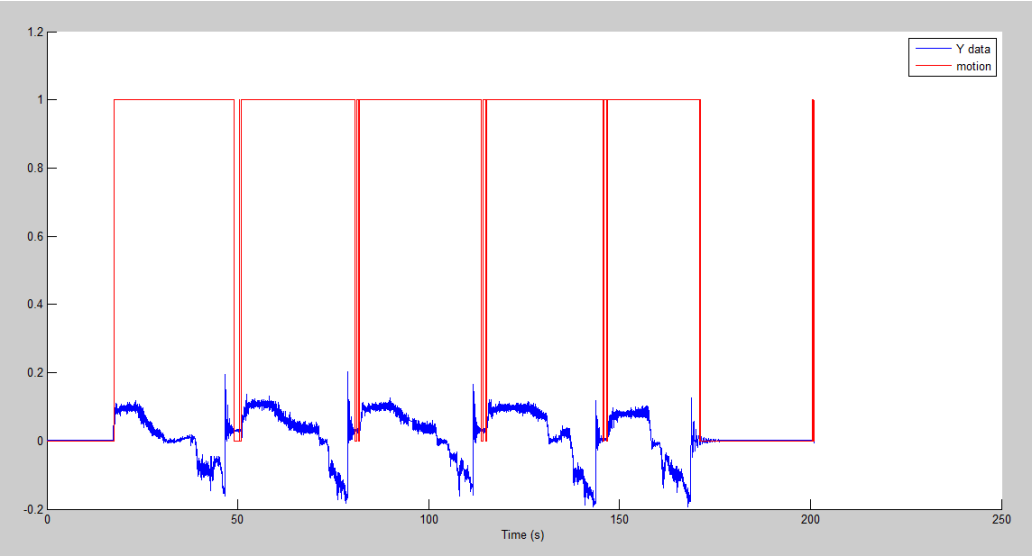

FIGURE 4.6: Standard deviation algorithm using total acceleration - no false positives are detected

This algorithm works well for determining when there is no motion in the railway environment. It uses two parameters, the standard deviation threshold in a window and the absolute value of the total acceleration threshold, to determine when there is no motion. These two values must be tuned for the sensors and the environment at hand. Further, the algorithm works for three-axes sensors as it makes use of the off-axis vibrations that are present. For one-axis sensors, it is not as robust.

4.3 Bias Interpolation

The bias interpolation method is a post-processing algorithm that would not work in real time. The premise behind this idea uses zero velocity detection to determine the bias during periods of no motion. However, during periods of motion, the bias is no longer known and has to be estimated somehow. The bias interpolation algorithm assumes that the bias changes approximately linearly from two points of no motion, demonstrated in Figure 4.7.

This direct linear interpolation method was evaluated, however with further testing, a slightly different interpolation function was found to have better performance.This function assumes that the second bias point is reached approximately 40% of the way during motion. It therefore interpolates from the first bias to the second bias for the first 40% of motion, then keeps the second bias until the end of motion. This is visually depicted in Figure 4.8.

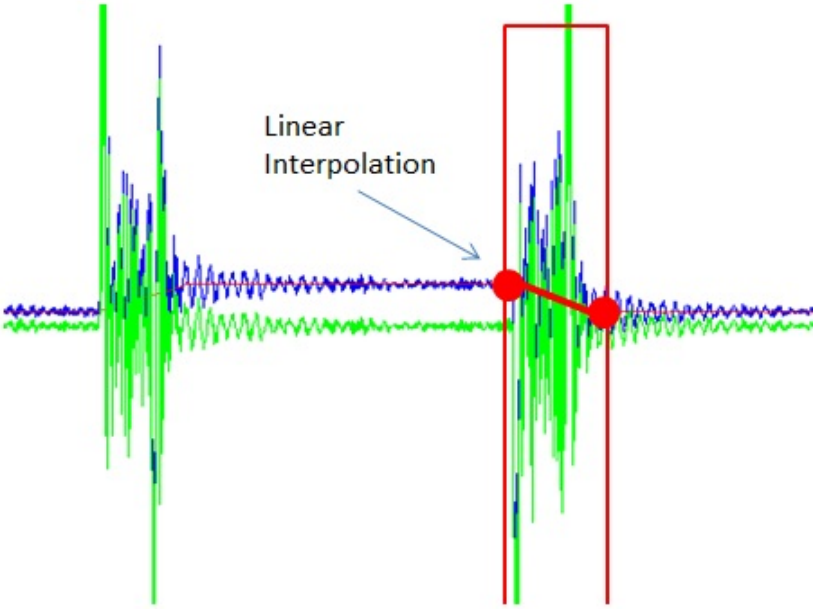

FIGURE 4.7: Bias estimation using linear interpolation between points of no motion

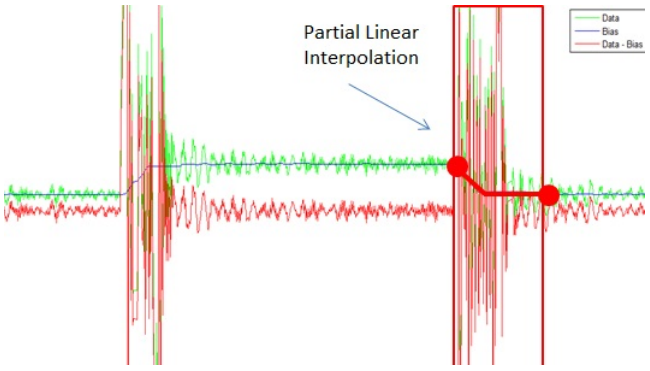

FIGURE 4.8: Bias estimation using partial linear interpolation between points of no motion

The results obtained using this partial interpolation on the evaluation platform were considered accurate. As can be seen from Figure 4.9 to Figure 4.11, four different runs of horizontal motion were performed, with displacement estimations being accurate to within 2 cm over 96 cm of motion.

As the results show, the accelerations, velocities, and displacements of the accelerometer closely match those of the GoPro camera, which is measuring ground truth. This indicates that for the evaluation platform, the bias interpolation is giving accurate estimates of the bias between periods of no motion.

This horizontal test uses longer motions with long rest times, which help the bias estimation perform interpolation. Another test, the step test, goes through shorter motions

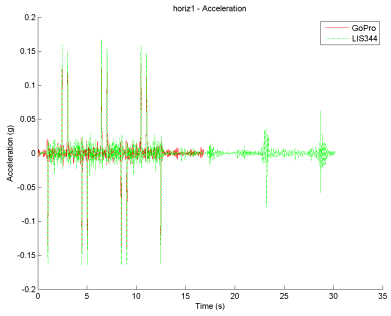

(A) Acceleration for horizontal run 1

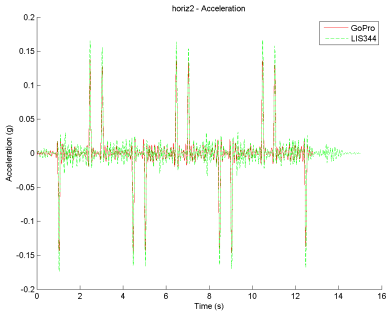

(B) Acceleration for horizontal run 2

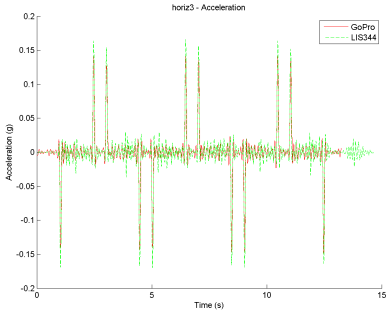

(C) Acceleration for horizontal run 3

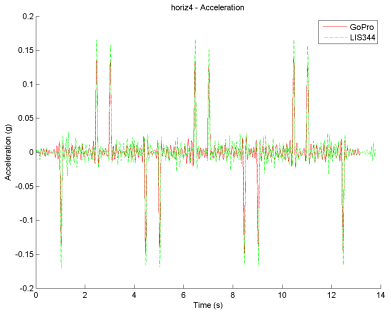

(D) Acceleration for horizontal run 4

FIGURE 4.9: Accelerations during horizontal runs using interpolated bias

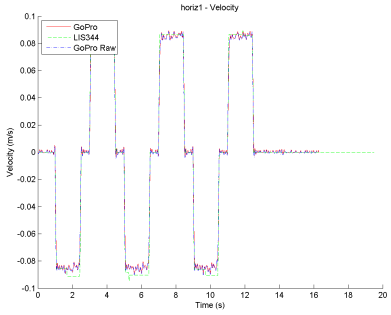

(A) Velocity for horizontal run 1

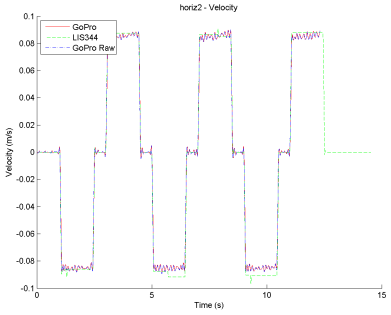

(B) Velocity for horizontal run 2

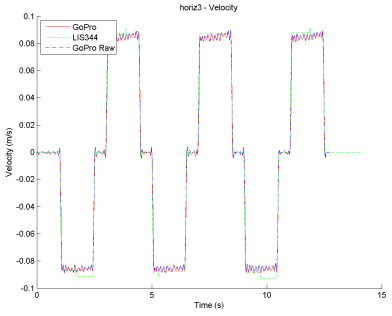

(C) Velocity for horizontal run 3

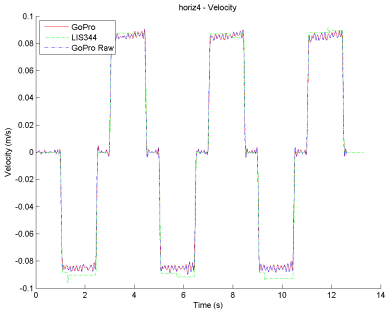

(D) Velocity for horizontal run 4

FIGURE 4.10: Velocities during horizontal runs using interpolated bias

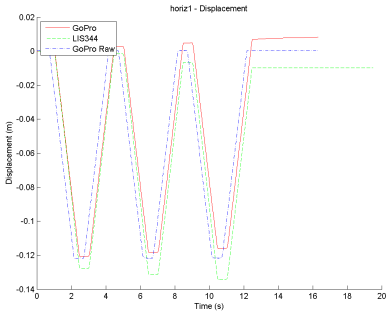

(A) Displacement for horizontal run 1

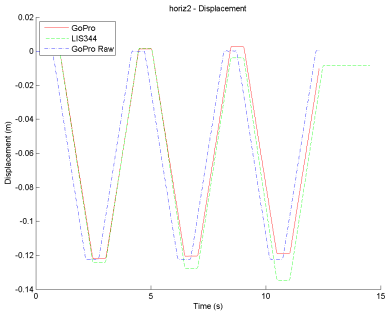

(B) Displacement for horizontal run 2

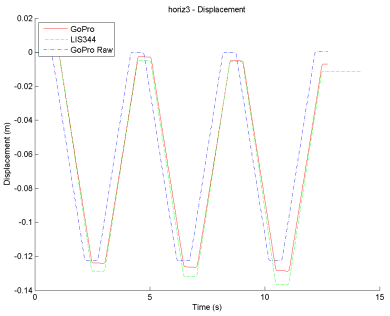

(C) Displacement for horizontal run 3

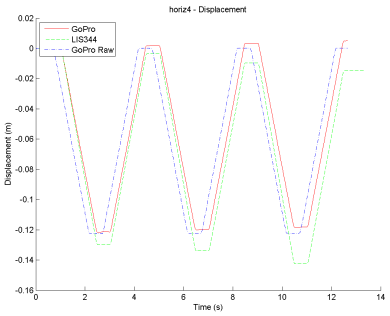

(D) Displacement for horizontal run 4

FIGURE 4.11: Displacements during horizontal runs using interpolated bias

and shorter rest times, which make the bias interpolation more difficult. The results from three step tests are seen in Figure 4.12 to Figure 4.14.

From the results shown, the sensors using the interpolation algorithm are able to estimate displacements to within a few centimetres of error after 40 centimetres of motion. This accuracy scaled to the railway environment would be acceptable, however the main issue remains that the bias interpolation is a post-processing algorithm and does not give this accuracy in real time.

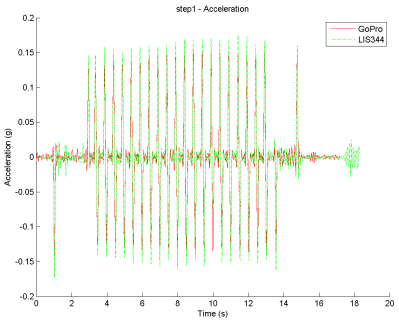

(A) Acceleration for step run 1

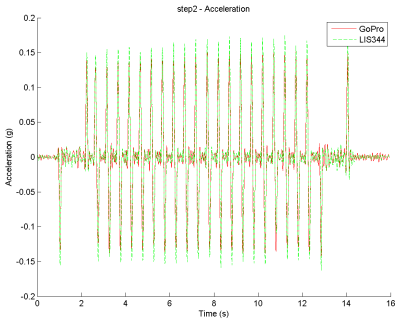

(B) Acceleration for step run 2

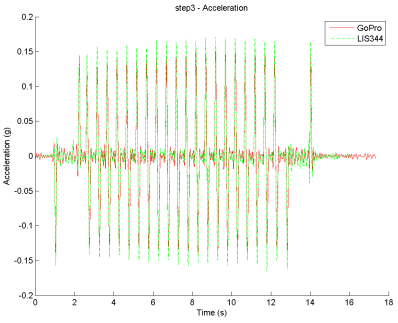

(C) Acceleration for step run 3

FIGURE 4.12: Accelerations during step runs using interpolated bias

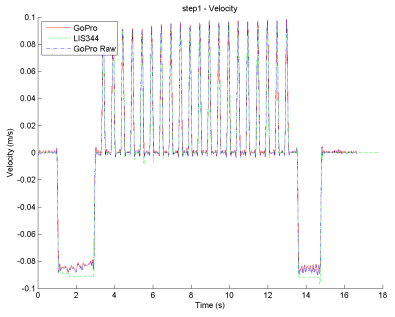

(A) Velocity for step run 1

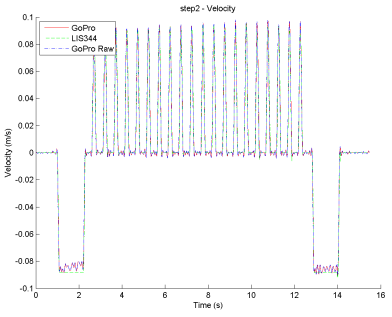

(B) Velocity for step run 2

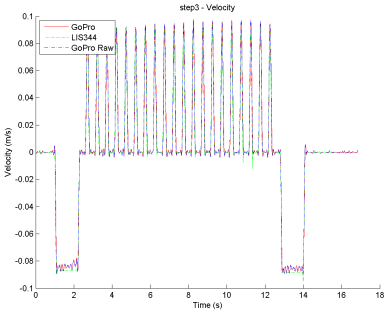

(C) Velocity for step run 3

FIGURE 4.13: Velocities during step runs using interpolated bias

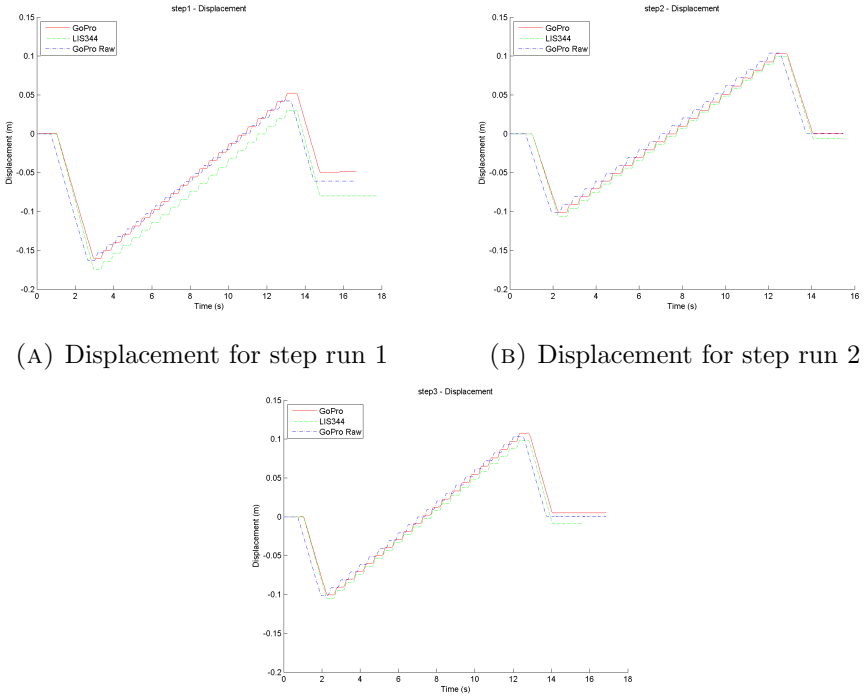

(A) Displacement for step run 1

(B) Displacement for step run 2

(C) Displacement for step run 3

FIGURE 4.14: Displacements during step runs using interpolated bias

4.4 Optimal Bias Algorithm

Due to the fact that bias interpolation seemed to show some error, it was desired to know approximately what the bias really is during periods of motion. If points of zero velocity are known, then when acceleration is integrated once between two points of zero velocity, the resultant final velocity must be equal to zero. This is more clearly depicted in Figure 4.15.

From the image, it can be seen that at approximately the 43 second mark, the train started to move. At about the 80 second mark, the train has finished its deceleration and is stopped. We know Equation (4.2) must hold.

$$\int_{t=43}^{t=80} [a(t) - B]dt = 0 \tag{4.2}$$

In this equation, $a(t)$ is the sensor output and B is the unknown sensor zero-g bias, assumed constant throughout motion. An algorithm was developed based off gradient descent optimization tools within the Matlab Optimization Toolbox [9]. The *fminunc* function is used to minimize the error of a function by varying some parameter. In order to use this algorithm for this application, the error term was integrated velocity while

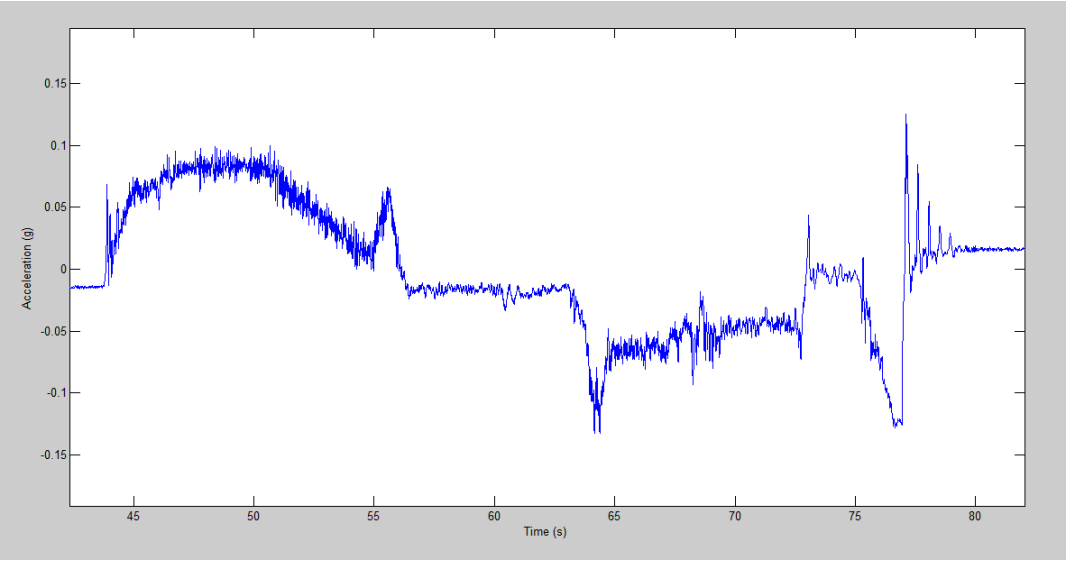

FIGURE 4.15: The acceleration output of one step motion lasting approximately 40 seconds

the parameter to be varied was the bias, in this case assumed to be constant throughout motion. Using this algorithm, a constant bias can be calculated for the period of motion, which if used during that motion, will result in a zero final integrated velocity. This algorithm eliminates the undesirable integration drift during periods of zero motion. However, this algorithm is too complex to be used in real-time. The algorithm applied to the motion in Figure 4.15 gives the velocity profile in Figure 4.16.

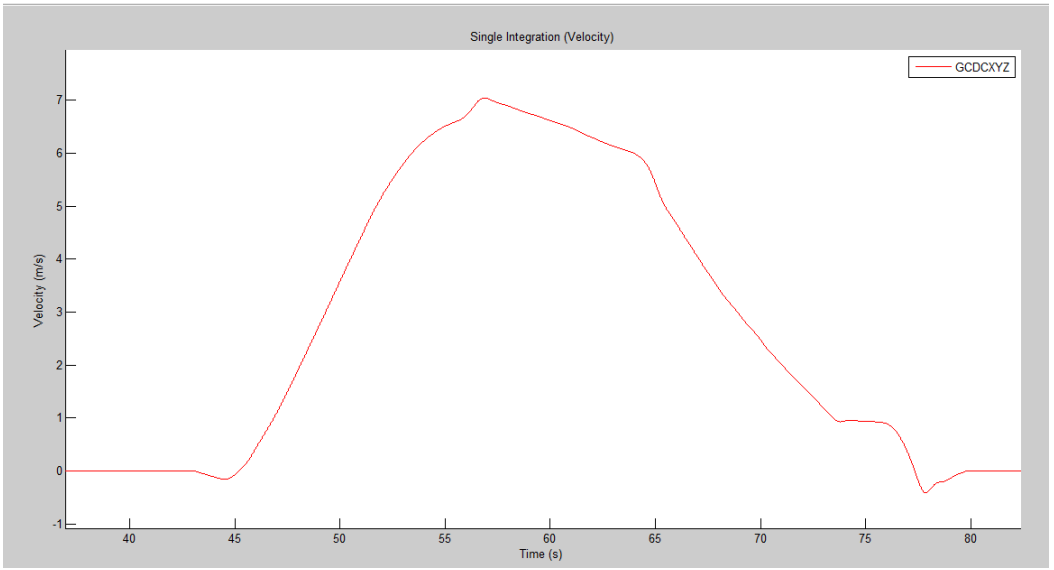

FIGURE 4.16: The velocity during one step motion using bias computed from the optimal algorithm

The bias that was computed by the algorithms successfully forces the velocity profile to begin and end with zero velocity. This eliminates the integration drift that occurs when non-zero velocity is computed from the first integration and gives a displacement profile

that approximately matches the actual motion during testing, as seen in Figure 4.17 where the actual displacement in the test was 150 m.

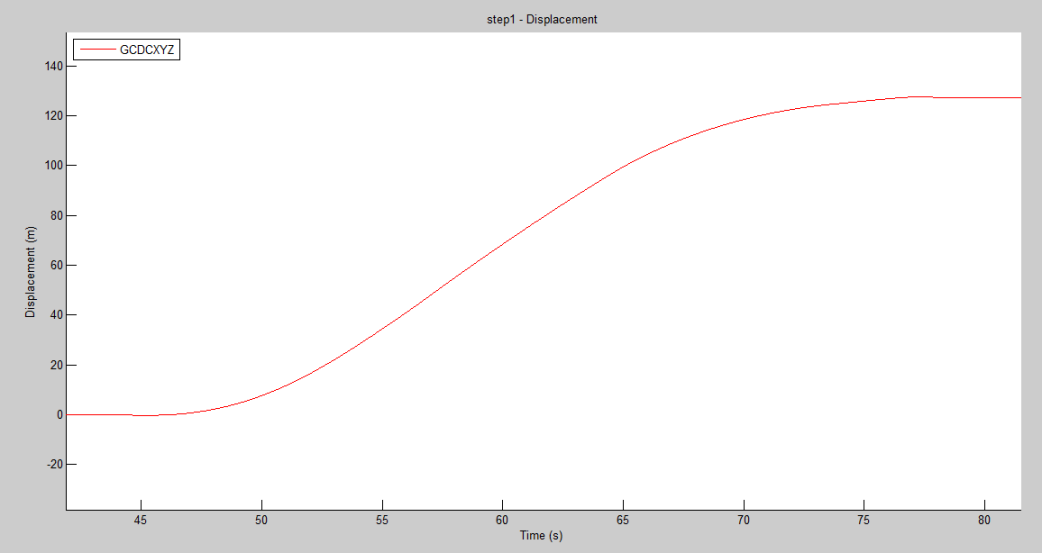

FIGURE 4.17: The displacement during one step motion using bias computed from the optimal algorithm

The biggest benefit of this algorithm was to observe what the bias actually approximately looked like during periods of motion. It was initially assumed that the bias would be approximately linearly interpolated between periods of no motion, however the tests done using the optimal bias algorithm suggested that during motion, the vehicle's suspension system and braking mechanics tilt the train significantly, which gives a different bias immediately when the train begins to move.

The optimal bias algorithm was applied to a number of the tests ran on the TTC Yonge-Sheppard subway line. The runs that were tested were the step test, the step-and-return test, the shuttle test, and the full run of the line. The results of these tests are shown in Figure 4.18 through Figure 4.25, where the displacement estimations are accurate to below 10% error over long distances.

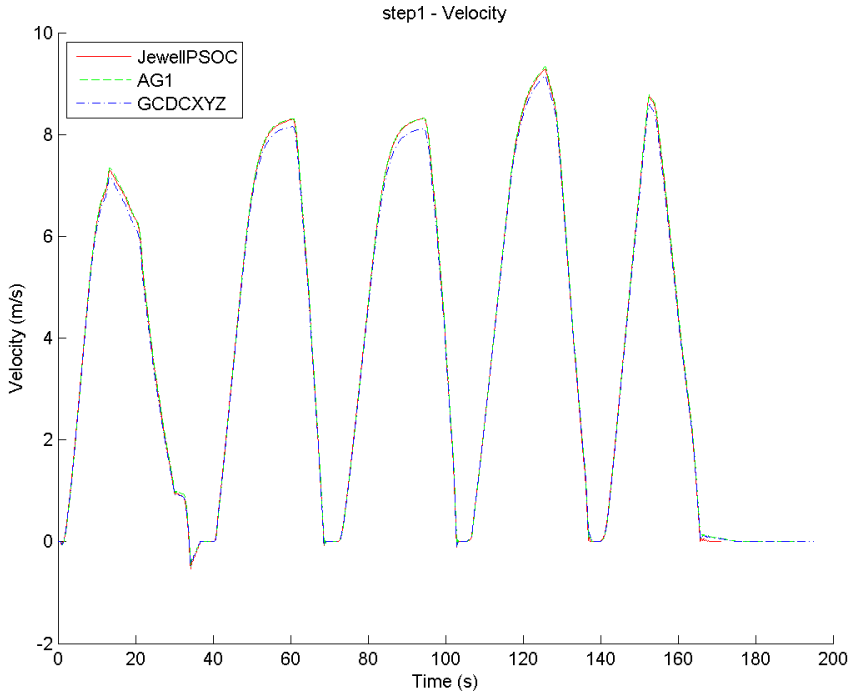

(A) Single integration after computed optimal bias

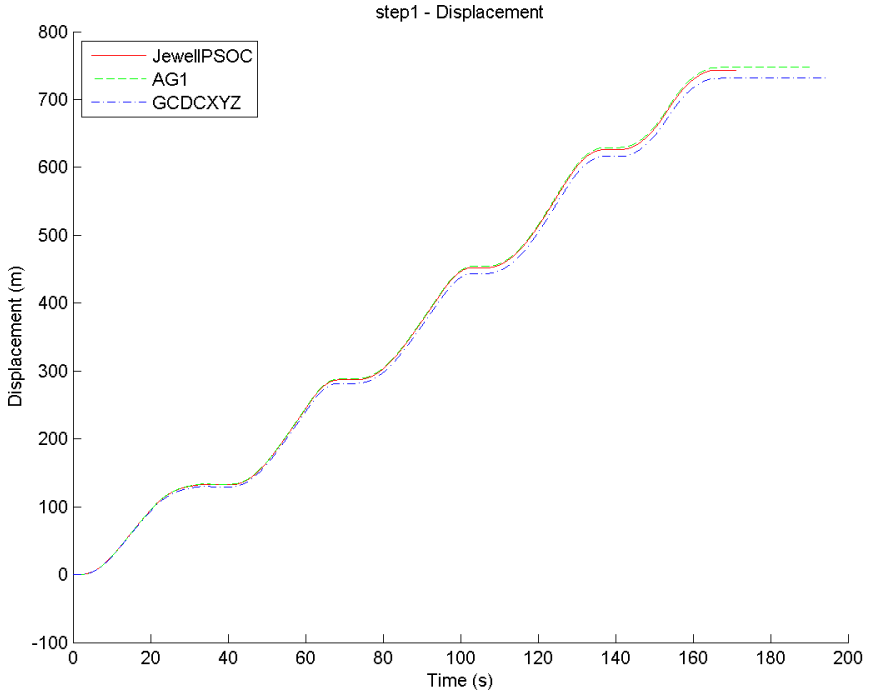

(B) Double integration after computed optimal bias

FIGURE 4.18: Results of double integration for step motion run 1 using optimal bias, actual displacement was approximately 760 m

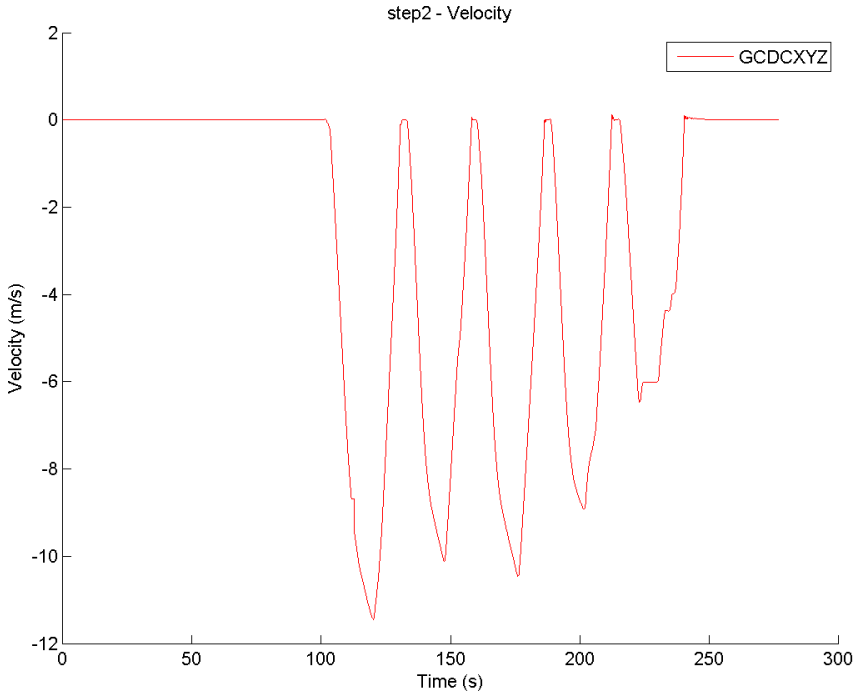

(A) Single integration after computed optimal bias

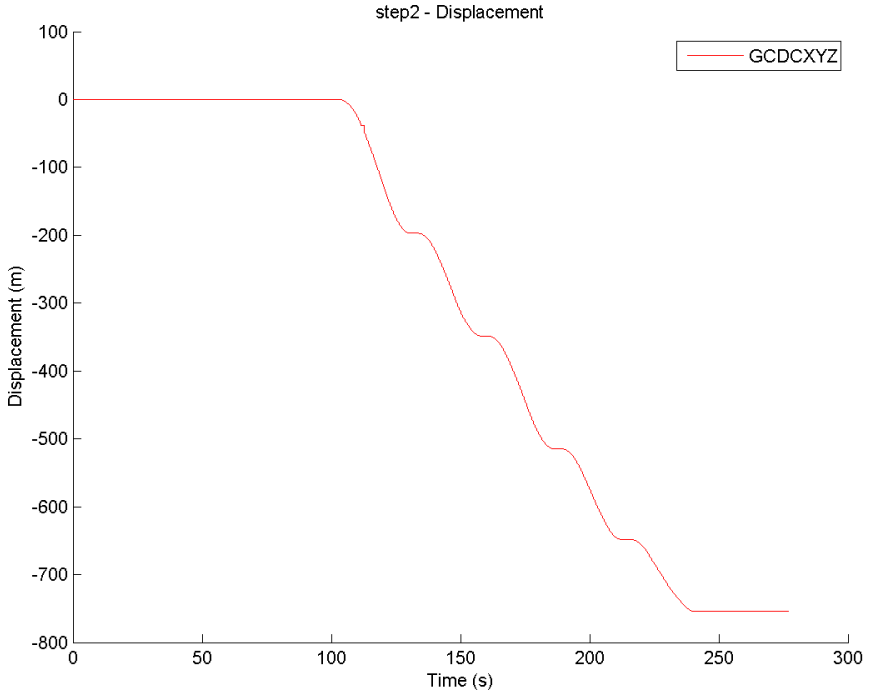

(B) Double integration after computed optimal bias

FIGURE 4.19: Results of double integration for step motion run 2 using optimal bias, actual displacement was approximately 760 m

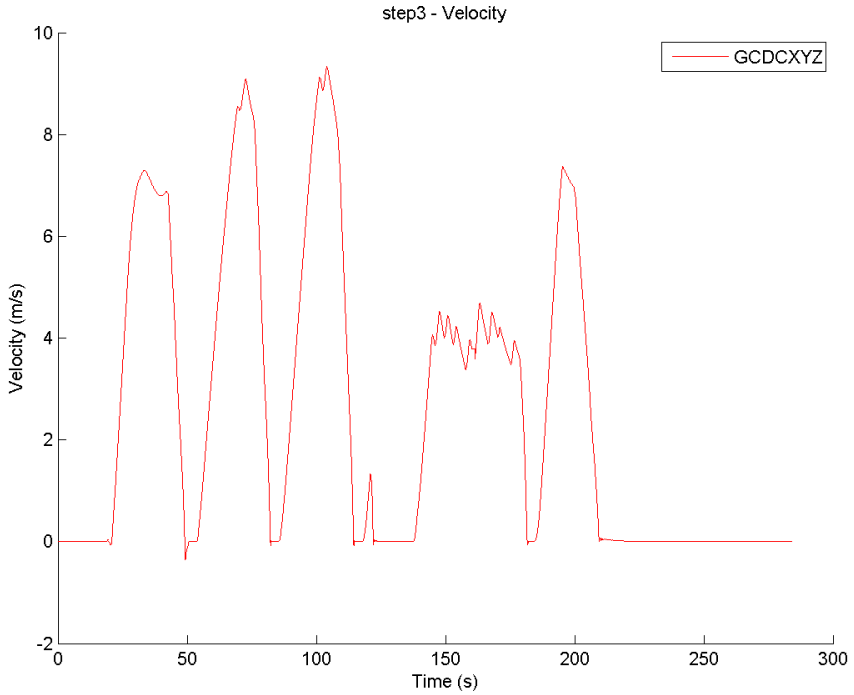

(A) Single integration after computed optimal bias

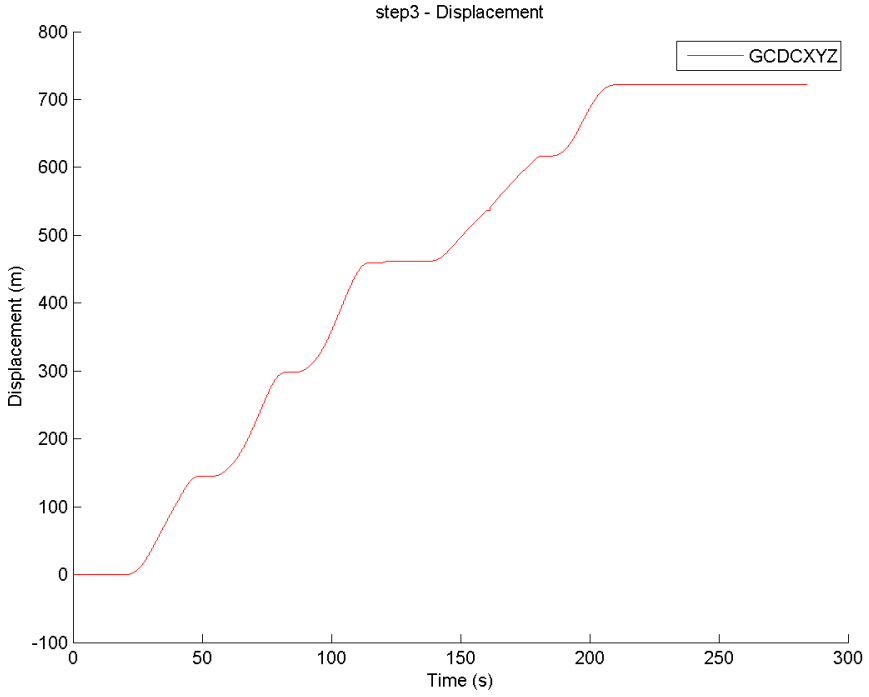

(B) Double integration after computed optimal bias

FIGURE 4.20: Results of double integration for step motion run 3 using optimal bias, actual displacement was approximately 760 m

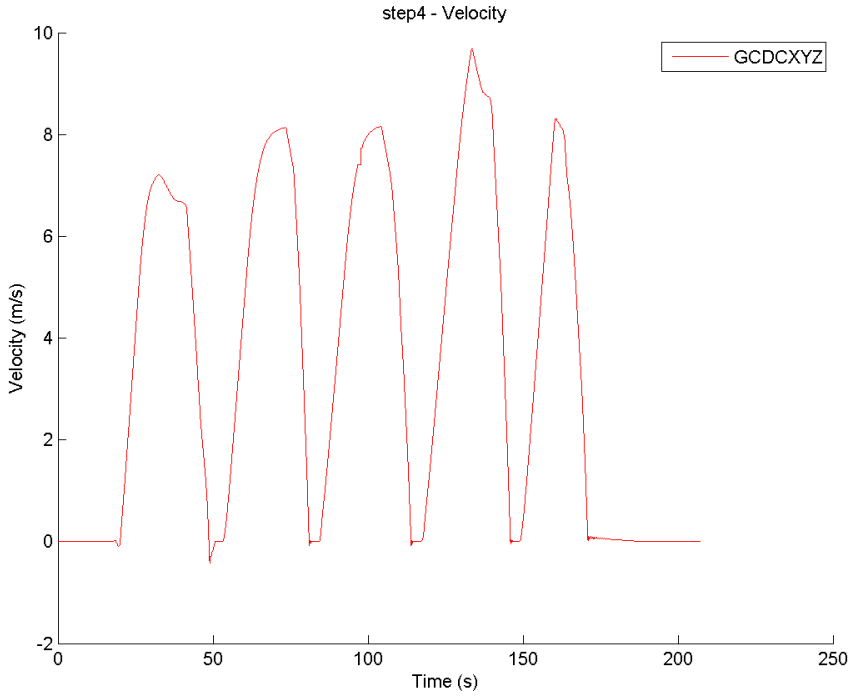

(A) Single integration after computed optimal bias

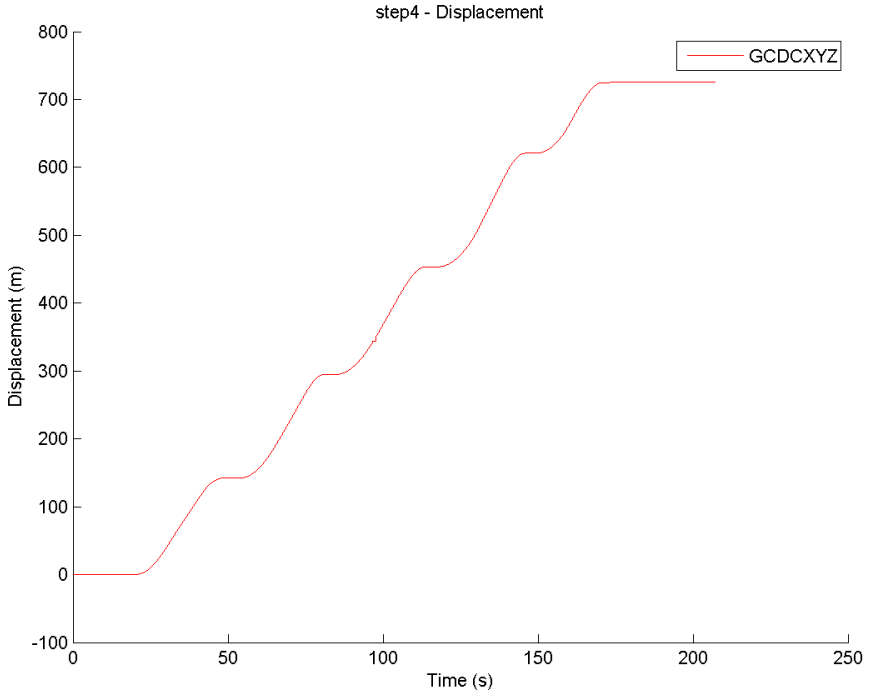

(B) Double integration after computed optimal bias

FIGURE 4.21: Results of double integration for step motion run 4 using optimal bias, actual displacement was approximately 760 m

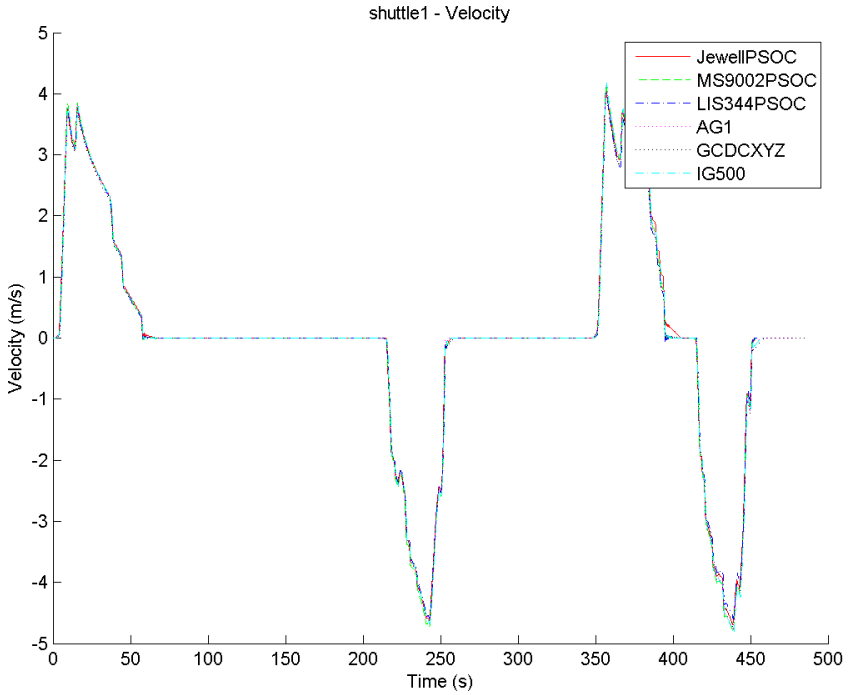

(A) Single integration after computed optimal bias

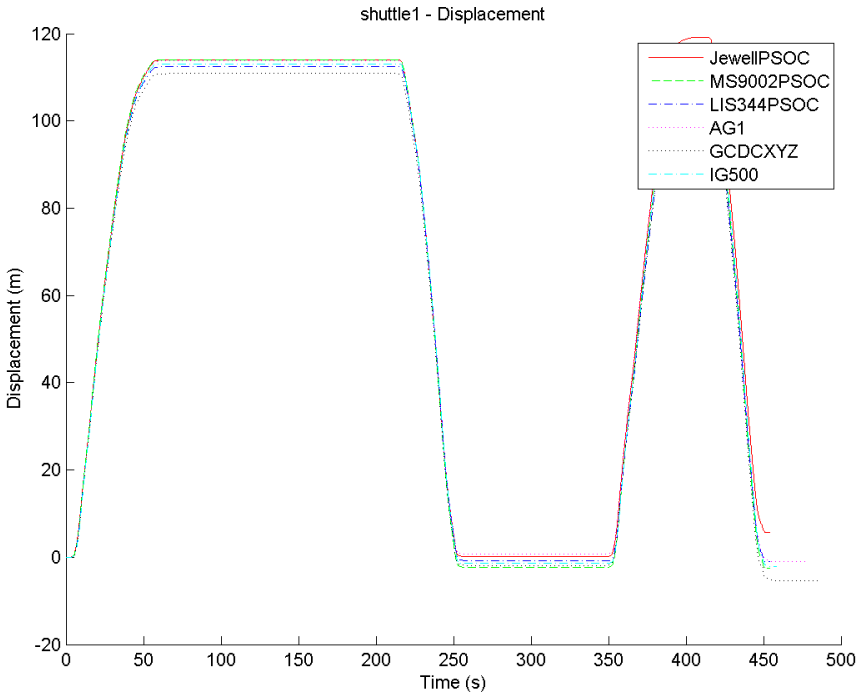

(B) Double integration after computed optimal bias

FIGURE 4.22: Results of double integration for shuttle motion run using optimal bias, actual displacement was approximately 110 m forward then return to the original position

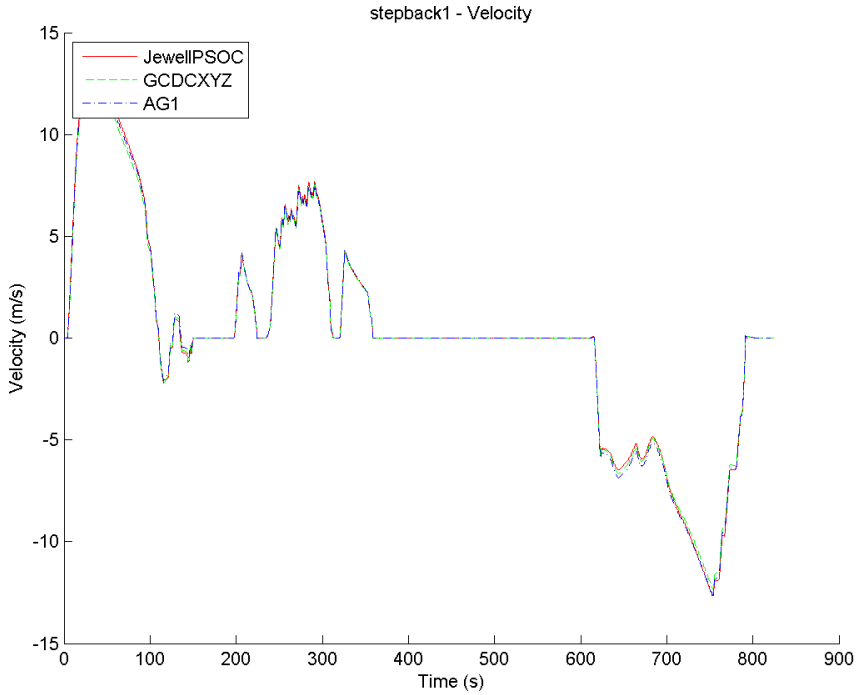

(A) Single integration after computed optimal bias

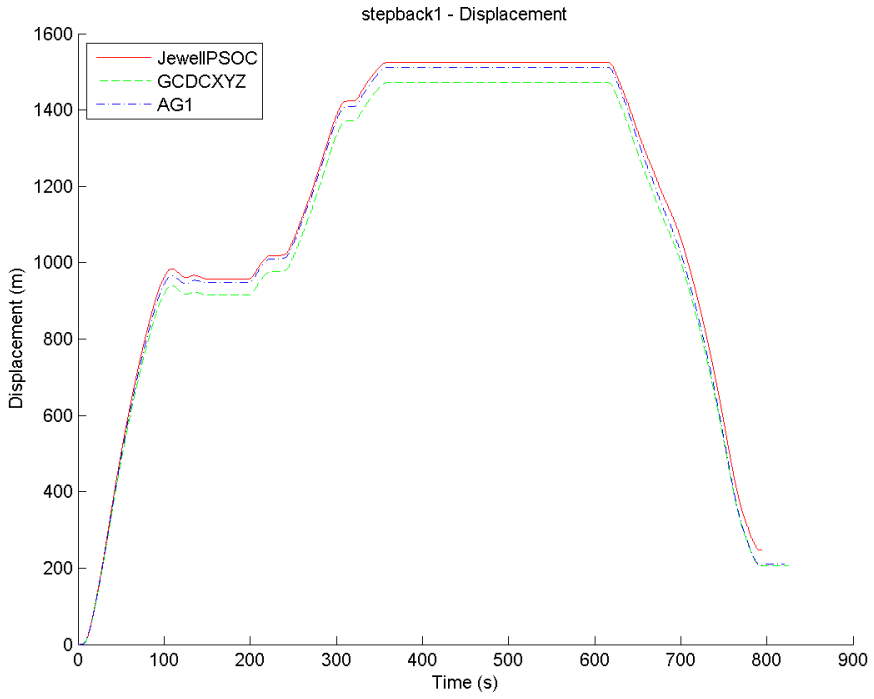

(B) Double integration after computed optimal bias

FIGURE 4.23: Results of double integration for step-and-return motion run 1 using optimal bias, actual displacement approximately 2000 m forward then 2000 m back

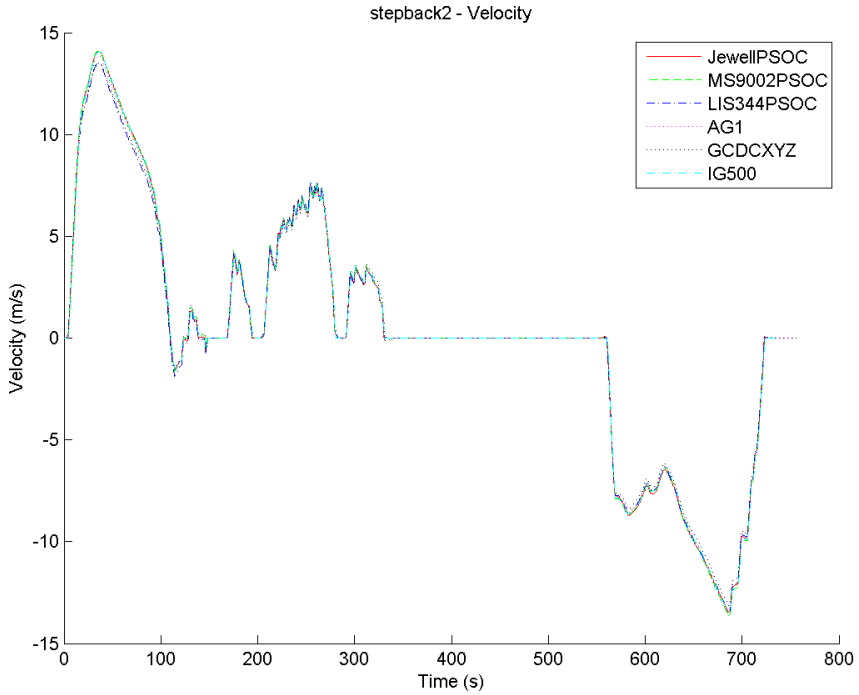

(A) Single integration after computed optimal bias

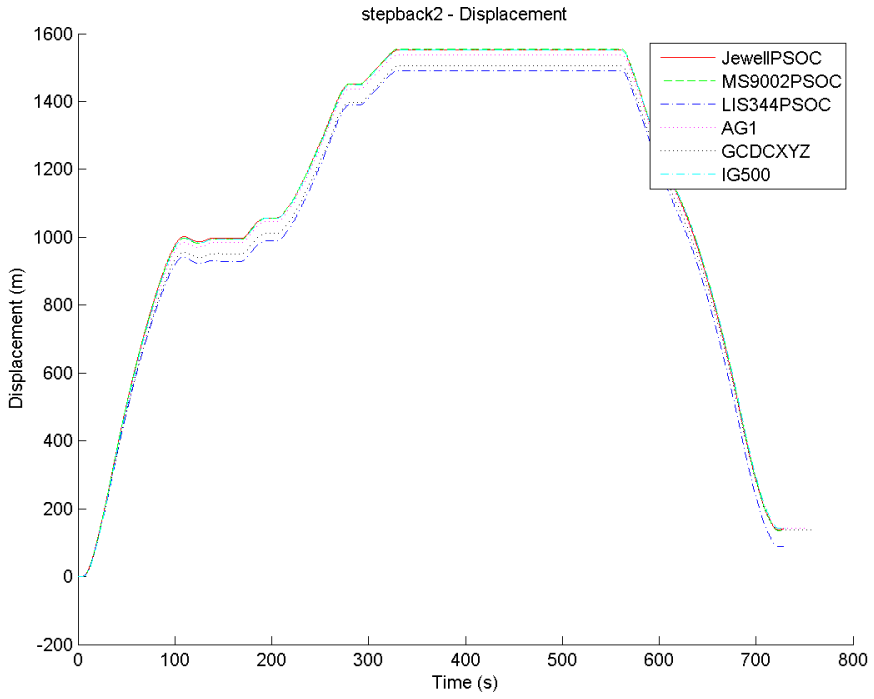

(B) Double integration after computed optimal bias

FIGURE 4.24: Results of double integration for step-and-return motion run 1 using optimal bias, actual displacement approximately 2000 m forward then 2000 m back

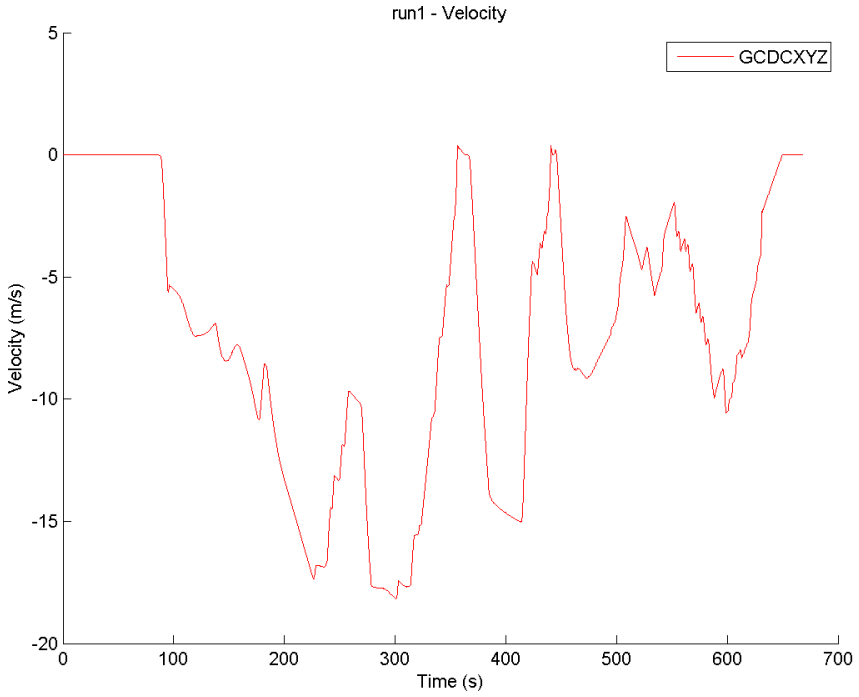

(A) Single integration after computed optimal bias

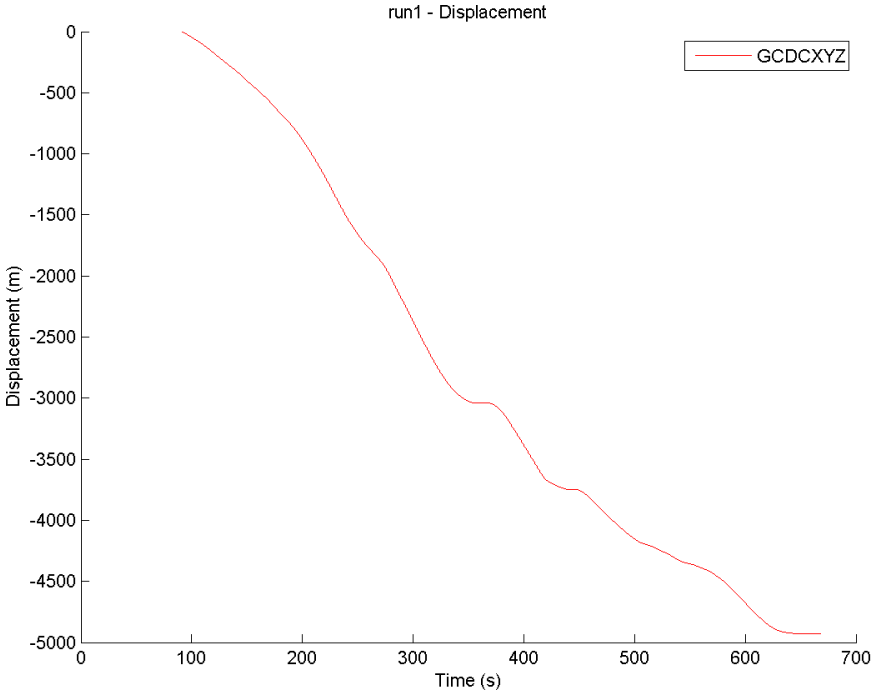

(B) Double integration after computed optimal bias

FIGURE 4.25: Results of double integration for full subway line run using optimal bias, actual displacement was approximately 5500 m

It is possible that, while the train comes to a stop, the bias can be computed to update the current displacement with a more accurate estimate. The main problem with the optimal bias algorithm is that it takes a long time to compute using the gradient descent algorithm. However, after revisiting the algorithm, it was found that a more simple approach can be used to deduce the required bias during motion. Observing the equation for the integration, we know that a constant bias error integrated gives the velocity error as follows

$$\int_{t_1}^{t_2} a(t)dt = v_\epsilon(t) = B_\epsilon[t_2 - t_1] \tag{4.3}$$

where B_ϵ is the bias error. Since we know the integrated velocity should be equal to zero when t_1 and t_2 represent consecutive times of zero velocity, any nonzero velocity must be due to the constant bias error, therefore we can calculate the bias error as

$$B_\epsilon = \frac{\int_{t_1}^{t_2} a(t)dt}{t_2 - t_1} \tag{4.4}$$

Further, since we know that the displacement error due to a constant bias error is

$$x_\epsilon(t) = B_\epsilon(t_2 - t_1)^2 \tag{4.5}$$

we can calculate an updated displacement by

$$x_{new} = x_{old} - x_\epsilon = x_{old} - B_\epsilon(t_2 - t_1)^2 \tag{4.6}$$

instead of integrating again with the new bias, which would be more complex to process.

It is shown here that the required bias can be computed with one division and a more accurate displacement estimation can be computed in a similarly simple manner. This means that the algorithm can update the displacement immediately when it is known that there is no motion, while using a previous bias during motion.

4.5 Delta-Mounted Sensors

The concept of delta-mounted sensors is named this way because the sensors are mounted so that two axes are 45° to the direction of motion, which forms a triangle or delta shape, as seen in Figure 4.26. The motivation behind this method is that applied accelerations would always be equal on both axes while tilts in the sensors would provide a differential on the output of the two axes. The idea is that a set of equations could be used to calculated both the sensor's tilt and the motion being applied to the sensor from these two axes.

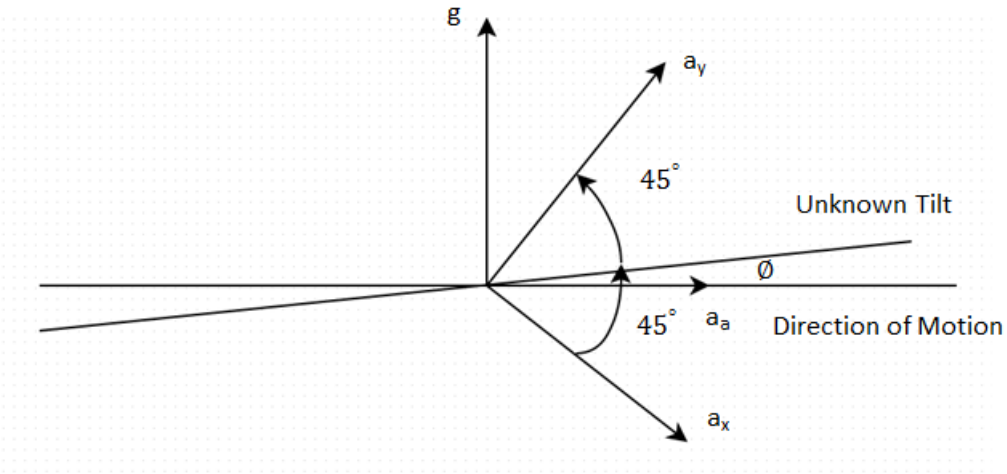

FIGURE 4.26: Delta-mounted sensors with labelled axes

The derivation of equation Equation (4.7) for this configuration is found in Appendix C. In the equations that follow, a_x and a_y are respectfully the x-axis and y-axis sensor readings, g is the acceleration due to gravity, a_a is the applied acceleration from the motion platform or subway train, and ϕ is the unknown tilt angle that is being determined. The equations derived in Appendix C provide us with a quadratic equation to determine the tilt angle. The quadratic formula gives two solutions to the equation.

$$\phi_{1,2} = \frac{-(2a_x + 2a_y) \pm \sqrt{(2a_x + 2a_y)^2 - 4(a_x - a_y)(2a_y - 2a_x - \frac{4g}{\sqrt{2}})}}{2(a_x - a_y)} \tag{4.7}$$

Examining the quadratic formula applied to this solution, we know that a real solution exists if $b^2 - 4ac > 0$. To see if this equation can provide real solution, let's consider the simplest case that there is zero tilt ($\phi = 0$). By mounting the sensors at 45° angles, $b = (2a_x + 2a_y) \approx 0$, therefore it is necessary that $4ac < 0$ for a solution to exist. Again, due to the mounting of the sensors, $a = a_x - a_y < 0$, therefore for $4ac < 0$, c must be a positive number. This gives us the the constraint that $2a_y - 2a_x - \frac{4g}{\sqrt{2}} > 0$. Testing

this equation in the railway environment with accelerations less than 0.15 g show that this equation is rarely satisfied. However, this equation was still tested by mounting the AG-1 (ST LIS3LV02DL accelerometer chip) onto the evaluation platform at various tilt angles and moving horizontally, as in the horizontal runs. The results from these experiments are shown in Figure 4.27 and Figure 4.28.

The data in Figure 4.27 shows the acceleration results of the horizontal test performed with the AG-1 mounted at 0°, 5°, and 10°. Examining the periods where there is no motion, the bias level is based on the tilt angle being applied. For example, in the 0° experiment, the y bias is approximately 0.7 and the x-bias is approximately -0.7. These values correspond to $1/\sqrt{2} = 0.71$, because each axis carries an equal component of gravity due to the zero tilt. Taking the magnitude of these values gives 1 g. Correspondingly, at 5°, the y-axis is closer to 0.75, while the x-axis is closer to -0.65 when there is no motion. This is because, due to the tilt, more of the gravity vector appears on the y-axis. A similar explanation holds for the 10° run. Further, examining the accelerations during motion, it can be seen that the change in acceleration is in the same direction for each axis. That is, the first motion makes both axes more positive, followed by a short constant acceleration where the signal is near the bias but noisier, followed by a signal that makes both axes more negative. This was the reason for mounting the sensors in this manner.

Figure 4.28 shows the tilt angles computed using equation Equation (4.7). The computed angles are correct withina small percentage error when the sensors are not in motion, however during motion the $b^2 - 4ac$ term becomes negative, which provides complex solutions to the quadratic equation (the real part of these complex solutions is plotted here). These solutions cannot be used, which implies that mounting the sensors in this delta formation does not provide a benefit because the problem remains that the tilt cannot be deduced when the sensors are in motion.

Other approaches were taken to analyze the deta obtained from the experiments with the sensors mounted in the delta configuration. One approach was to add the signals together, which would cancel the tilt bias and leave us with just the signal. However, this did not prove useful, as there was still a changing bias during the periods of no motion when this was done. To make matters still more difficult, during motion it remains impossible to determine if the tilt is changing, because motion will always add mechanical noise. This mechanical noise means that is not possible to separate if acceleration changes are due to motion or change in tilt.

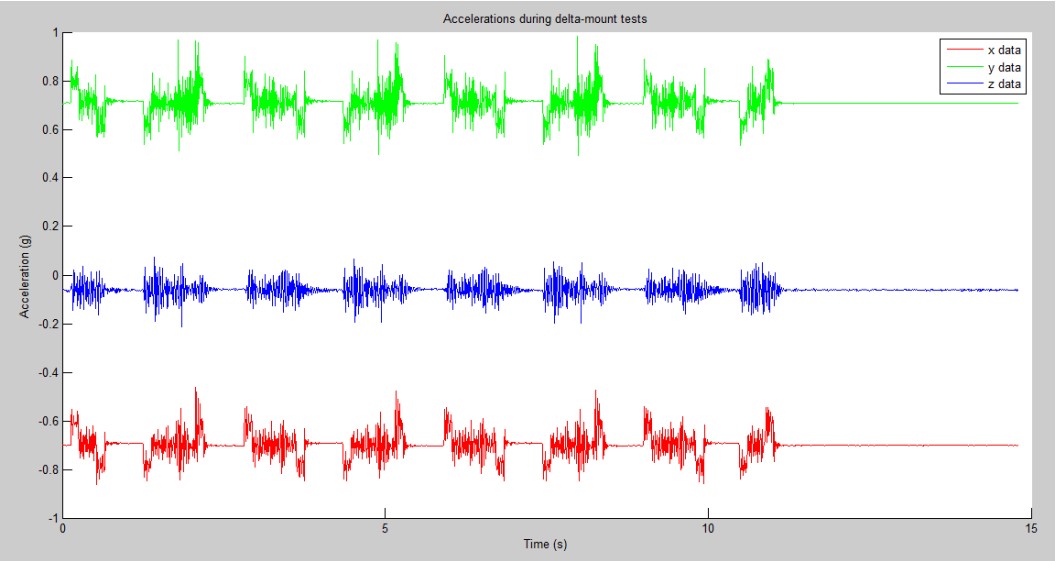

(A) Accelerations for delta run at tilt of 0°

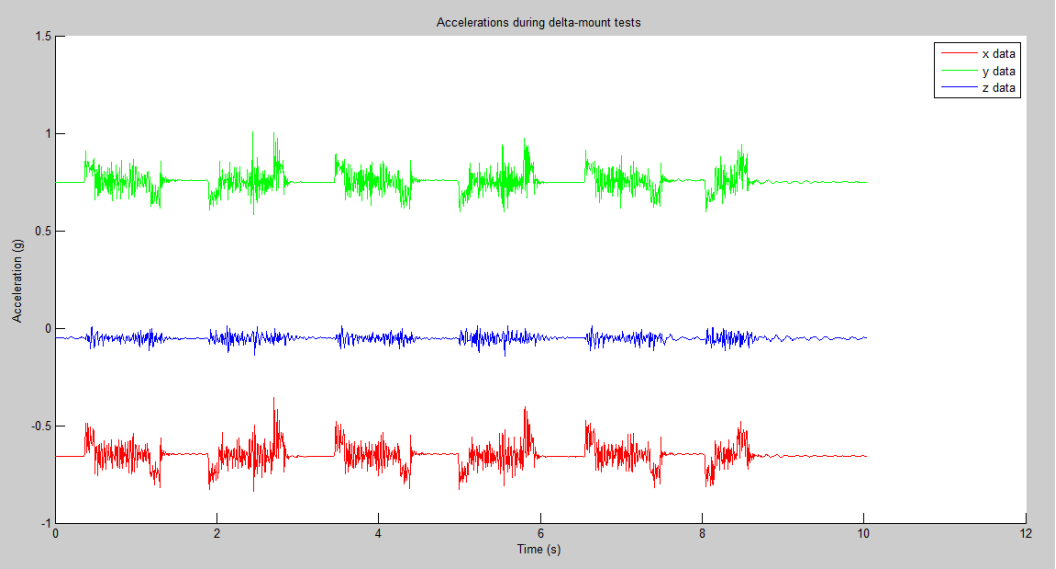

(B) Accelerations for delta run at tilt of 5°

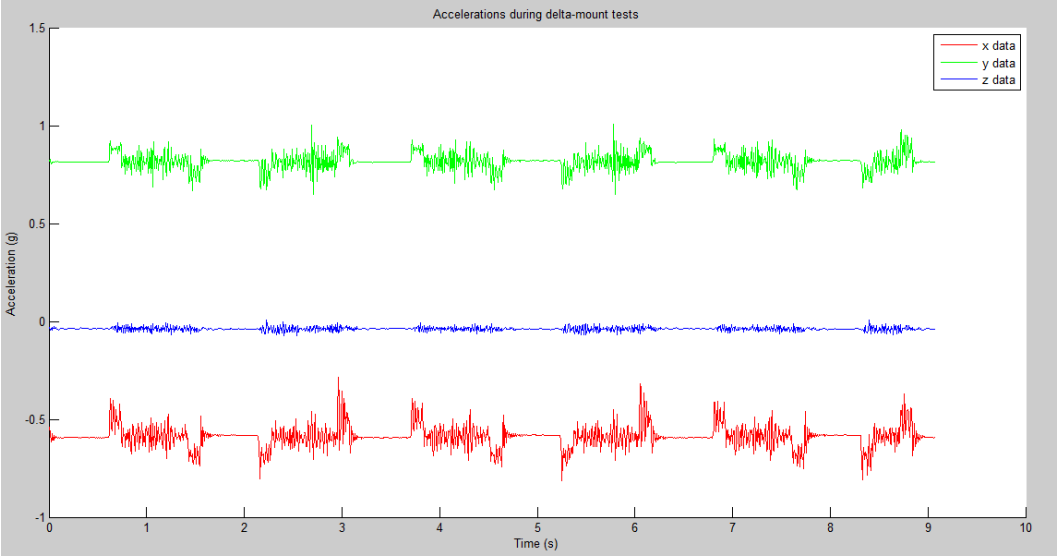

(C) Accelerations for delta run at tilt of 10°

FIGURE 4.27: Accelerations during horizontal runs with sensors mounted at various angles

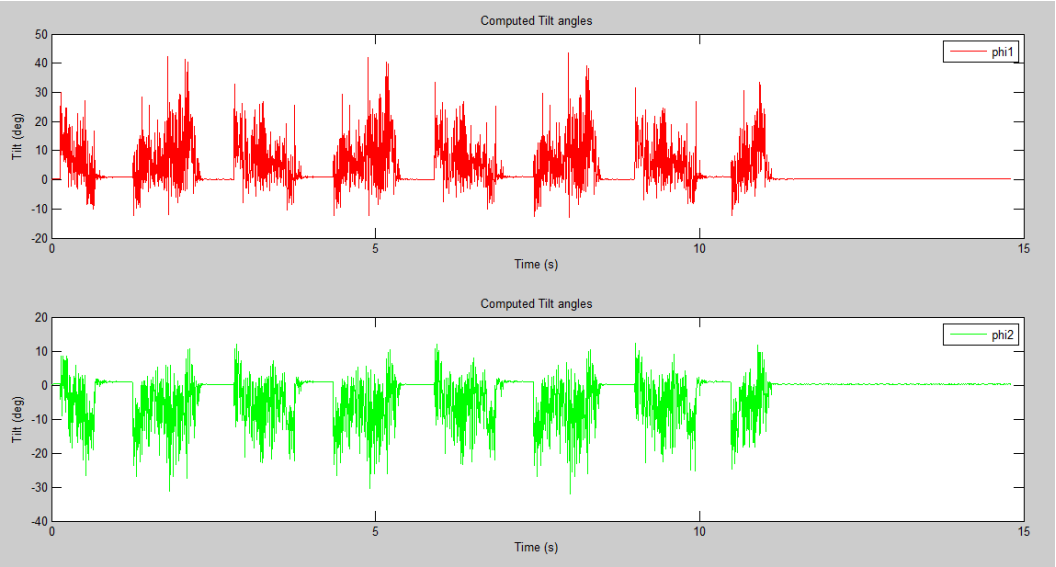

(A) Computed tilt angle for delta run at tilt of 0°

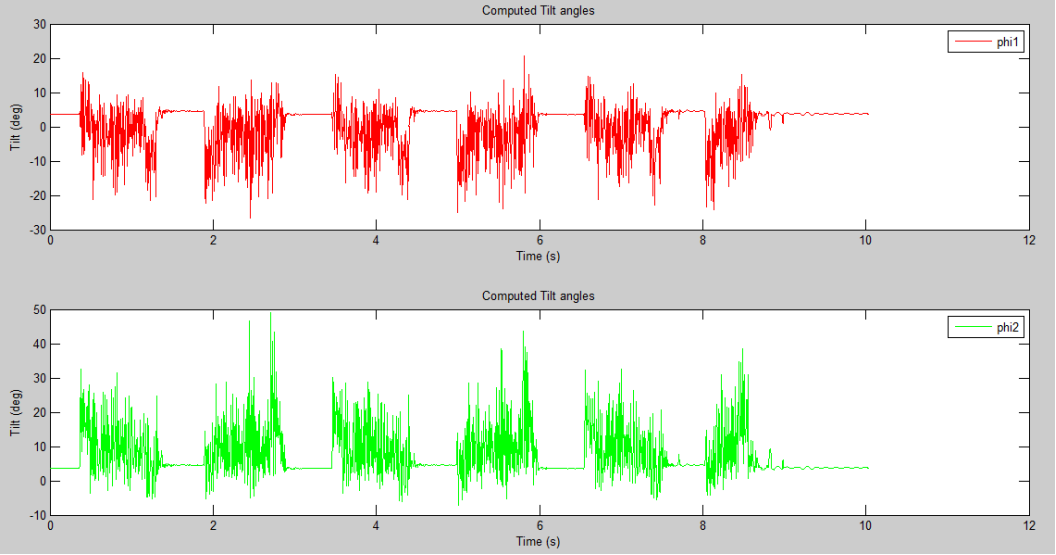

(B) Computed tilt angle for delta run at tilt of 5°

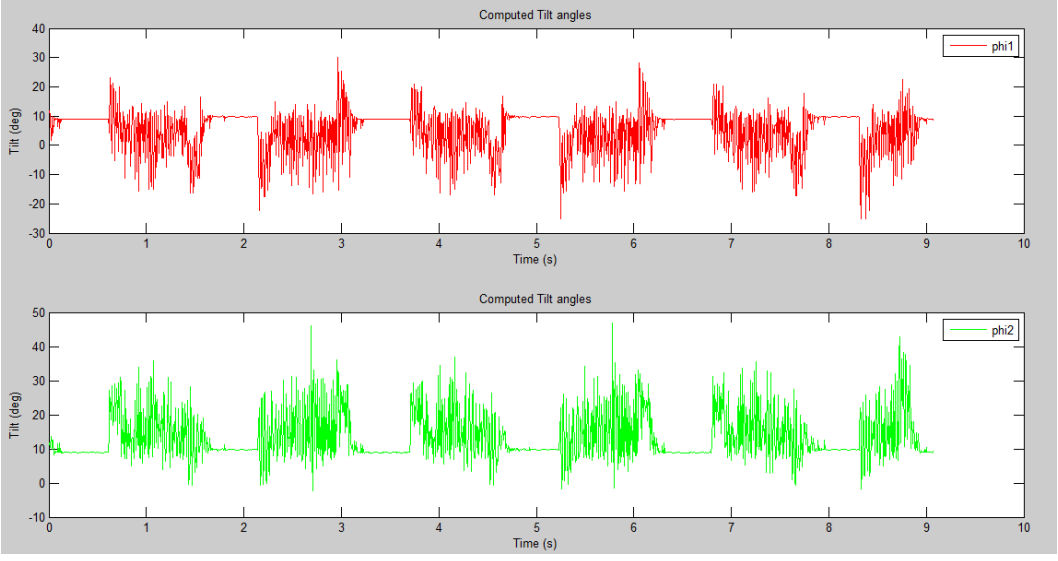

(C) Computed tilt angle for delta run at tilt of 10°

FIGURE 4.28: Computed tilt angles for horizontal runs with sensors mounted at various angles

Chapter 5

Conclusions and Future Work

5.1 Conclusions

As the mechatronics field has such a huge potential for advancement in the near future with the expanding consumer robotic market, it is necessary to investigate all sensors that assist systems in perceiving and acting in their environment. With the increasing ratio of performance to cost of MEMS accelerometer sensors, they are an ideal candidate for further development and use in various mechatronic applications for smart systems, especially in transportation and automotive industries.

The basic operation principle of MEMS accelerometers is that it functions as a mass-spring-damper system. Due to the dynamics of this system, the frequency response of the acceleration can be determined due to displacements of the proof mass within the chip. This displacement can be detected in multiple ways, both dynamic and static. The dynamic methods are characterized as AC response sensors and can only detect changing accelerations and are therefore not studied here. Piezoresistive and capacitive sensing are static methods, which can detect static or unchanging accelerations and are more widely used in industry.

The accelerometer currently in use by Thales on subway trains is the Jewell LCA-165-5051. This is a high-end and expensive sensor, which make costs of building and repairing trains higher than desirable. Over 70 sensors were sourced from the most prominent MEMS companies and narrowed down to eight sensors using a weighted-decision-making process. These eight sensors were tested using the evaluation platform built out of a modified Rostock 3D printer, using a high-speed GoPro camera to determine the ground truth of the sensors during evaluations. They were then also tested in the railway application by driving a subway train in the TTC Shepphard line. After benchmarking

all the sensors, it was found that the Kionix KXRB5 sensor performed the best amongst the others, even outperforming the high-end Jewell accelerometer. It is recommended that this sensor is put forth for further testing.

The potential of MEMS accelerometers and gyroscopes to function as an Inertial Measurement Unit (IMU) and provide localisation information for a mobile robot greatly assists the dead-reckoning problem. These sensors provide the robot with an angular speed vector about three axes in the robot's frame and a force vector along the axes in the robot's frame. The accelerations in the reference frame can be deduced and these can be integrated, knowing the initial position and speed, to track the position of the robot through some three-dimensional environment. However, in the railway environment, accelerations are almost entirely in one-dimension. This poses the following question: if the environment is constrained to one dimension, can the sensors be simplified to only one low-cost accelerometer while continuing to accurately estimate displacements over time? The very basic inertial algorithms used show that because of unknown tilts in the sensors during motion, the zero-g bias is constantly changing. The bias estimation problem becomes the biggest challenge facing accelerometers to estimate displacement.

Various methods of estimating the biaswere investigated, however it has been shown that while the sensors are in motion, it is impossible to accurately determine the bias because it is impossible to distinguish between acceleration due to gravity and acceleration due to motion. A standard deviation method to determine when there is zero velocity has been introduced, which allows the inertial algorithms to know when the sensors are not moving. This is an important algorithm, because the algorithm will not integrate the data when there is no speed, which eliminates integration drift error. It also assists the algorithms estimate the bias, because if the system is not moving, it is known that the zero-g bias is simply the current output of the accelerometer sensors.

An optimal bias algorithm was investigated, which can be used to determine the bias that would result in a zero velocity integration between two points of zero velocity. The main problem with this algorithm is that it can only be used during points where the system knows it has stopped moving, after which it can calculate the bias and update the displacement. This updated displacement has been experimentally tested to be accurate to below 10%. During motion, however, the estimated displacement is entirely dependent on how close the bias estimation is during motion, which can introduce large errors from integration.

5.2 Future Work

The biggest disadvantage of these sensors for displacement applications was identified as the integration of various errors, especially the unknown zero-g bias, which generates an undesirable random walk effect. Other main sources of error for MEMS accelerometers, as with most sensors, are issues of noise. However, because of the electromechanical nature of these sensors, they are also sensitive to temperature changes, which affect their bias and sensitivity. Furthermore, nonlinearities and cross-axis sensitivities introduce factors of error into the output of the individual axes of the sensors. The biggest challenges for this evaluation system are mounting the accelerometers level, estimating and computing the bias, and tuning the various parameters in the inertial algorithm. The 3D printer that was used exhibits the issue that as it moves along a horizontal axis, the end-effector is slightly tilted, which means that an unknown and varying component of the gravity shows up on the output of the X or Y axes. This bias needs to be subtracted from the output of the sensor in order to determine the actual signal that is due to motion. This issue would be present in any robotic or vehicular application, as perfect mounting of accelerometers is impossible and if the vehicle goes up- or down-hill, gravity components appear on the outputs in an undesirable manner.

Another challenge of the evaluation system is that the camera can only measure motion accurately in the Y and Z directions. As the end-effector moves in the X direction away from the camera, it has a lower ability of correctly determining this change in displacement. In order to capture this axis effectively, another camera would be needed or some other sensor such as an infrared or ultrasonic proximity sensor.

For future work with these MEMS accelerometers, there are a number of subjects that can be further investigated. The thermal tests were inconclusive and it would be important to ensure that the sensors can adequately function in the required temperature range. It must be kept in mind that thermal chambers induce a significant mechanical noise from vibrations as well as possibly electrical noise. Mounting sensors carefully to reduce this noise is critical.

Furthermore, it was found that the evaluation platform itself had some problems in tilting during testing. It would be beneficial to design and build an evaluation platform with a bigger workspace, which did not tilt the sensors in any way. A possible evaluation would be to design tests to run at the Vicon lab at the UTIAS (University of Toronto Institute for Aerospace Studies) motion capture laboratory. This would provide ground truth of the sensors during any sort of testing.

The inertial algorithms were able to estimate displacements to below 10% error on almost all tests and even much better on some tests. However, some of these algorithms

do not work in realtime or would only be able to update displacement at points of zero velocity. It is of interest to investigate how much these algorithms can be improved, possibly by combining the ideas from various algorithms. One method that was used in [4] is feature detection. This idea could be further applied to the data to attempt to determine various states of motion (ie. constant speed, standing still, accelerating, or braking) using signal processing techniques.

Finally, it is important to fully test if the recommended sensor, the KXRB5, can replace the high-cost Jewell currently in-use. This would involve designing a ruggedized compartment to place the sensor into as well as the electrical equipment necessary to interface to the train's control system. It will be required to run tests with the KXRB5 and the Jewell to ensure that the low-cost alternative can adequately and safely replace the Jewell accelerometer.

The list below summarizes the key ideas for future work.

- Proper thermal testing of recommended sensor(s) with investigation of mechanical noise due to vibrations and electrical noise from the equipment.
- Development of bigger evaluation platform that has the ability to rotate the sensors in a known manner as well as a larger work space (at least a few metres of travel distance) or possiblydevelop tests that can be ran at the Vicon motion capture lab at UTIAS
- Further investigate various inertial algorithms to see if they can be combined to improve results.
- Investigate feature detection possibilities using signal processing techniques to determine different states of motion.
- Perform more advanced reliability and failure testing on recommended sensor(s).
- Investigate the option of mounting sensors onto the train chassis, where there is less unknown tilt than the car body.
- Design and implement a ruggedized data capturing module for sensor(s) put forth for further development.
- Compare Jewell with recommended sensor(s) in long-term testing on TTC subway trains.

As technology advances, specifically MEMS technology as well as processing technology for intelligent systems, consumer, industrial, and commercial robotics will prove to demonstrate great capabilities to assist society in various ways. There will always be a push for more accurate sensors to assist smart systems and with the pace of improvement of the performance to cost ratio of MEMS accelerometers, they will likely be an important sensor of the future.

Appendix A

Table of all accelerometers considered

The table shown on the following page lists all the MEMS accelerometers that were considered for evaluation.

Part Number	**Manufacturer**
MPU-6000	InvenSense
MPU-6050	InvenSense
MPU-6100	InvenSense
MPU-6150	InvenSense
MPU-9150	InvenSense
MPU-9250	InvenSense
ADIS16003	Analog Devices
ADIS16201	Analog Devices
ADIS16300	Analog Devices
ADIS16305	Analog Devices
ADIS16334	Analog Devices
ADIS16362	Analog Devices
ADIS16364	Analog Devices
ADIS16445	Analog Devices
ADXL103	Analog Devices
ADXL203	Analog Devices
ADXL212	Analog Devices
ADXL213	Analog Devices
ADXL313	Analog Devices
ADXL325	Analog Devices
ADXL327	Analog Devices
ADXL335	Analog Devices
ADXL345	Analog Devices
HS8002.D	Colibrys
MS7002.3	Colibrys
MS8002.D	Colibrys
MS9001.D	Colibrys
MS9002.D	Colibrys
MS9005.D	Colibrys
RS9010.B	Colibrys
VS9002.D	Colibrys
BMA280	Bosch
BMA355	Bosch
BMI055	Bosch
BMX055	Bosch
AIS326DQ	STMicroelectronics
AIS328DQ	STMicroelectronics
LIS2DH	STMicroelectronics
LIS2DM	STMicroelectronics
LIS331DLH	STMicroelectronics
LIS3DH	STMicroelectronics
LIS3DSH	STMicroelectronics
LIS344ALH	STMicroelectronics
LIS352AR	STMicroelectronics
LIS352AX	STMicroelectronics
LIS3LV02DL	STMicroelectronics
LIS3LV02DQ	STMicroelectronics
LSM303DLH	STMicroelectronics
LSM303DLHC	STMicroelectronics
LSM330D	STMicroelectronics
LSM330DLC	STMicroelectronics
LSM9D3	STMicroelectronics
KMX61	Kionix
KMX61G	Kionix
KX022	Kionix
KXCJK	Kionix
KXR94	Kionix
KXRB5	Kionix
KXTC9	Kionix
KXTJ2	Kionix
KXG02	Kionix
KXGS2	Kionix
CXL02TG3	Memsic
MXA2500EL	Memsic

Table A.1: List of all sensors considered for evaluation

Appendix B

Full Results of Tests from all Sensors

This section presents the results from the tests for all sensors that is available to display. Some sensors do not have test results for all tests, as they were eliminated earlier during evaluation or if there was a problem during a certain run. The graphs also include results from the IG500 fom SBG Systems. This is a rugged miniature IMU that can accurately provide orientation measurements in real time. It has an internal low-pass filter, which helps reduce the noise output that is measured.

It may be noted that through various tests, after double-integration of the acceleration data, the BMA280 sensor has a final displacement that is better than the others. However, it is important to note that the Jewell accelerometer is considered the *gold standard* for these evaluations and therefore any deviation from this accelerometer is in fact not a good result. Examining the accelerations of the BMA280 compared to the other sensors, it seems to have an problem with positive accelerations. That is, the negative accelerations match the other sensors to a close degree, however the positive accelerations are noisy and overall much lower in magnitude than those from the other sensors. This may be an issue with the sensor itself or with the PSOC5 interfacing to it. The end result of this lower magnitude in the positive direction is that the displacement happens to look better due to this problem, because the integration drift is in the positive direction, so the sensor exhibits less of this integration drift due to bias errors.

B.1 Evaluation Platform Results

The following sections present the results of the sensors on the evaluation platform.

B.1.1 Off-Axis Results

The data below in Table B.1 presents the results for the three sensors LIS344ALH, MS9002.D, and BMA280 for off-axis testing on the evaluation platform. Comparing these results to Table 3.8, these three sensors have off-axis error that is significantly higher, with the LIS344ALH performing especially poorly. This could be due to mounting errors of this sensor with respect to the axis of motion.

Test	**Accelerometer**	**Measured Noise** ($\mu g/\sqrt{Hz}$)	**Maximum Signal** (mg)	**Signal Power** (g^2)
X-Axis	LIS344ALH	193652	0.936	0.3524
X-Axis	MS9002.D	39380	0.155	0.0147
X-Axis	BMA280	40293	0.251	0.0155
Z-Axis Slow	LIS344ALH	106743	0.357	0.11177
Z-Axis Slow	MS9002.D	25429	0.087	0.00633
Z-Axis Slow	BMA280	24957	0.122	0.00611
Z-Axis Medium	LIS344ALH	154457	0.486	0.23385
Z-Axis Medium	MS9002.D	30435	0.130	0.00091
Z-Axis Medium	BMA280	26484	0.157	0.00690
Z-Axis Fast	LIS344ALH	263559	2.844	0.6818
Z-Axis Fast	MS9002.D	50531	0.883	0.0251
Z-Axis Fast	BMA280	72188	1.986	0.0521
Average	LIS344ALH	32197	0.152	0.01174
Average	MS9002.D	14858	0.076	0.00253
Average	BMA280	11331	0.056	0.00147

TABLE B.1: Quantitative results from off-axis testing

B.1.2 Vibration Results

The data in Figure B.1 shows vibration data for the LIS344ALH, the MS9002.D, and the BMA280 sensors. Comparing the data from this graph to the data in Figure 3.7, the amplitude and noise level is significantly higher with these three sensors than for the Jewell, KXRB5, and LIS3LV02DL.

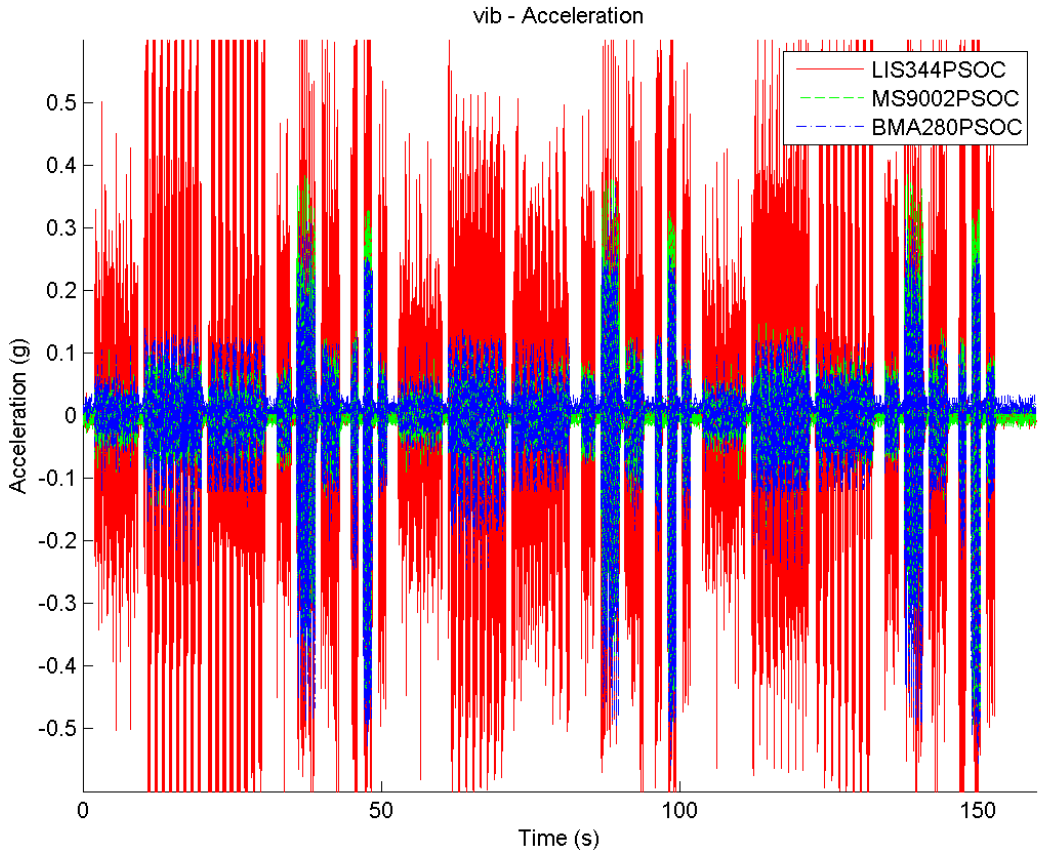

FIGURE B.1: Vibration data for three sensors

B.1.3 Step Test Results

The data in Figure B.2 shows data for the LIS344ALH, the MS9002.D, and the BMA280 sensors for the step test on the evaluation platform. The MS9002.D in this run actually has good results comparing it to the other two sensors. It also has a final displacement of only 2 m, which is good.

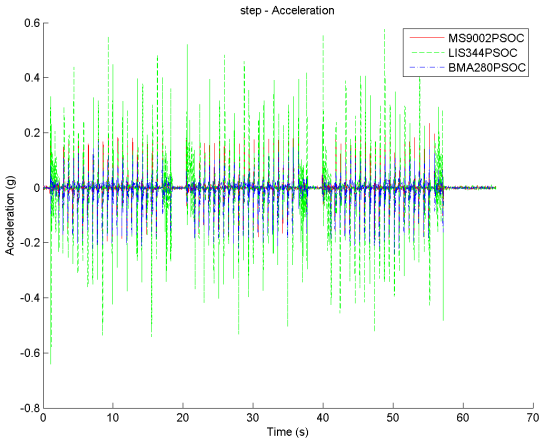

(A) Accelerations of sensors for step run

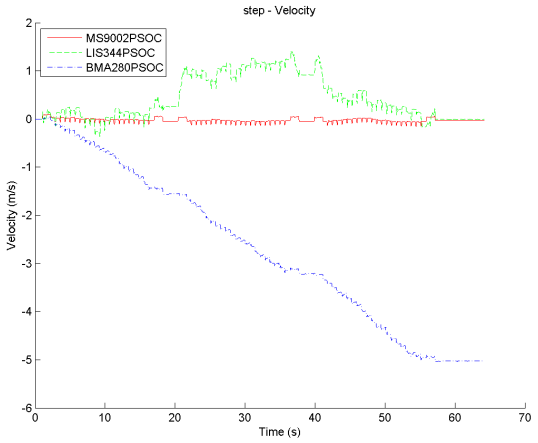

(B) Velocities of sensors for step run

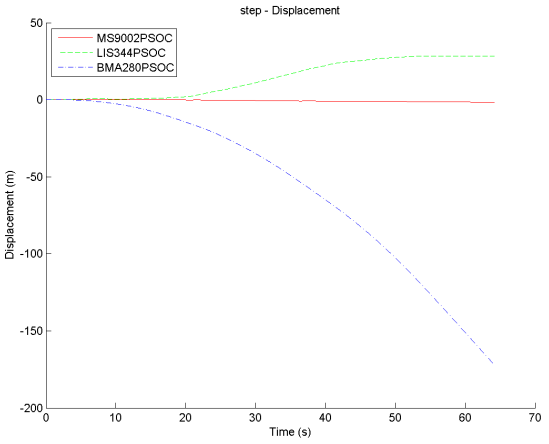

(C) Displacements of sensors for step run

FIGURE B.2: Accelerations, velocities, and displacements for step run for all sensors

B.2 Subway Train Results

The graphs on the following pages summarize the data from some of the TTC tests that were undertaken for all sensors. The simple inertial algorithm is used to estimate displacement for comparison purposes. It is important to note that the sensors are all fairly consistent amongst themselves, except for the BMA280. The main differentiator between the sensors are their noise levels. This is the fundamental reason the sensors with lowest noise were chosen to continue evaluation.

B.2.1 No Motion Noise Results

Accelerometer	**Measured Noise** ($\mu g/\sqrt{Hz}$)	**Datasheet Specification** ($\mu g/\sqrt{Hz}$)	**Total Noise** (μg)
Jewell	112.91	100.00	1129
KXRB5	54.31	45.00	869
LIS3LV02DL	80.41	158.00	1017
BMA280	929.50	120.00	9295
MS9002.D	897.41	18.00	8974
LIS344ALH	1548.21	50.00	15482
IG500	150.73	250.00	783

TABLE B.2: Noise measurements of sensors on-board subway train

B.2.2 Step Test Results

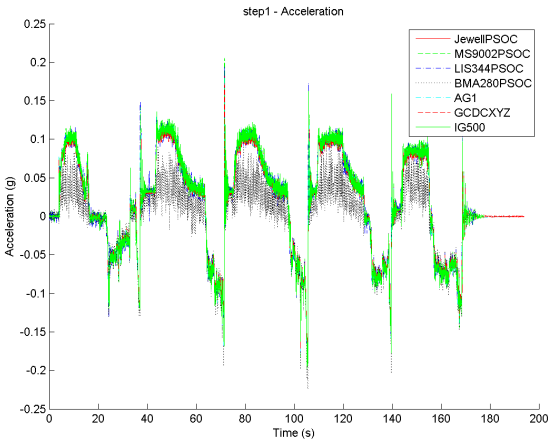

(A) Accelerations of sensors for step run 1

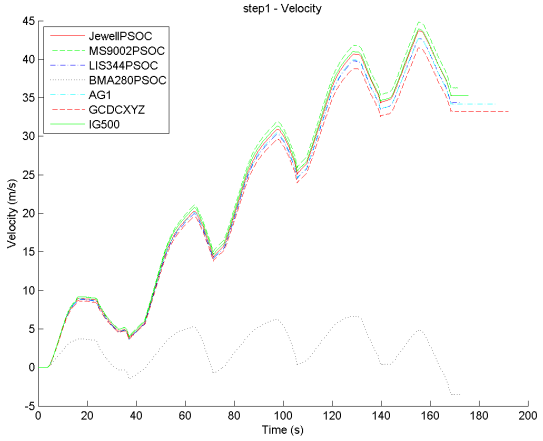

(B) Velocities of sensors for step run 1

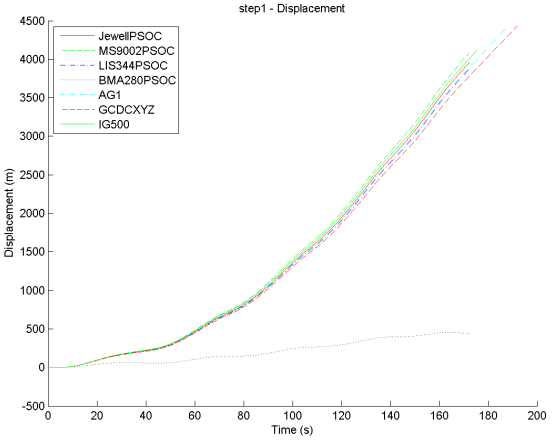

(C) Displacements of sensors for step run 1

FIGURE B.3: Accelerations, velocities, and displacements for step run 1 for all sensors

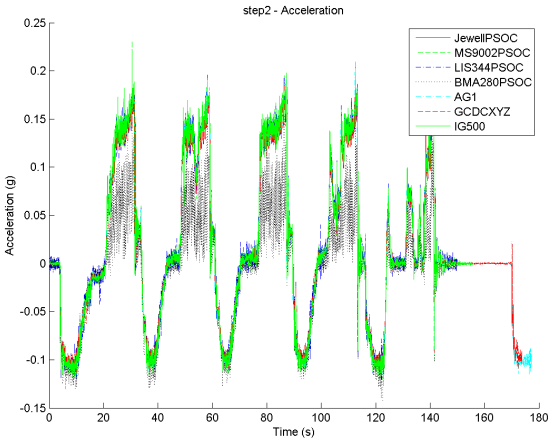

(A) Accelerations of sensors for step run 2

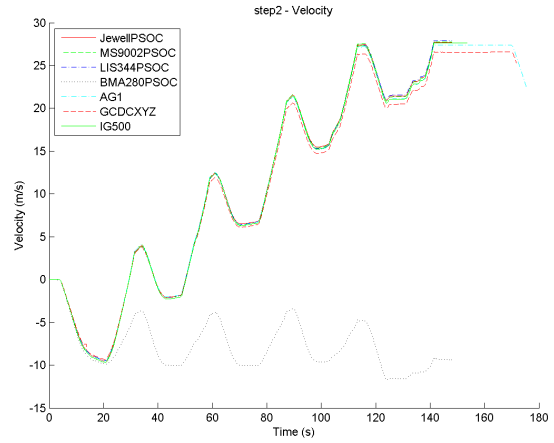

(B) Velocities of sensors for step run 2

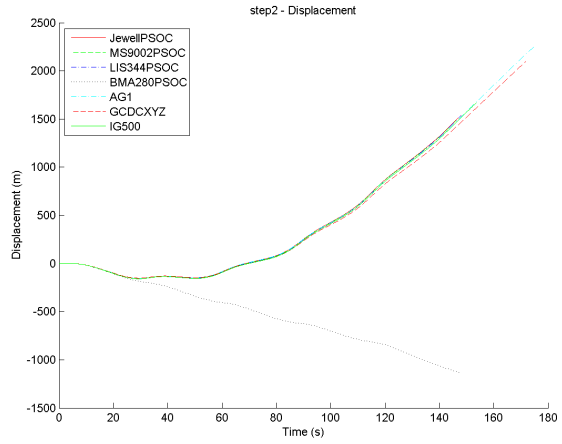

(C) Displacements of sensors for step run 2

FIGURE B.4: Accelerations, velocities, and displacements for step run 2 for all sensors

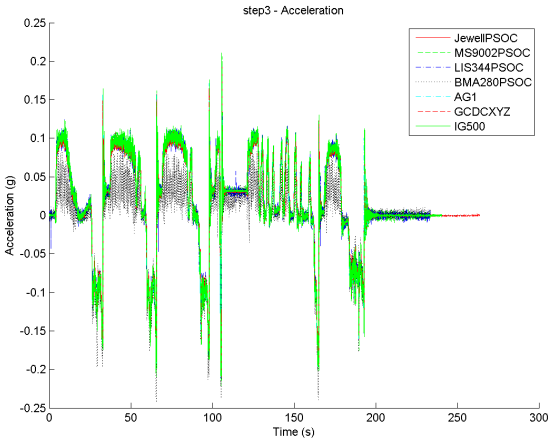

(A) Accelerations of sensors for step run 3

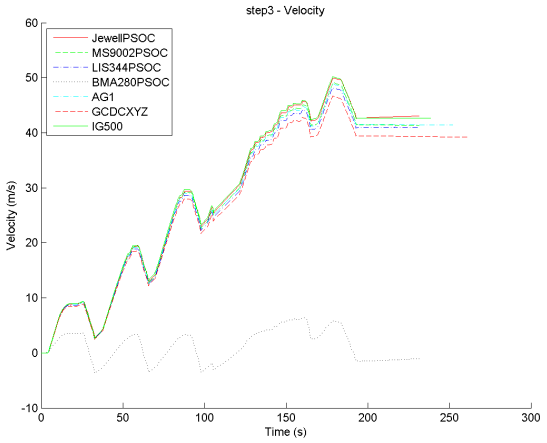

(B) Velocities of sensors for step run 3

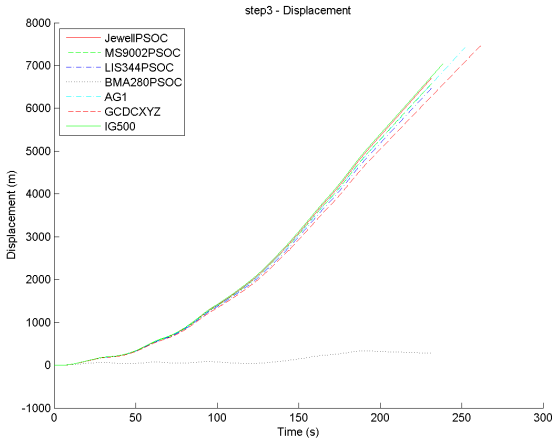

(C) Displacements of sensors for step run 3

FIGURE B.5: Accelerations, velocities, and displacements for step run 3 for all sensors

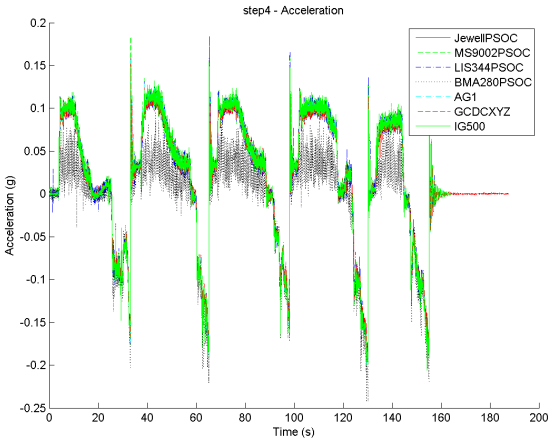

(A) Accelerations of sensors for step run 4

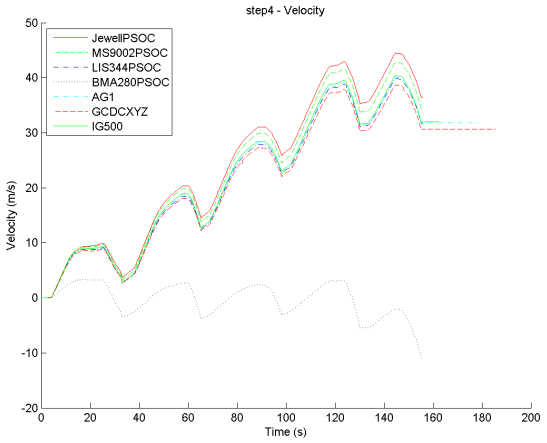

(B) Velocities of sensors for step run 4

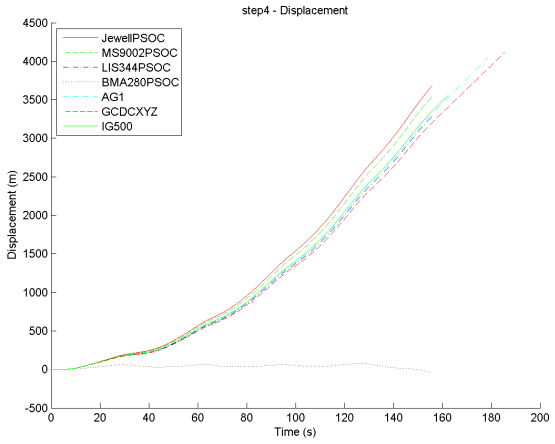

(C) Displacements of sensors for step run 4

FIGURE B.6: Accelerations, velocities, and displacements for step run 4 for all sensors

B.2.3 Shuttle Test Results

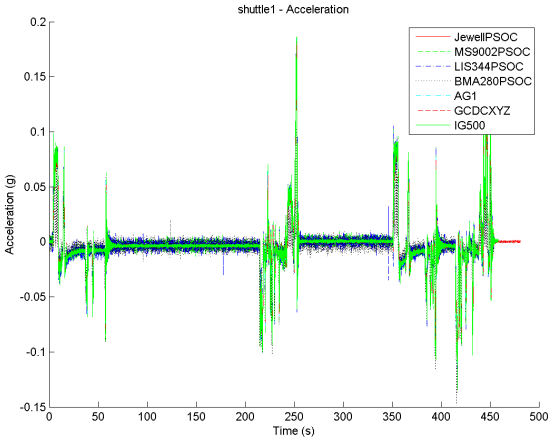

(A) Accelerations of sensors for shuttle run

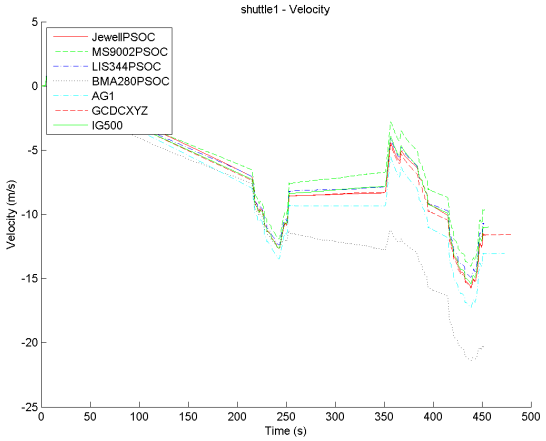

(B) Velocities of sensors for shuttle run

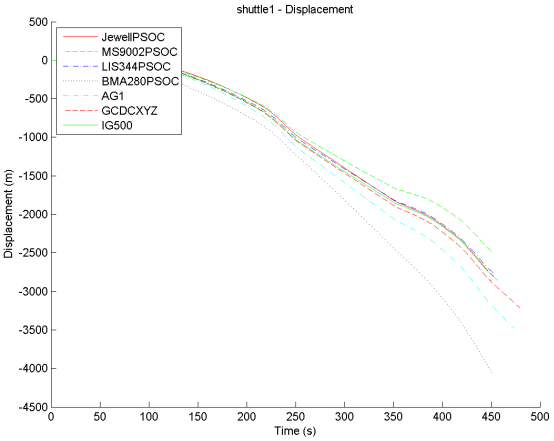

(C) Displacements of sensors for shuttle run

FIGURE B.7: Accelerations, velocities, and displacements for shuttle run for all sensors

B.2.4 Step-and-Return Test Results

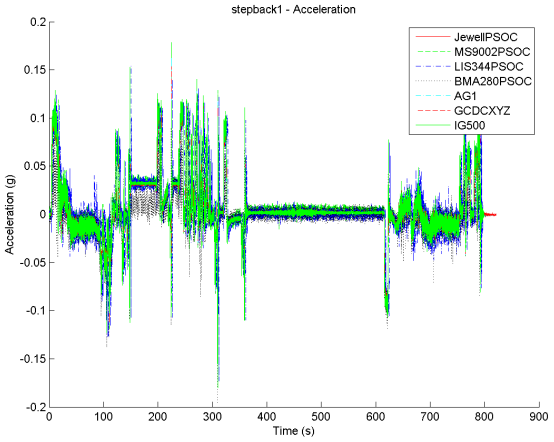

(A) Accelerations of sensors for step-and-return run 1

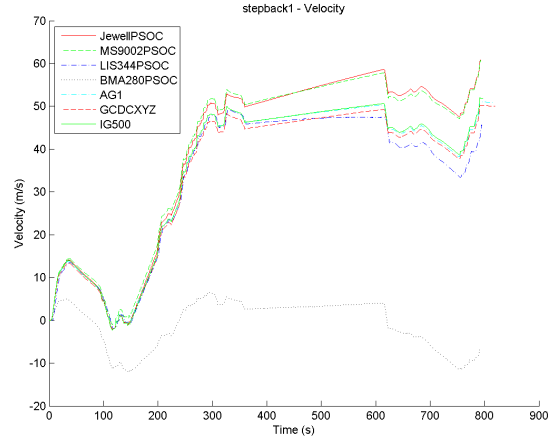

(B) Velocities of sensors for step-and-return run 1

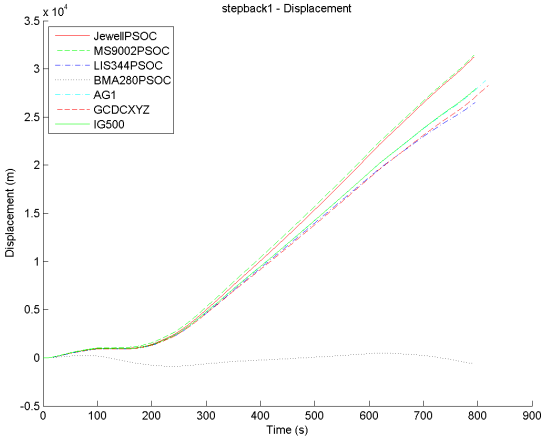

(C) Displacements of sensors for step-and-return run 1

FIGURE B.8: Accelerations, velocities, and displacements for step-and-return run 1

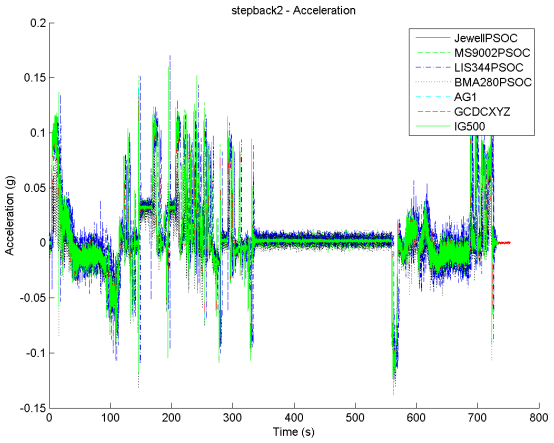

(A) Accelerations of sensors for step-and-return run 2

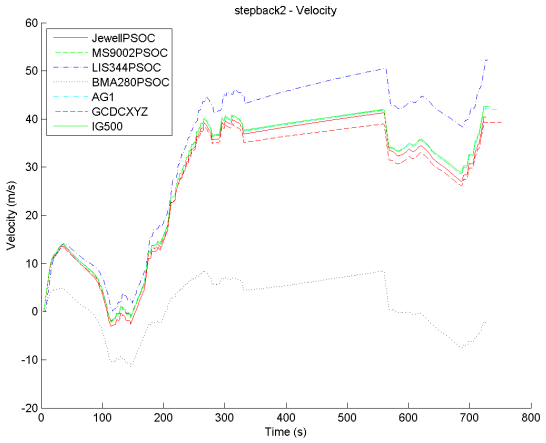

(B) Velocities of sensors for step-and-return run 2

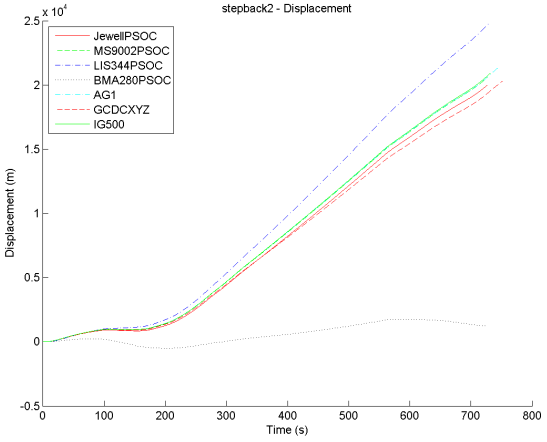

(C) Displacements of sensors for step-and-return run 2

FIGURE B.9: Accelerations, velocities, and displacements for step-and-return run 2

B.3 Thermal Testing Results

The thermal testing results were largely inconclusive due to various sources of error and inconsistencies with the methods of capturing data between different sensors. In order to fairly evaluate the sensors, the data from each sensor would have to be captured in the same manner. This way, the source of error can be tracked to either the accelerometer itself or the method capturing the data.

Below are the results from all of the sensors that underwent testing in the thermal chamber. The ADIS16305 from Analog Devices and the LSM303DLHC from STMicroelectronics did not undergo thermal testing as they were eliminated prior to this testing.

The data in Figure B.10 show the filtered results from the first test with the sensors mounted with the y-axis aligned with gravity with a thermal profile going to 85 °C as shown in Figure B.10a.

The data in Figure B.11 show the filtered results from the first test with the sensors mounted with the y-axis aligned with gravity with a thermal profile going to −40 °C as shown in Figure B.11a.

Afer the second thermal run, the GCDC data logger could not function. This is more likely due to the datalogger itself than the accelerometer. Therefore there is no available data for thermal tests 3 and 4 for the KXRB5 sensor. The data in Figure B.12 show the filtered results from the first test with the sensors mounted with the y-axis aligned at a 45° angle with respect to gravity with a thermal profile going to 85 °C as shown in Figure B.12a.

The data in Figure B.13 show the filtered results from the first test with the sensors mounted with the y-axis aligned at a 45° angle with respect to gravity with a thermal profile going to −40 °C as shown in Figure B.13a.

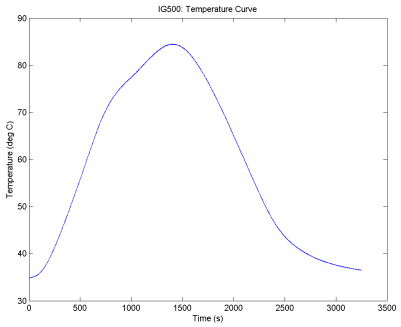

(A) Thermal curve for thermal test 1

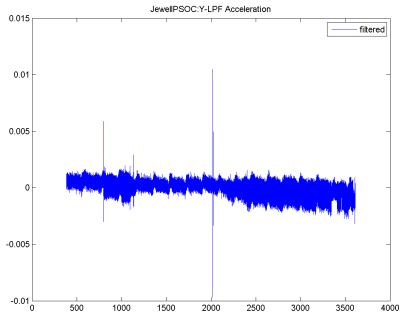

(B) Jewell filtered data

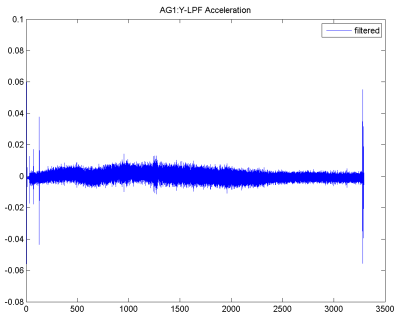

(C) LIS3LV02DL filtered data

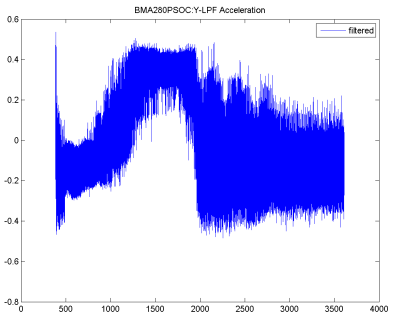

(D) BMA280 filtered data

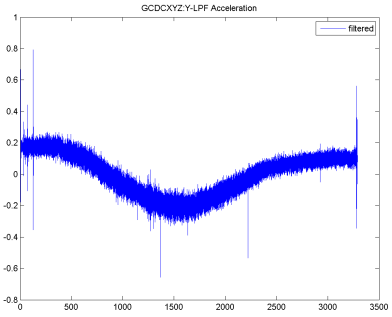

(E) KXRB5 filtered data

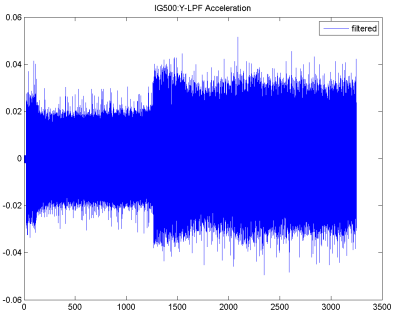

(F) IG500 filtered data

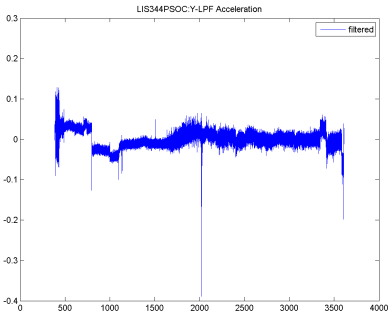

(G) LIS344ALH filtered data

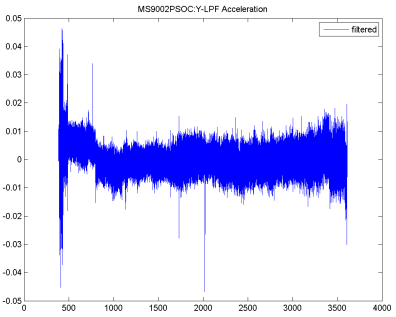

(H) MS9002.D filtered data

FIGURE B.10: Sensor data for thermal test 1

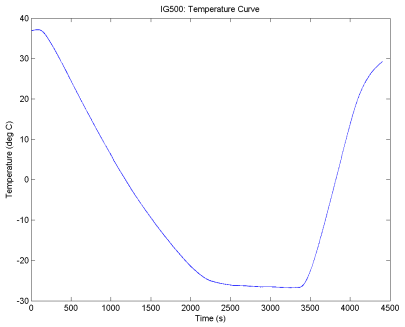

(A) Thermal curve for thermal test 2

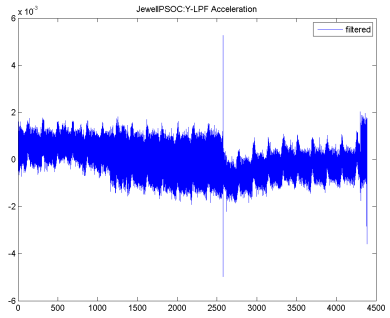

(B) Jewell filtered data

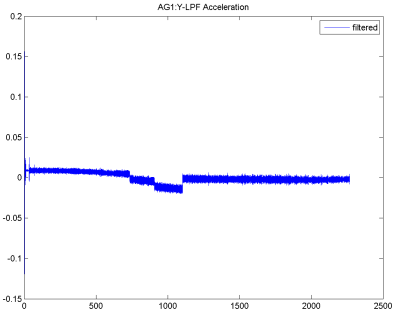

(C) LIS3LV02DL filtered data

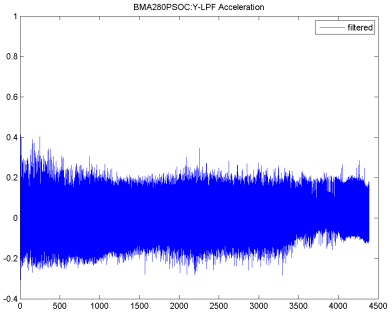

(D) BMA280 filtered data

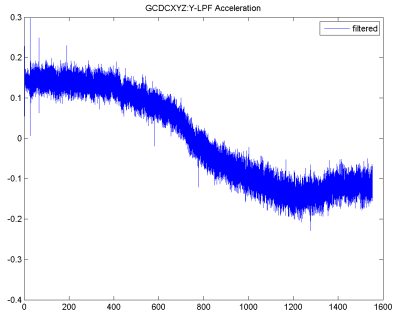

(E) KXRB5 filtered data

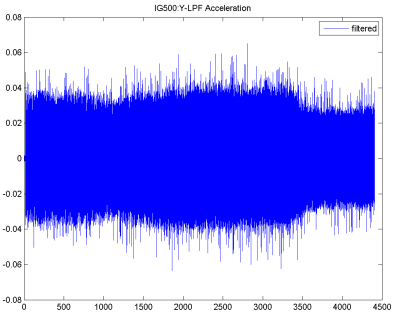

(F) IG500 filtered data

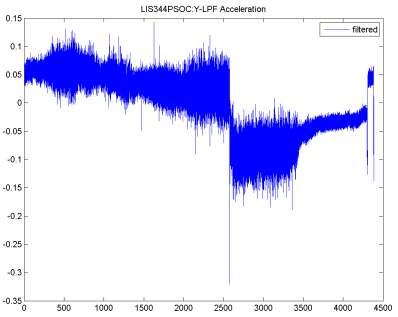

(G) LIS344ALH filtered data

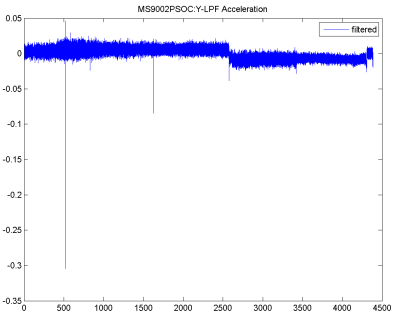

(H) MS9002.D filtered data

FIGURE B.11: Sensor data for thermal test 2

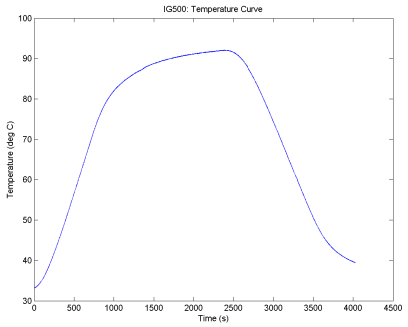

(A) Thermal curve for thermal test 3

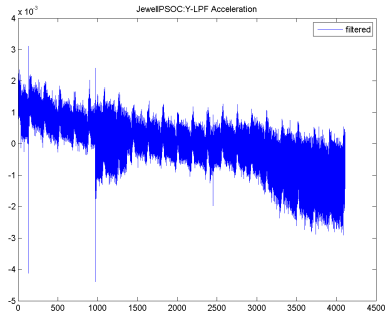

(B) Jewell filtered data

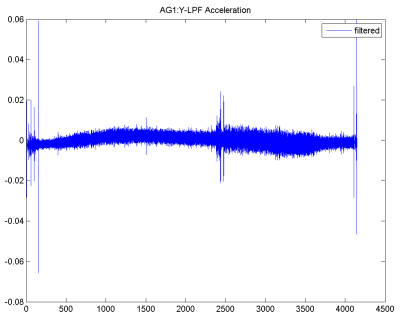

(C) LIS3LV02DL filtered data

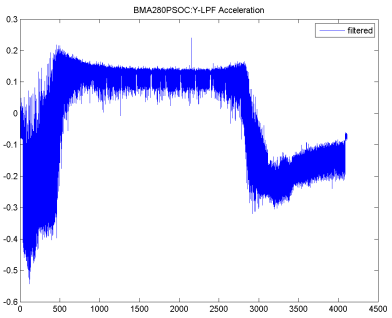

(D) BMA280 filtered data

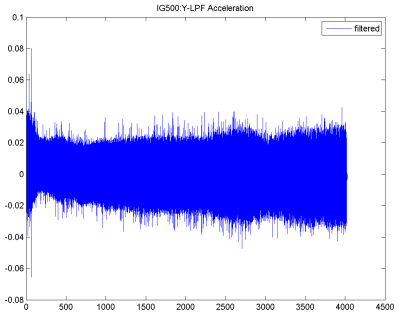

(E) IG500 filtered data

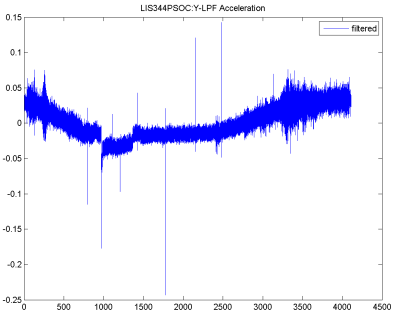

(F) LIS344ALH filtered data

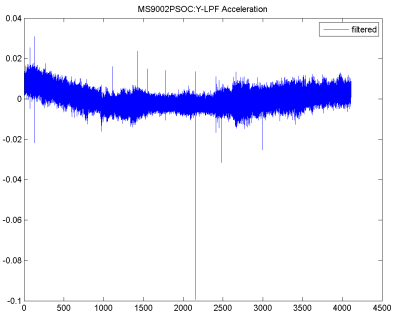

(G) MS9002.D filtered data

FIGURE B.12: Sensor data for thermal test 3

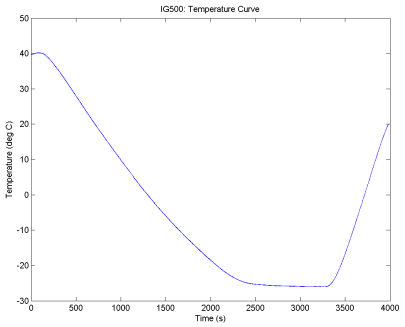

(A) Thermal curve for thermal test 4

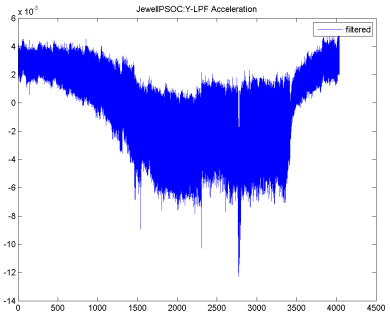

(B) Jewell filtered data

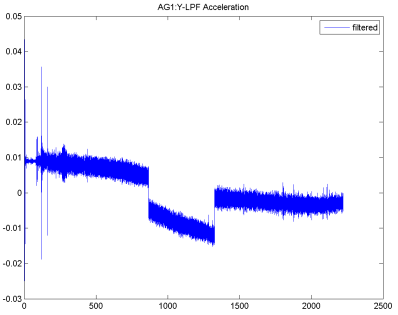

(C) LIS3LV02DL filtered data

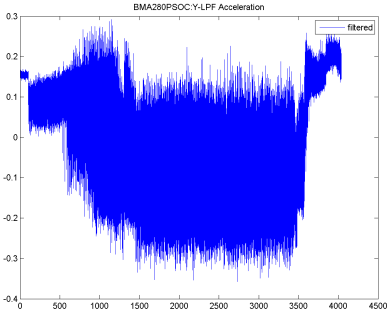

(D) BMA280 filtered data

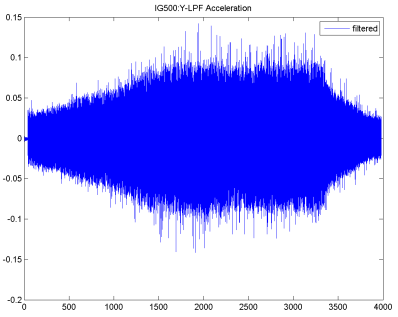

(E) IG500 filtered data

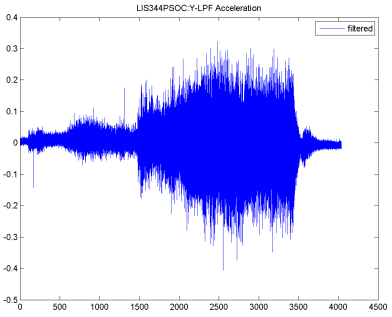

(F) LIS344ALH filtered data

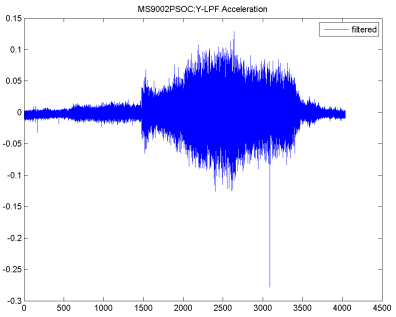

(G) MS9002.D filtered data

FIGURE B.13: Sensor data for thermal test 4

B.4 Note on ADIS16305

The Analog Devices ADIS16305 sensor was brought in and evaluated in the early stages of the work. The sensor was sampled at a high sampling rate above 500 Hz. However, it was found that the timestamps on the data had issues because for every timestamp, multiple samples existed. This created an issue that it was unknown what precise time each sample was for and the problem that multiple samples existed for different time periods.

The problem of the timestamps with the evaluation board and evaluation software coupled with the fact that in general, the noise level of the sensor was greater than the others being tested at the time, brought an end to further testing of this sensor. It may be of interest to further test this sensor using a different evaluation setup, in order to correct the timestamp problem and determine if it is an acceptable sensor for railway applications.

Appendix C

Derivation for Equations for Delta-Mounted Sensor

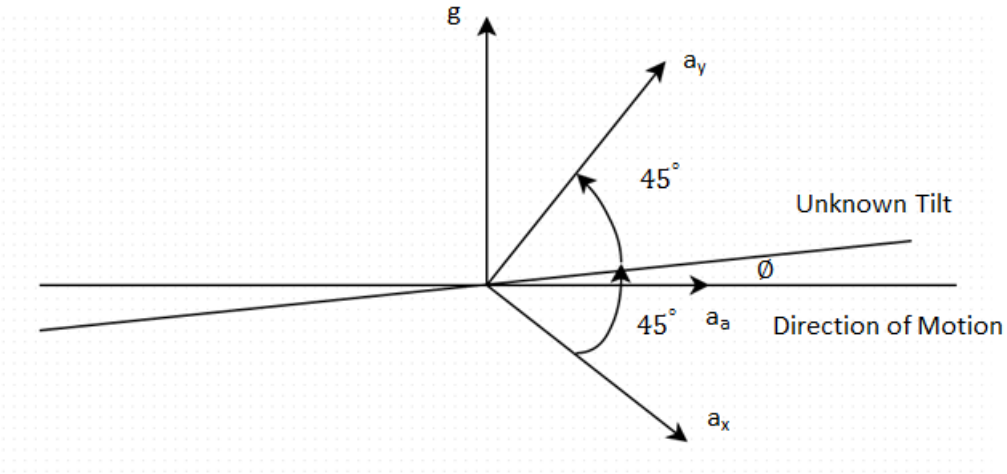

FIGURE C.1: Delta-mounted sensors with labelled axes

This Appendix shows the derivation of the quadratic equation for the delta-mounted sensors during motion.Figure C.1 shows how the sensors are mounted, as well as the symbols for the derivation. In the following, a_x and a_y are respectfully the x-axis and y-axis sensor readings, g is the acceleration due to gravity, a_a is the applied acceleration from the motion platform or subway train, and ϕ is the unknown tilt angle that is being determined.

The small angle approximations, shown in Equation (C.1) and Equation (C.2) are used in addition to the Sum-Difference trigonometric identities, shown in Equation (C.3) and Equation (C.4).

$$\cos\phi \approx 1 - \frac{\phi^2}{2} \tag{C.1}$$

$$\sin\phi \approx \phi \tag{C.2}$$

$$\sin(u \pm v) = \sin u \cos v \pm \cos u \sin v \tag{C.3}$$

$$\cos(u \pm v) = \cos u \cos v \mp \cos u \sin v \tag{C.4}$$

Examing the free-body diagram in Figure C.1, we have the following equation.

$$a_x = a_a \cos(\pi/4 - \phi) - g\cos(\pi/4 + \phi) \tag{C.5}$$

$$a_y = a_a \cos(\pi/4 + \phi) + g\sin(\pi/4 + \phi) \tag{C.6}$$

Using Equation (C.4) to expand the trigonometric functions, we obtain

$$\begin{aligned} a_x &= a_a \cos(\pi/4 - \phi) - g\cos(\pi/4 + \phi) && \text{(C.7)}\\ &= a_a[\cos\frac{\pi}{4}\cos\phi + \sin\frac{\pi}{4}\sin\phi] - g[\cos\frac{\pi}{4}\cos\phi - \sin\frac{\pi}{4}\sin\phi] && \text{(C.8)}\\ &= a_a[\frac{\sqrt{2}}{2}\cos\phi + \frac{\sqrt{2}}{2}\sin\phi] - g[\frac{\sqrt{2}}{2}\cos\phi - \frac{\sqrt{2}}{2}\sin\phi] && \text{(C.9)} \end{aligned}$$

Similarly for a_y, we use Equation (C.3) and Equation (C.4) to obtain

$$\begin{aligned} a_y &= a_a \cos(\pi/4 + \phi) + g\sin(\pi/4 + \phi) && \text{(C.10)}\\ &= a_a[\cos\frac{\pi}{4}\cos\phi - \sin\frac{\pi}{4}\sin\phi] + g[\sin\frac{\pi}{4}\cos\phi + \cos\frac{\pi}{4}\sin\phi] && \text{(C.11)}\\ &= a_a[\frac{\sqrt{2}}{2}\cos\phi - \frac{\sqrt{2}}{2}\sin\phi] + g[\frac{\sqrt{2}}{2}\cos\phi + \frac{\sqrt{2}}{2}\sin\phi] && \text{(C.12)} \end{aligned}$$

If we let $x = \frac{\sqrt{2}}{2}\cos\phi$ and $y = \frac{\sqrt{2}}{2}\sin\phi$, we can simplify Equation (C.9) and Equation (C.12).

$$a_x = a_a[x + y] - g[x - y] \tag{C.13}$$

$$a_y = a_a[x - y] + g[x + y] \tag{C.14}$$

Using Equation (C.13) and Equation (C.14) and solving for a_a, we have

$$a_a = \frac{a_x + g[x - y]}{x + y} = \frac{a_y - g[x + y]}{x - y} \tag{C.15}$$

Equating the right side of Equation (C.15) and simplifying, we obtain

$$a_x[x - y] + g[x - y]^2 = a_y[x + y] - g[x + y]^2 \tag{C.16}$$

$$a_x[x - y] + gx^2 - 2gxy + gy^2 = a_y[x + y] - gx^2 - 2gxy - gy^2 \tag{C.17}$$

Bringing all terms to one side to equation to zero,

$$a_y[x + y] - a_x[x - y] - 2gx^2 - 2gy^2 = 0 \tag{C.18}$$

Now subbing back in our terms for x and y, we obtain

$$a_y[\frac{\sqrt{2}}{2}\cos\phi + \frac{\sqrt{2}}{2}\sin\phi] - a_x[\frac{\sqrt{2}}{2}\cos\phi - \frac{\sqrt{2}}{2}\sin\phi - 2g[\frac{1}{2}\cos^2\phi] - 2g[\frac{1}{2}\sin^2\phi] = 0$$

Now, simplifying with the small-angle approximations Equation (C.1) and Equation (C.2), we obtain

$$a_y[\frac{\sqrt{2}}{2}(1 - \frac{\phi^2}{2}) + \frac{\sqrt{2}}{2}\phi] - a_x[\frac{\sqrt{2}}{2}(1 - \frac{\phi^2}{2}] - g(1 - \frac{\phi^2}{2})^2 - g\phi^2 = 0$$

$$a_y[\frac{\sqrt{2}}{2}(1 - \frac{\phi^2}{2}) + \frac{\sqrt{2}}{2}\phi] - a_x[\frac{\sqrt{2}}{2}(1 - \frac{\phi^2}{2}] - g + g\phi^2 - \frac{g\phi^4}{4} - g\phi^2 = 0$$

Here, the $g\phi^2$ terms cancel out and we can make the approximation that $\phi^4 << \phi^2$ to obtain:

$$\frac{a_y\sqrt{2}}{2} - \frac{a_y\sqrt{2}}{4}\phi^2 + \frac{a_y\sqrt{2}}{2}\phi - \frac{a_x\sqrt{2}}{2} + \frac{a_y\sqrt{2}}{4}\phi^2 + \frac{a_x\sqrt{2}}{2}\phi - g = 0$$

Multiplying by 4 and grouping terms, we obtain

$$(a_x - a_y)\phi^2 + (2a_x + 2a_y)\phi + 2a_y - 2a_x - \frac{4g}{\sqrt{2}} = 0$$

The solution to this quadratic equation is found using the quadratic formula, $\phi = \frac{-b \pm \sqrt{b^2 - 4ac}}{2a}$, where $a = a_x - a_y$, $b = 2a_x + 2a_y$, and $c = 2a_y - 2a_x - \frac{4g}{\sqrt{2}}$.

$$\phi_{1,2} = \frac{-(2a_x + 2a_y) \pm \sqrt{(2a_x + 2a_y)^2 - 4(a_x - a_y)(2a_y - 2a_x - \frac{4g}{\sqrt{2}})}}{2(a_x - a_y)}$$

Bibliography

[1] Oliver Woodman. Pedestrian localisation for indoor environments. *Digital Technology Group, Computer Laboratory, University of Cambridge*, Sept. 2010.

[2] Ville Kaajakari. *Practical MEMS*. Small Gear Publishing, 2009.

[3] Matthew Beckler. Accelerometer-based inertial navigation. *University of Minnesota, Electrical and Computer Engineering*, May 2008.

[4] O. Heirich, A. Lehner, P. Robertson, and T. Strang. Measurement and analysis of train motion and railway track characteristics with inertial sensors. In *14th International Conference on Intelligent Transportation Systems (ITSC)*, pages 1995 – 2000, Washington, 2011.

[5] M. Lauer and D. Stein. Algorithms and concepts for an onboard train localization system for safety-relevant services. In *IEEE International Conference on Intelligent Rail Transportation (ICIRT)*, pages 65 – 70, Beijing, 2013.

[6] O. Heirich, A. Lehner, P. Robertson, and T. Strang. Probabilistic localization method for trains. In *IEEE Intelligent Vehicles Symposium (IV)*, pages 482 – 487, Alcala de Henares, 2012.

[7] Mathworks. Find circles using Hough Transform, September 2014. URL http://www.mathworks.com/help/images/ref/imfindcircles.html.

[8] Analog Devices. Accelerometer specifications - quick definitions, September 2014. URL http://www.analog.com/en/content/td_accelerometer_specifications_definitions/fca.htmlS.

[9] Mathworks. Find minimum of unconstrained multivariable function, September 2014. URL http://www.mathworks.com/help/optim/ug/fminunc.html.